# Numerical Optimization of Boundary-Layer Control using Dielectric Barrier Discharge Plasma Actuators

Vom Fachbereich Maschinenbau
an der Technischen Universität Darmstadt
zur
Erlangung des Grades eines Doktor der
Naturwissenschaften
(Dr. rer. nat.) genehmigte

Dissertation

vorgelegt von

**M.Sc. Régis Sperotto de Quadros**

aus Passo Fundo - RS - Brasilien

| | |
|---|---|
| Berichterstatter: | Prof. Dr.-Ing. C. Tropea |
| Mitberichterstatter: | Prof. Dr.-Ing. S. Ulbrich |
| Tag der Einreichung: | 05.05.2009 |
| Tag der mündlichen Prüfung: | 01.07.2009 |

Darmstadt 2009
D17

Hiermit versichere ich, die vorliegende Doktorarbeit unter der Betreuung von Prof. Dr.-Ing. C. Tropea nur mit den angegebenen Hilfsmitteln selbständig angefertigt zu haben.

Darmstadt, den 05.05.2009

to my wife Daniela Buske

# Abstract

A numerical investigation of active wave cancellation, using a plasma actuator in both continuous and pulsed operation modes, was carried out for a flat-plate boundary layer with an adverse pressure gradient at low Reynolds number. Pulsing was achieved by rectangular and sinusoidal modulation of the high-frequency plasma excitation voltage. A closed-loop control was developed and implemented using Large-Eddy Simulations into a CFD code (FASTEST). With this feed-back control algorithm it was found that the control can be limited to two operating parameters in order to significantly reduce Tollmien-Schlichting waves (TS-waves). The feed-back control algorithm was validated using two existing optimization methods which were also implemented in the code. The first method finds a local minimum of a function with several variables using a pattern search technique that compares function values at the three vertices of a triangle. The second method, known as the *trust-region* method, is based on quadratic models for derivative-free minimization. It was found that the developed feed-back control works efficiently and can be used to determine the optimum operating parameters of the plasma actuator for cancellation of TS-waves. The amplitude reduction of TS-waves is of interest since it allows for a delay of laminar-to-turbulent transition in the boundary layer, resulting in significant drag reduction.

# Zusammenfassung

In der vorliegenden Arbeit wird eine numerische Untersuchung zur aktiven Wellendämpfung mit Plasma-Aktuatoren vorgestellt. Die Aktuatoren kommen in einer verzögerten Grenzschichtströmung entlang einer ebenen Platte bei kleinen Reynoldszahlen zum Einsatz und können kontinuierlich oder gepulst betrieben werden, wobei die Pulsation durch rechteckige bzw. sinusförmige Modulation der hochfrequenten Spannung zur Plasma-Erzeugung realisiert wird. Ein geschlossener Kontrollkreislauf zur Dämpfung von Tollmien-Schlichting Wellen (TS-Wellen) wurde entwickelt und in einen Code zur Large-Eddy Simulation der Grenzschicht implementiert. Dabei zeigt sich, dass die Kontrolle zweier Betriebsparameter ausreicht, um die TS-Wellen signifikant zu dämpfen. Um den optimierten Betrieb der Aktuatoren in dem Kontrollkreislauf zu validieren, wurden zwei aus der Literatur bekannte Optimierungsmethoden in den Code implementiert. Die erste Methode bestimmt das lokale Minimum einer Funktion mit verschiedenen Variablen auf Grundlage einer Zielfunktion, bei der die Funktionswerte an den Ecken eines Dreiecks verglichen werden. Bei der zweiten Methode handelt es sich um eine Trust-Region Methode, die auf quadratischen Modellen zur ableitungsfreien Minimierung beruht. Es konnte gezeigt werden, dass der entwickelte Kontrollkreislauf effizient funktioniert und eine Optimierung der Betriebsparameter des Plasma Aktuators ermöglicht, so dass eine deutliche Verringerung der TS-Wellenamplitude in der Grenzschicht realisiert werden kann. Dies führt zu einer Verzögerung der laminar-turbulenten Transition und somit zu signifikanter Reibungsminderung.

# Contents

# Nomenclature

## Latin Letters

| Symbol | Description | Units |
|---|---|---|
| $\tilde{A}$ | middle point NELMEAD method | $-$ |
| $A_0$ | disturbance amplitude | $-$ |
| $a, a_0$ | plasma actuator width | $m$ |
| $a_{ij}$ | tensor of small structures | $-$ |
| $b, b_0$ | plasma actuator length | $m$ |
| $bf$ | voltage | $V$ |
| $\tilde{B}$ | best vertex NELMEAD method | $-$ |
| $c$ | phase velocity | $\frac{m}{s}$ |
| $c_i$ | amplification factor of a perturbation (complex) | $\frac{m}{s}$ |
| $c_f$ | skin friction | $-$ |
| $c_g$ | Germano's constant | $-$ |
| $c_r$ | phase velocity of a perturbation | $\frac{m}{s}$ |
| $c_s$ | Smagorinsky's constant | $-$ |
| $\tilde{C}$ | contraction point NELMEAD method | $-$ |
| $d$ | distance between the two electrodes | $m$ |
| $DC$ | duty cycle of the modulation in pulsed mode | % |
| $\tilde{E}$ | expand point NELMEAD method | $-$ |
| $e_c$ | elementar charge | $C$ |
| $E_S$ | disturbance energy | $Nm$ |
| $E_t$ | threshold energy | $Nm$ |
| $f$ | frequency | $\frac{1}{s}$ |
| $F$ | objective function | $-$ |
| $\tilde{G}$ | good vertex NELMEAD method | $-$ |
| $G$ | filter function | $m$ |

| | | |
|---|---|---|
| $h$ | channel width | $m$ |
| $h$ | step size | $m$ |
| $i$ | imaginary number | $-$ |
| $K$ | von Karman constant, K=0.4 | $-$ |
| $k_1, k_2$ | scaling parameters | $-$ |
| $L_{ij}$ | modeled turbulent stress | $-$ |
| $M_{ij}$ | resolved turbulent stress | $-$ |
| $m_1$, $m_2$ | gradients of electric field | $-$ |
| $N$ | number of grid point | $-$ |
| $Re$ | Reynolds number | $-$ |
| $Re_c$ | critical Reynolds number | $-$ |
| $Re_\delta$ | displacement Reynolds number | $-$ |
| $Re_T$ | turbulent Reynolds number | $-$ |
| $Re_\tau$ | friction Reynolds number | $-$ |
| $Re_x$ | streamwise Reynolds number | $-$ |
| $p$ | pressure | $\frac{N}{m^2}$ |
| $\tilde{R}$ | reflection point NELMEAD method | $-$ |
| $\tilde{S}$ | shrink point NELMEAD method | $-$ |
| $s_{ij}$ | shear-stress tensor | $-$ |
| $\bar{s}_{ij}$ | filter shear-stress tensor | $-$ |
| $t$ | time | $s$ |
| $T^*$ | threshold | $\frac{m}{s}$ |
| $T$ | temperature | $K$ |
| $Te$ | kinetic energy of the electron | $Nm$ |
| $T_{ij}$ | stress tensor | $-$ |
| $\vec{u} = (u, v, w)^T$ | velocity vector | $\frac{m}{s}$ |
| $\bar{u}$ | streamwise time average velocity | $\frac{m}{s}$ |
| $\vec{u}' = (u', v', w')^T$ | disturbance velocity | $\frac{m}{s}$ |
| $u_\tau$ | friction velocity | $\frac{m}{s}$ |
| $u_{rms}$ | RMS value of the wall-parallel velocity fluctuation | $\frac{m}{s}$ |
| $V_{ac}$ | alternating voltage | $V$ |

|  |  |  |
|---|---|---|
| $\tilde{W}$ | worse point NELMEAD method | – |
| $x_{opt}$ | optimal distance | $m$ |
| $\vec{x} = (x, y, z)^T$ | cartesian coordinates | $m$ |
| $y_{max}$ | truncation position | – |

## Greek Letters

| Symbol | Description | Units |
|---|---|---|
| $\alpha$ | streamwise wave number | $\frac{1}{m}$ |
| $\alpha^*$ | convergency parameter | – |
| $\alpha_i$ | imaginary eigenvalue | – |
| $\alpha_r$ | real eigenvalue | – |
| $\tilde{\alpha}, \tilde{\beta}, \tilde{\gamma}$ | convergence constant NELMEAD method | – |
| $\beta$ | spanwise wave number | $\frac{1}{m}$ |
| $\beta_i$ | ampliation factor | – |
| $\beta_r$ | circular wave number | $rad$ |
| $\delta$ | boundary-layer thickness | $m$ |
| $\delta_1$ | displacement thickness | $m$ |
| $\delta_2$ | momentum thickness | $m$ |
| $\delta_{99}$ | boundary-layer thickness | $m$ |
| $\delta_{ij}$ | Kronecker delta | – |
| $\Delta$ | filter width | $m$ |
| $\Delta^{(k)}$ | distance thrust-region NEWUOA method | $m$ |
| $\varepsilon$ | convergence error | – |
| $\eta$ | similarity variable | – |
| $\tau$ | Kolmogorov time scale | $s$ |
| $k(\alpha, \beta)^T$ | wave number vector | $\frac{1}{m}$ |
| $\lambda$ | wavelength | $m$ |
| $\mu$ | dynamic viscosity | $\frac{kg}{ms}$ |
| $\nu$ | kinematic viscosity | $\frac{m^2}{s}$ |

| | | |
|---|---|---|
| $\nu_\tau$ | turbulent kinematic viscosity | $\frac{m^2}{s}$ |
| $\rho$ | density | $\frac{kg}{m^3}$ |
| $\rho_{beg}$ | initial thrust-region NEWUOA method | $\frac{kg}{m^3}$ |
| $\rho_c$ | charge density | $\frac{C}{m^3}$ |
| $\rho_{end}$ | final thrust-region NEWUOA method | $m$ |
| $\rho_{(k)}$ | NEWUOA convergence parameter | $m$ |
| $\tau_{ij}$ | subgrid scale stress | $\frac{N}{m^2}$ |
| $\tau_w$ | wall-shear stress | $\frac{N}{m^2}$ |
| $\hat{v}$ | velocity amplitude function | $m/s$ |
| $\varphi_v, \varphi_\omega$ | phase displacement | $rad$ |
| $\phi$ | phase shift | $^o$ |
| $\phi_E$ | applied voltage potential | $Volt$ |
| $\psi$ | streamfunction | $\frac{m^2}{s}$ |
| $\omega$ | angular frequency | $\frac{1}{s}$ |
| $\vec{\Omega} = (\Omega_x, \Omega_y, \Omega_z)^T$ | vorticity | $\frac{1}{s}$ |
| $\bar{\Omega}(y)$ | vorticity amplitude function | $-$ |

## Subscripts and Superscripts

| Symbol | Description |
|---|---|
| $C$ | characteristic quantities |
| $crit$ | quantities in the critical point |
| $\delta$ | relating to the edge of the boundary layer |
| $i$ | imaginary part |
| $i$ | numerical index |
| $j$ | numerical index |
| $k$ | numerical index |
| $L$ | characteristic length |
| $max$ | maximum of a quantity |
| $min$ | minimum of a quantity |

| | |
|---|---|
| $r$ | real part |
| $\mathbb{R}$ | set real numbers |
| $2D$ | two-dimensional approach |
| $3D$ | three-dimensional approach |
| $DNS$ | Direct Numerical Simulation |
| $DC$ | duty cycle |
| $FFT$ | Fast-Fourier-Transformation |
| $LES$ | Large-Eddy Simulation |
| $PIV$ | Particle Image Velocimetry |
| $RMS$ | root mean square |
| $SGS$ | subgrid scales |
| $sgn$ | signal |

# List of Figures

# 1 Introduction

## 1.1 Flow control

Many flows, especially in external aerodynamics, are decidedly influenced by the state and behaviour of the near-wall flow structure - the boundary layer. The velocity gradient at the wall, or even more precisely the wall shear stress, determines the skin friction, but also the susceptibility of the boundary layer to separate from the body, resulting in reverse flow regions. While the skin friction is directly responsible for frictional drag on a body, phenomena such as separation can lead to massive changes of pressure drag or lift, e.g. wing stall. The wall shear stress for a given outer velocity is highly dependent on the state of the boundary layer - laminar or turbulent. Whereas a laminar boundary exhibits much lower wall shear stress, a turbulent boundary layer offers much high momentum transport transverse to the mean velocity gradient; hence withstanding a much higher negative streamwise pressure gradient and avoiding separation over longer streamwise distances than a laminar boundary layer.

These initial remarks already indicate that a control of the boundary layer state - laminar or turbulent - could be very useful to exploit the respective benefits of each state. The change of state laminar-to-turbulent is known as transition, the reverse process is commonly called re-laminarization. Flow control can refer to either of these processes. The emphasis in the present research is on the possibility of actively delaying transition beyond its natural streamwise position in a boundary layer. The natural transition of a boundary layer is dependent on numerous parameters, the most influential being the Reynolds number, defined by a length scale ($l$), a velocity scale ($u$), the density ($\rho$) and the dynamic viscosity ($\mu$): $Re = \rho l u/\mu$. The immediate benefit of delaying transition is a sustained laminar state; hence a reduction of the frictional drag. However, the flow control devices employed in the present investigations - dielectric barrier discharge plasma actuators - inject momentum into the near-wall region of the boundary layer and this also can be used to delay or even avoid separation of the boundary layer. While this latter effect is not investigated further in the present research, it is a clear example of flow control and one which is equally applicable to both laminar and turbulent boundary layers.

The stability and transition of boundary layers is a complex subject and is not entirely resolved. A complete theory on transition does not exist to-date. Furthermore the ability of low Reynolds number turbulence models to predict transition is contested [6]. For a steady flow, two kinds of boundary-layer transition can be distinguished: natural and bypass transition. The transition type investigated in this study is natural transition, which occurs when a laminar boundary-layer becomes unstable. The background turbulence in the main flow is low for this type of transition to occur. Experiments performed by Schubauer [6] for the flow along a flat plate showed that the boundary layer is laminar when the Reynolds number based on the leading edge distance ($Re_x$) is less than $2.8 \times 10^6$, while it is completely turbulent when $Re_x$ is larger than $3.9 \times 10^6$. In this range the flow is considerable to be transitional.

In 1930, a linear stability theory was developed by Tollmien and Schlichting [7]. This theory predicts the streamwise distance at which small disturbances in the boundary layer become unstable and amplify. These sustained disturbances are known as Tollmien-Schlichting waves (TS-waves). Dependent on local properties, such as the shape of the mean velocity profile and the Reynolds number, these waves are amplified or damped, as described by linear stability theory [8]. Agreement with measurements is found when free-stream turbulence is less than 0.1%. Unstable waves grow in amplitude and far downstream of the leading edge linear theory is no longer valid. During the growth of the waves, spanwise distortions and three-dimensional non-linear interactions become significant. Finally, areas of turbulence, denoted as turbulent spots, start to develop increasingly in the streamwise direction. These spots grow in streamwise and spanwise directions until the flow is completely turbulent and transition is completed.

The second type of boundary-layer transition is called bypass transition. When the free-stream turbulence level is higher than 0.4%, it is assumed that this transition type is dominant [9]. The idea behind bypass transition is that the disturbances in the flow cause fluctuations in the laminar boundary layer, or that disturbances are strong enough to enter the boundary layer and initiate turbulent spots immediately. In both cases the occurrence of Tollmien-Schlichting waves, spanwise vorticity and three-dimensional breakdown is "bypassed", which explains the name. Linear stability theory is irrelevant since in this study the turbulent spots are generated close to the leading edge of a plate compared to natural transition.

Two types of flow control have been used to initiate or influence boundary-layer transition: active and passive. Moving surfaces [10], blowing and suction with periodic excitation [11], among others, are active methods of flow control that induce flow perturbations in the vicinity of the wall. Vortex generators [12], riblets [13] and other methods modify the wall conditions for promoting transition and are considered to be passive methods.

Since turbulence dramatically increases wall friction, maintaining laminar flow by delaying natural transition is often desirable. Comprehensive reviews on transition control can be found in [14], [15], [16]. However, the vast majority of the methods proposed fit into one of two main categories: First, as the shape of the mean velocity profile relates to the growth rates of TS-waves, adding momentum to the near-wall flow usually translates to a transition delay. Second, given the linear character of small-amplitude TS-waves, superposition of artificial, anti-phase waves can reduce the overall wave amplitude and therefore postpone the onset of three-dimensional disturbances. Nevertheless, some other methods have been proposed, such as from Gmelin and Rist [17] where feed-back modified, instantaneous wall shear signals of the flow are used to successfully cancel out even non-linear, three-dimensional disturbances. Recent advances in nonmodal theory [18] enabled Fransson [19] to reduce TS wave growth when applying optimum initial perturbations that can actually be introduced passively, i.e. without additional energy input, by carefully-designed vortex generators.

A variety of actuators or working principles to prevent TS-wave growth has been studied, including most notably, (oscillating) blowing/suction at the wall [20], wall heating/cooling [21], wall motion [10], compliant coatings [22], [23], and body forces [24], [25], [26]. Several numerical results were developed to explain the mechanism of TS-waves growth. Joslin et al. [27] and Joslin, Erlebacher & Hussaini [20] used Direct Numerical Simulations (DNS) to show that wave cancellation was the fundamental reason for the reduction in amplitude of the instability waves. They explained that the wave cancellation was very sensitive to the wave parameters and postulated that incomplete reduction in the controlled motion, reported in the earlier studies, arose from imperfect phase or amplitude properties of the cancelling wave. Gmelin & Rist [17] examined different active approaches in various flow scenarios using both DNS and linear stability theory. The superposition of disturbances with opposite phase on the initial waves in the boundary layer led to a significant attenuation only in linear and weakly nonlinear scenarios. In stages close to transition, where strong nonlinearity has already taken place, the instantaneous feedback vorticity control led to better damping of nonlinear disturbances. Instead of using DNS, Gaster [28] used linear stability theory to investigate the possibility of active control of spatially evolving instability waves in the boundary layer of a flat plate.

Rizzeta and Visbal [29], using Large-Eddy Simulations (LES) and a simple phenomenological model to represent plasma-induced body forces imparted by actuators on the surrounding fluid, solved the flow around a cylinder using pulsed and continuous operation of the actuators, reducing drag significantly. On the other hand, experiments [30] have shown that by appropriate adjustment of the phase and amplitude of the signal driving the control actuator, an order of magnitude reduction in the two-dimensional primary disturbance amplitude could be obtained and significant transition delay realized. However, the downstream wave was never exactly eliminated and some residue remained.

The flow could therefore not be restored completely to its undisturbed state. Recent experimental work of Sturzebecher and Nitsche [31] showed that a sensor-actuator system combined with an adaptive control algorithm could successfully be used to achieve a powerful attenuation of naturally excited two-dimensional Tollmien-Schlichting instabilities on an unswept wing. With a pure two-dimensional control system a local TS-wave was reduced in amplitude by about 90%. They also claimed that three-dimensional instabilities were successfully cancelled by means of a spanwise arrangement of sensors and actuators. In order to study the effect of nonlinearity and three-dimensionality of the travelling disturbances on the performance of active wave cancellation, Opfer et al. [32] developed two different active-control systems in a zero-pressure-gradient laminar boundary layer. By adding nonlinearity or special three-dimensional modelling capabilities to the system, some minor improvements in performance were achieved, but at high computational cost.

During the last decade, many techniques to control disturbances in the flow were improved. One of the most current techniques applied to realize flow control is the dielectric barrier discharge (DBD) plasma actuator. In order to characterize the plasma-air interaction induced by a DBD plasma actuator, several theories have been developed. Plasma can be described as an ionized gas which contains a considerable portion of free charges, such as ions and electrons.

The timescales in which the relevant processes take place range from picoseconds for the plasma-relevant processes to seconds for the processes relevant to the fluid flow. Also the spatial scales range in dimensions, according to the temporal scales involved. The simulation of the plasma-air interaction is therefore very demanding, not only due to the necessary high temporal and spatial resolution but also due to the fact that the number of the chemical processes within the ionized air can reach one hundred or more, depending on the required accuracy. Several authors developed reduced-order kinetic models to simulate the force production of DBD plasma actuators on a physical basis: Roy et al. [33],[34], Boeuf et al. [35], [36], [37] and Likhanskii et al. [38], [39], to name only a few.

While classic control methods, such as boundary-layer suction, are limited to some sort of flow modification at the wall, the plasma actuator can act directly within air flows as a body force. In previous work [40], the potential to delay transition to turbulence has been demonstrated. Two methods have been developed, each employing different operational modes of the actuators. The first method uses continuously-operated actuators: by modifying the mean velocity profile; hence, stabilizing the laminar boundary layer [41], disturbances are locally damped. The second approach uses pulsed actuator operation to directly cancel out the TS-waves [42].

Numerical investigations and experimental results conducted at the Institute of Fluid

Mechanics and Aerodynamics of the Technische Universitaet Darmstadt have shown great success in delaying transition from laminar to turbulent for boundary-layer flows. Grundmann [26] paved the way for active Tollmien-Schlichting wave cancelation (AWC) in his experiments conducted on an adverse pressure gradient, flat-plat boundary layer. He demonstrated that a pulsed-operation of the plasma actuator together with feedback control systems can be used to cancel or damp wave-like disturbances. Thus transition to turbulence could be delayed and friction drag was notably reduced. A semi-empirical and calibrated numerical model of the body force generated by the plasma actuator was used for numerical investigations of the same flow geometry. The obtained results enabled deeper and more detailed insights into flow-control mechanisms. The wave cancelation was also observed in numerical simulations and could be clearly depicted.

The influence of materials, electrical parameters and geometry of the actuator such as electrode size, thickness and electrode gap were not considered in previous work. Instead, the actuator has been represented numerically by an equivalent body force distributed in space. Such influences and a more detailed overview of the actuator's working principle is given by Boeuf [35] and Likhanskii et al. [38].

## 1.2 Optimization of control problems

An optimization approach to flow-control problems has been addressed by a number of authors. Bewley & Liu [43] showed that the instabilities in channel flow could be suppressed by applying suitable active boundary value control in response to some measurable function on the surface. This theoretical approach was then validated by numerical modelling. This idea has been also applied to spatially-evolving boundary layers by Högberg and Henningson [44] where the linear optimal control theory was used to determine an estimator-based feedback to maintain laminar flow. Numerical modelling has shown the power of this approach in significantly reducing the level of the disturbances. The feasibility of applying these control strategies to real flows has been discussed by Bewley [45], but practical implementation seems only likely in the future, as sensors and actuators become available.

To-date several detailed investigations concerning the optimization of the plasma actuators have been performed. Parameters like the operating voltage, the operating frequency, the waveform, the electrode widths and their ratio, the dielectric material and the width of a horizontal gap between the electrodes has been varied and their influence investigated [46], [47]. Most parametric studies concentrate on the energy efficiency, the effectiveness of the actuator, or the maximal flow velocity achieved in the wall jet. However, these optimization objectives are not the only relevant parameters for boundary-layer experiments. For further design criteria and optimization, objective functions have to be defined and a robust and generic algorithm must be developed to find the best parameters for each particular case.

Due to the high level of disturbances and the extreme difficulty in evaluating the derivatives of objective functions in the simulations, the use of methods for unconstrained optimization becomes essential in the optimization for the cancellation of TS-waves using plasma actuators. Algorithms for unconstrained optimization have been used extensively to solve parameter estimation problems for almost 40 years [48]. They remain the method of choice for many practitioners in the fields of statistics, engineering and the physical and medical sciences because they are easy to code and use. The crucial issue is finding a better answer quickly. The asymptotic convergence property is in some cases irrelevant. In fact, a frequent aim in the applications is improvement rather than direct optimization.

To minimize or improve a function with these characteristics many researchers have used simplex-based direct search methods, attaining high effectiveness. Spendley, Hext and Himsworth [49] first developed simplex-based methods almost 50 years ago. These methods construct an evolving pattern of $n+1$ points in $\mathbb{R}^n$ that are viewed as the vertices of a simplex[1]. The most famous simplex-based direct search method was proposed in 1965 by Nelder and Mead [48], based on the idea of Spendley et al. [49]. The idea is that the new simplex is formed at each iteration by reflecting away from the vertex with the largest value of the objective function $f$, or by contracting toward the vertex with the smallest value of $f$. With this approach, the angles of every simplex remain the same throughout, even though the simplex may grow or decrease in size.

In the present work the algorithm of Nelder and Mead [48] is also considered because it has become the most popular simplex method in practice for unconstrained optimization. The Nelder-Mead method is a pattern search algorithm that compares in each iteration the functional values at the vertices and generates a new simplex by replacing the worst vertex by a new one [48]. Powell [3] includes an excellent discussion of the limitations, disadvantages, successes and developments of the Nelder and Mead algorithm. The fact that literature searches show that it is the most widely-used method for unconstrained optimization in practice is remarkable because some severe cases of failure have been found. Mckinnon [50] analyzed the behavior of the Nelder-Mead simplex method for a family of examples, which cause the method to converge to a non-stationary point. All the examples use continuous functions of two variables. In the cases where they had imperfections, the simplex defining the possible search directions became degenerate, restricting the search to a subspace [51].

Powell [52] recently investigated the use of quadratic models of the objective function in unconstrained calculations, which is also a derivative-free method. Good efficiency can be achieved using only $2n+1$ conditions at a time, although a quadratic polynomial has $\frac{1}{2}(n+1)(n+2)$ degrees of freedom. This new unconstrained optimization algorithm called NEWUOA is a method for unconstrained optimization without derivatives, in which the local minimum of an objective function $F(x)$ is calculated by building a quadratic model. This algorithm is based on a trust-region method. In comparison with the other descent methods, trust-region methods are more suitable for the cases where $f(x)$ is non-convex and ill-conditioned. Under some mild conditions it can be proven that the sequence of points $x_k$ generated by the trust-region method converge to a point which satisfies both the first-and the second-order necessary conditions. The theorems about the general trust-region and details of this proof can be found in Shiquan [53].

## 1.3 Aim and procedure of the present investigation

Recently, DBD plasma actuators have been successfully used for flow control applications [26]. They generally offer the advantage that flow manipulation can be achieved without the introduction of mechanically moving parts. The body force which a DBD plasma actuator introduces to the flow field is determined by a variety of operating parameters and it is known that the control performance of the actuator strongly depends on these parameters [54]. The aim of the present investigation is the development of optimization tools that can be employed to determine the optimum operating parameters for a specific control goal. Such a tool will be highly valuable for a wide range of possible applications, since the operating conditions of the plasma actuator are presently determined on a trial-and-error basis. The exemplary control case chosen is the damping of TS-waves resulting

---

[1] A simplex method in two dimensions is a triangle; a simplex in three dimensions is a tetrahedron; etc.

in a delay of the laminar to turbulent transition. From experimental investigations it is known that plasma actuators can be used to successfully damp TS-waves in a flow field [30].

In the present investigation, large eddy simulations (LES) of a flat-plate boundary layer are carried out in which the effect of the plasma actuator is introduced as a body force in the near wall region according to different existing model formulations. In order to be able to use the above-mentioned experimental data as a reference, the simulation is set up to resemble the experiment, in which a TS-wave is introduced into a flat-plate boundary layer by means of a mechanical exciter.

Different optimization methods are implemented and tested to evaluate their performance with respect to the determination of the optimum operating parameters for active cancellation of the TS-waves. The focus is placed on the Nelder-Mead-type method [48] for finding a local minimum of a function of several variables and the trust-region method NEWUOA [52] based on quadratic models for derivative-free minimization, that was performed by J. Elsemüller in [4]. The direct search and unconstrained optimization are methods which have the advantage of finding the best parameters quickly without evaluating the derivatives. Finally, the optimization scheme which is most efficient in the numerical experiments is transferred to the wind-tunnel experiment in order to test its feasibility in practice.

The structure of the present thesis is as follows:

In Chapter 2 a brief theoretical background on transition and turbulent boundary layers is given. Some concepts of linear stability, transition to turbulence and the fundamental equations necessary to perform numerical investigations using Large Eddy Simulation (LES) will be discussed in this chapter.

In Chapter 3 some numeric terms and concepts will be explained, such as the computational grid; the discretization of the partial differential equations into a solvable algebraic form; the temporal discretization; the boundary conditions; the computational code used; the convergency criterion and the initial conditions.

In the next Chapter, the physical and mathematical principle of dielectric barrier discharge plasma actuators as represented by two different phenomenological models will be presented.

In Chapter 5 the results obtained with the continuously-operating mode of the control actuator will be presented. Two different test cases are examined. The first test case uses two control actuators and is compared to experimental results and numerical simulations using Direct Numerical Simulations (DNS). The second test shows the results using only a single control actuator and a comparison between two different phenomenological models.

The optimization procedures and the results obtained by applying these procedures to actuators operated in pulsed mode will be presented in the Chapter 6. Hereby the two optimization approaches Nelder-Mead and NEWUOA[2] which was will be discussed as well as an existing closed-loop control already implemented experimentally. Active wave cancelation using rectangular and sinusoidal modulations of the pulsed actuator signal will be described in this chapter. Finally, the optimal parameters found by the three optimization methods will be interpreted in terms of results obtained using linear stability theory applied to the boundary layer.

Summarizing, the scope of this work follows the schematic outline given in Fig. (1.1).

---

[2] The quadratic model NEWUOA developed by Powell [52], was conducted by J. Elsemüller [4] in the Institute of Mathematics at TU-Darmstadt.

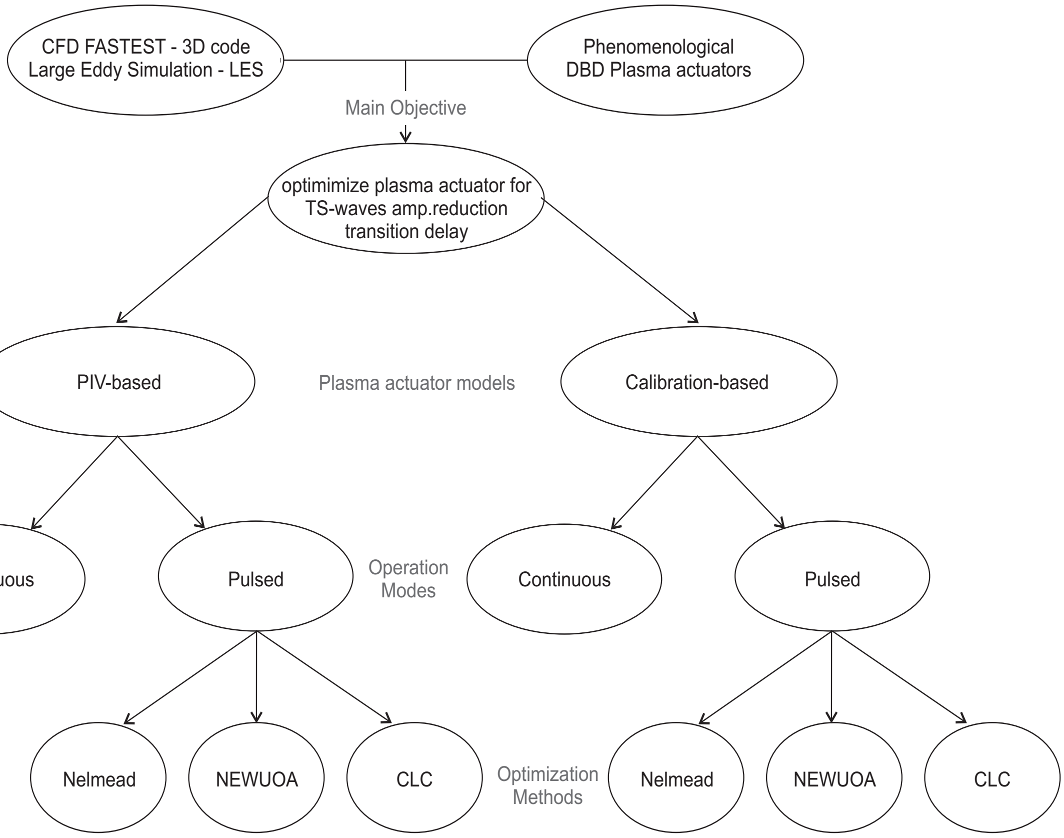

Figure 1.1: Schematic outline of the present work.

# 2 Theoretical Background

The objective of this chapter is to provide a theoretical background to accompany the topics treated in this study. More detailed information on these topics can be found in the textbooks [55], [56], [57], [7] and [58].

## 2.1 Fundamental equations

The conservation equations for fluid flow are based on the principles of conservation of mass, momentum and energy. They can be represented in both differential and integral form. In this work, one assumes that the flow is incompressible and the temperature differences between the surface and free-stream are small so that the fluid properties such as density $\rho$ and kinematic viscosity $\nu$ in the conservation equations are considered constant. This assumption allows us to direct our attention to the conservation equations for mass and momentum and ignore the conservation equation for energy. Thus, the governing equations for laminar, transitional and turbulent flows are given in a non-dimensional form by:

$$\partial_{x_i} u_i = 0 \tag{2.1}$$

$$\partial_t u_i + \partial_{x_i}(u_i u_j) = -\partial_{x_i} p + \partial_{x_j} T_{ij} + F_i, \tag{2.2}$$

where $u_i$ $(i = 1, 2, 3)$ are the velocity components, $F_i$ the external body forces, $p$ is the pressure and $t$ the time. The external body forces represented by the plasma actuators will be specified in Chapter 4.

According to the hypothesis of Stokes, the stress tensor $T_{ij}$ for a Newtonian fluid can be represented as

$$T_{ij} = \rho\nu \left( \partial_{u_j} x_i + \partial_{u_i} x_j \right) - \frac{2}{3} \rho\nu \partial_{u_k} x_k \delta_{ij}. \tag{2.3}$$

The Kronecker delta $\delta_{ij}$ is 1 if $i = j$ and 0 otherwise. Thus, assuming incompressibility, the second term of equation (2.3) disappears, and this equation, inserted into the momentum conservation equation (2.2), leads to the following continuity and Navier-Stokes equations:

$$\begin{aligned} \partial_{x_i} u_i &= 0 && (2.4) \\ \partial_t u_i + \partial_{x_i}(u_i u_j) &= -\partial_{x_i} p + \partial_{x_j}(2\nu S_{ij}) + F_i && (2.5) \end{aligned}$$

where the shear stress tensor $S_{ij}$ is defined by

$$S_{ij} = \frac{1}{2} \left( \partial_{x_i} u_j + \partial_{x_j} u_i \right). \tag{2.6}$$

Equations (2.4) and (2.6) represent a system of equations with four equations and four unknown quantities. The unknown quantities are the pressure and the three velocity components. With this system of equations and the appropriate boundary conditions the flow field can be completely described.

## 2.2 Transition to turbulence

The concept of transition was implicitly introduced by Landau in 1944 and later revised by Ruelle and Takens in 1971 [59]. According to Landau, turbulence is reached at the end of an indefinite superposition of successive oscillatory bifurcations, each bringing its unknown phase into the dynamics of the system. In contrast, Ruelle and Takens mathematically showed that Landau's assumption of quasi-periodicity is not universal when nonlinearities are acting. They identified turbulence with the stochastic regime of deterministic chaos characterized by long-term unpredictability due to sensitivity to initial conditions and only reached after a finite and small number of bifurcations.

### 2.2.1 Physical scenarios

From a physical viewpoint, one can distinguish between open and closed flows when describing transitional flows. Open flows are characterized by a global transfer of matter from upstream to downstream. In this case the transition depends on whether perturbations can be sustained against the convective flow stream and develop into turbulence while staying at a fixed location in the laboratory frame, or whether they are wiped out by the stream and can, at most, amplify perturbations at the entrance, either controlled or uncontrolled (residual noise). Observing sustained turbulence at a given place depends on the amplitudes of the perturbations. Reducing the perturbation amplitude delays turbulence until further downstream. On the other hand, in closed flows, characterized by the presence of lateral boundaries in all space directions, the instability mechanisms must involve a feedback between the fluid velocity field and other flow fields, e.g. pressure. Such instabilities usually introduce an intrinsic length scale in the flow, leading to the formation of dissipative structures [60]. The scenarios leading to turbulence depend on the relative width of the experimental cell compared to the length scale, which measures the strength of confinement effects.

In this work, simulations of closed flows are performed and the presence of solid walls is essential to the dynamics of such bounded flows. Absence of inflection points in the base flow profile explains that the instability, if any, must rely on the Tollmien-Schlichting mechanism, a counter-intuitive linear feedback in which viscosity plays a destabilizing role. Involving infinitesimal perturbations, such an instability is only possible at large values of Reynolds number ($Re$). This leaves room for sustainable, nonlinear finite amplitude departures from the base state at more moderate values of $Re$. The general mechanism sustaining this non-trivial state involves streamwise vortical perturbations generating alternatively slow and fast streamwise streaks [61]. This linear lift-up mechanism is next closed by a nonlinear feedback that regenerates the vortices. The transition in bounded shear flows typically follows a globally sub-critical scenario marked by the not yet fully understood coexistence of spots filled with turbulent flow scattered amidst laminar flow. The same regeneration cycle is expected to hold inside the turbulent spots. These turbulent spots are convected in the downstream direction and grow in all three dimensions. When they overlap each other and merge, a completely turbulent boundary layer is formed.

### 2.2.2 Linear stability

Transition in fluid dynamics describes the process in which a flow changes its state from laminar to turbulent. It is common sense that laminar-turbulent transition originates from a stability problem based on the idea that some small disturbances in a laminar base flow grow and eventually lead to a change of the flow regime. If small disturbances attenuate, the flow is considered stable. Otherwise, if the disturbances grow and cause the laminar flow to change into a different state, the flow is considerable unstable. Instabilities may lead to a different, more complicated laminar state or they may trigger transition, the onset of turbulence. The understanding of the stability problem is crucial since it initiates the transition to turbulence. It is thus desirable to develop and implement a method for practical analysis of shear flow stability properties. The knowledge of particular stability properties of a flow can be used for laminar flow control applications.

In order to define stability of a flow a convenient measure is given by the kinetic energy of the disturbance motion. Symbols with an apostrophe are used in the following to denote disturbance quantities whereas capitals are used to denote the base-flow quantities. Therefore the resulting flow has e.g. the two-dimensional velocity and pressure components given by

$$u = \bar{u} + u', \quad v = \bar{v} + v', \quad p = \bar{p} + p'. \tag{2.7}$$

In accordance with Henningson [16], the disturbance energy of the flow contained in a defined volume is given by

$$E_s = 0.5 \int_v ||\bar{u}|| dV. \tag{2.8}$$

Using this disturbance energy it is possible to clarify some stability definitions. A solution $U_i$ of the Navier-Stokes equations is considered stable if

$$lim_{t \to \infty} \frac{E_s(t)}{E_s(0)} \to 0. \tag{2.9}$$

If there exist some threshold energy $E_t$, which has to be overcome before instabilities grow, the solution $U_i$ is denoted conditionally stable, i.e. $\exists\, E_t : E_s(0) < E_t \Rightarrow$ Eq. 2.9 holds. If $E_t \to \infty$ the conditional stability is denoted as global stability. If $\frac{dE_s}{dt} < 0,\ \forall t > 0$ the stability is monotonic. This present study has a particular focus on finding the threshold, where a flow is no longer conditionally stable. The condition $E_s(0) = E_t$ is fulfilled in the critical state. This stability theory is fundamental to evaluate the critical state of the flow, where the flow changes from the laminar to transitional regime.

Another aspect of concern is the mode of the instabilities. Rayleigh in 1880 described the amplification, phase speed and amplitude distribution of harmonic oscillations as a function of frequency, using an inviscid stability equation, i.e. the effect of viscosity can be neglected. From the analysis of this equation two important theorems were derived. The first states that the existence of an inflexion point in the velocity profile is a sufficient condition for amplification of the disturbances. As a result, a velocity profile with an inflexion point is unstable. So, at infinite $Re_x$ all boundary layers in a positive pressure gradient are unstable to disturbances, because the existence of an inflexion point is directly related to a streamwise increasing pressure. Once this criterion is known it provides a rough classification of all laminar flow on the basis of the pressure gradient.

The other theorem from Rayleigh states that the propagation velocity of neutral disturbances in a boundary layer is smaller than the edge velocity. This layer is called critical-layer $y = y_c$, where the phase speed of neutral disturbances is equal to the local mean velocity of the flow, i.e. $\bar{u}(y_c) = c_r$.

Almost 30 years later, Orr and Sommerfeld extended the Rayleigh equation to include the effects of viscosity. The viscosity stability equation is described by Schlichting, i.e. [7]

$$(\bar{u} - c)(\phi'' - \alpha^2 \phi) - \bar{u}'' \phi = \frac{i}{\alpha Re}(\phi'''' - 2\alpha^2 \phi'' + \alpha^4 \phi). \tag{2.10}$$

The governing linearized disturbance equations, i.e. the dimensionless system of equations consisting of the Orr-Sommerfeld and the Squire equations

$$\left[(-i\omega + i\alpha\bar{u})\left(D^2 - k^2\right) - i\alpha\frac{d^2\bar{u}}{dy^2} - \frac{1}{Re}\left(D^2 - k^2\right)^2\right]\hat{v} \;=\; 0 \tag{2.11}$$

$$\left[-i\omega + i\alpha\bar{u} - \frac{1}{Re}\left(D^2 - k^2\right)\right]\hat{\Omega} \;=\; -i\beta\frac{\mathrm{d}\bar{u}}{\mathrm{d}y}\hat{v}, \tag{2.12}$$

are solved numerically using a Chebychev collocation method based on a Gauss-Lobatto grid [5]. The velocity amplitude function $\hat{v}$ is described in wall-normal direction and $k(\alpha, \beta)^T$ is the wave number vector. Due to the excitation actuators mode of operation, two-dimensional wave-like disturbances are developed in the base flow. Thus, the dispersion relation

$$D(\alpha, \beta, \omega, Re) = 0 \tag{2.13}$$

reduces to a two-dimensional problem ($\beta = 0$). The resulting eigenvalue problem is solved for the spatial framework, using the complex streamwise wave number $\alpha = \alpha_r + i\alpha_i$. In Eq. 2.10, $c$ is the parameter given by

$$c = \frac{\beta}{\alpha} \;=\; c_r + ic_i, \tag{2.14}$$

where the quantity $\beta$ is complex $\beta = \beta_r - i\beta_r$, $\beta_r$ is the circular wavenumber of the mode and $\beta_i$ is the amplification factor and determines if the mode is amplified in the boundary layer or if it dies away. The quantity $\alpha$ is real and is the spatial wavenumber, while $\lambda = 2\pi/\alpha$ would be the wavelength of the perturbation. Equation (2.10) has been cast in dimensionless form by dividing all small scales by the displacement thickness $\delta_1$ and dividing all velocities by the outer, free-stream velocity $u_\infty$. The primes denote differentiation with respect to the dimensionless wall distance $y/\delta_1$. In addition to the Reynolds number

$$Re_{\delta_1} = \sqrt{\frac{u_\infty \delta_1}{\nu}}, \tag{2.15}$$

the only feature of the base flow entering the Orr-Sommerfeld equations is the mean velocity profile $\bar{u}(y)$ and $\bar{u}" = \frac{d^2u}{dy^2}$. The stream function of a single two-dimensional harmonic disturbance is given by

$$\psi(x, y, t) = \phi(y)e^{i(\alpha x - \omega t)}, \tag{2.16}$$

with $x$ and $y$ denoting the streamwise and wall-normal coordinates respectively and $t$ the time. The spatial amplification is used in the current work. Thus, the circular frequency $\omega = 2\pi f$ is real, the wavenumber $\alpha = \alpha_r + i\alpha_i$ is complex and the amplitude varies with streamwise distance $x$ as $e^{-\alpha_i x}$. For $-\alpha_i < 0$ disturbances with frequency $\omega$ are damped and the laminar flow is stable to these disturbances, whereas for $-\alpha_i > 0$ the disturbances will be amplified in the streamwise direction. For a given flow with specified mean velocity profile $u(y)$ at a streamwise position $x$, the Reynolds number $Re_x$ is specified ($Re_x = \sqrt{u_\infty x/\nu}$). When the frequency $\omega$ of the disturbance is given, the Orr-Sommerfeld equation can be solved and provides the eigenfunctions $\phi(y)$ and eigenvalues $\alpha_r$ and $\alpha_i$ for each pair of values $Re_x$ and $\omega$. The Fig. (2.1) presents the eigenvalues of the Eq. (2.10) for a given laminar flow $u(y)$.

The stability diagram describes the three possible states of a disturbance at a given $Re_x$; damped $\alpha_i > 0$, neutral $\alpha_i = 0$ or amplified $\alpha_i < 0$. For two-dimensional flows the locus of neutral amplification $\alpha_i = 0$, called the neutral curve, separates the damped region

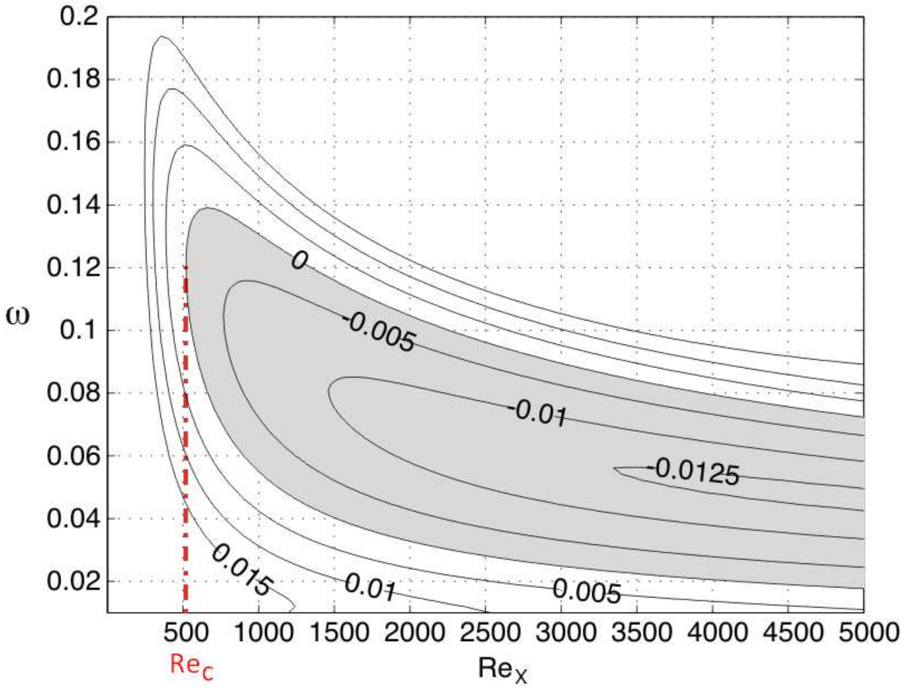

Figure 2.1: Stability diagram: $Re_x$ versus frequency $\omega$. The continuous lines represent rates of constant disturbance growth $\alpha_i$, taken from [5].

(stable) from the amplified region (unstable). The neutral curve consists of two branches, a lower branch where the disturbances of a fixed frequency first becomes unstable for increasing $Re$ and an upper branch, which marks the position where the disturbances become unstable again. The $Re$ below which all disturbances are damped is called the critical Reynolds number $Re_c$. These relations are pictured graphically in Fig. (2.1).

The change in amplitude of a disturbance with frequency $\omega$ in the streamwise direction is given by

$$A = A_0 exp \int_{x_0}^{x_1} - \alpha_i dx, \tag{2.17}$$

with $A_0$ being the disturbance amplitude at $x_0$.

Some results about stability theory applied to boundary-layer flows manipulated by plasma actuators will be presented in Section 7.2, where the author compares two plasma actuator models using this technique.

## 2.3 Turbulence

When a flow is turbulent, the flow contains eddy motions of all sizes and a large part of the mechanical energy in the flow goes into the formation of these eddies, which eventually dissipate their energy as heat. As a result, at a given Reynolds number, the drag of a turbulent flow is higher than the drag of a laminar flow. Also, a turbulent flow is affected by surface roughness, such that increasing roughness normally increases the drag. Some notable exceptions have been demonstrated in recent years, in which structured surfaces such as grooves or riblets can be used to decrease the dissipation rate in the near-wall layer; hence reducing drag [62].

Transition to turbulence can occur over a range of Reynolds numbers, depending on many factors, including the surface roughness, heat transfer, vibration, noise, and other disturbances. To understand why this is so, and to appreciate the role of the *Re* in governing the stability of the flow, it is helpful to think in terms of a spring-damper system such as the suspension system of a car. Driving along a bumpy road, the springs act to reduce the movement experienced by the passengers. If there were no shock absorbers, there would be no damping of the motion, and the car would continue to oscillate long after the bump has been left behind. So the shock absorbers, through a viscous damping action, dissipate the energy in the oscillations and reduce the amplitude of the oscillations. If the viscous action is strong enough, the oscillations will die out very quickly, and the passengers can proceed smoothly. If the shock absorbers are not in good shape, the oscillations may not die out. The oscillations can actually grow if the excitation frequency is in the right range, and the system can experience resonance. The car becomes unstable, and it is then virtually uncontrollable.

In fluid flow, we often interpret the *Re* as the ratio of the inertial force (that is, the force given by mass times acceleration) to the viscous force. At low *Re*, therefore, the viscous force is large compared to the inertial force. Small disturbances in the velocity field, created perhaps by small roughness elements on the surface, or pressure perturbations from external sources such as vibrations in the surface or strong sound waves, will be damped out and not will grow. As the *Re* increases, the viscous damping action becomes comparatively less, and at some point it becomes possible for small perturbations to grow. The flow can become unstable, and it can experience transition to a turbulent state where large variations in the velocity field can be maintained. If the disturbances are very small, or if the wavelength of the disturbance is not near the point of resonance, the transition to turbulence will occur at a higher *Re* than the critical value. So the point of transition does not correspond to a single *Re*, and it is possible to delay transition to relatively large values by controlling the disturbance environment. At very high *Re*, however, it is not possible to maintain laminar flow since under these conditions even minute disturbances will be amplified into turbulence.

Turbulent flow is characterized by unsteady eddy motions that are in constant motion with respect to each other. At any point in the flow, the eddies produce fluctuations in the flow velocity and pressure. The velocity has a time-averaged value $\bar{u}$ and a fluctuating value $u'$, such that $\bar{u}$ is not a function of time.

The eddies interact with each other as they move around, and they can exchange momentum and energy. As they mix, momentum differences are smoothed out. This process is superficially similar to the action of viscosity, which tends to smooth out momentum gradients by molecular interactions. Turbulent flows are sometimes said to have an equivalent eddy viscosity. Because turbulent mixing is such an effective transport process, the eddy viscosity is typically several orders of magnitude larger than the molecular viscosity. The important point is that turbulent flows are very effective at mixing: the eddying motions can very quickly transport momentum, energy and heat from one place to another. As a result, velocity differences are smoothed out more effectively than in a laminar flow, and the time-averaged velocity profile in a turbulent flow is much more uniform over a flow cross-section than in a laminar flow.

As a result of this mixing, the velocity gradient at the wall is higher than that seen in a laminar flow at the same *Re*, so that the shear stress at the wall is correspondingly larger. This observation is in agreement with the fact that the losses in a turbulent flow are much higher than in a laminar flow, and therefore the pressure drop per unit length will be greater, which is reflected in a larger frictional stress at the wall.

### 2.3.1 Statistical description

In order to describe fluid motion in a turbulent flow, a statistical description is used. This assumes that a quantity $\phi$ can be decomposed into a temporal average value $\overline{\phi}$ and a fluctuation $\phi'$, such that

$$\overline{\phi}(x_i, t) = \lim_{T\to\infty} = \frac{1}{2T}\int_{t_0-T}^{t_0+T} \phi(x_i, t)dt, \tag{2.18}$$

$$\phi = \overline{\phi} + \phi', \tag{2.19}$$

whereby the average value of the fluctuation is zero. The averaging has the following characteristics:

$$\overline{\overline{g}} = \overline{g},\ \overline{g+f} = \overline{g} + \overline{f},\ \overline{\overline{g}f} = \overline{g}\,\overline{f}, \tag{2.20}$$

$$\overline{\frac{\partial g}{\partial f}} = \frac{\partial \overline{g}}{\partial f},\ \overline{\int f\,ds} = \int \overline{f}\,ds,\ \overline{g'} = 0. \tag{2.21}$$

After inserting this decomposition into the equations (2.4) - (2.6) and taking a renewed temporal averaging the Reynolds equations are obtained:

$$\begin{aligned} \partial_{x_i}(\overline{u_i}) &= 0 \\ \partial_t \overline{u_i} + \partial_{x_i}(\overline{u_i u_j}) &= -\partial_{x_i}\overline{p} + \partial_{x_j}[\mu(\partial_{x_i}\overline{u_j} + \partial_{x_j}\overline{u_i})] + F_i \end{aligned} \tag{2.22}$$

Applying the Reynolds decomposition and time-averaging to the above equation, followed by the boundary-layer approximations, results in equations for the mean flow in turbulent incompressible boundary layers, the continuity equation and the mean momentum equation read as follows:

$$\partial_{x_i}(\overline{u_i}) = 0 \tag{2.23}$$

$$\partial_{x_i}(\overline{u_i u_j}) = -\partial_{x_i}\overline{p} + \partial_{x_j}[\mu(\partial_{x_i}\overline{u_j} + \partial_{x_j}\overline{u_i})] - \rho\,\partial_{x_i}(\overline{u_i' u_j'}), \tag{2.24}$$

where the total shear stress in the boundary layer is related to the last two terms in equation (2.24). The total shear stress $\tau$ is composed of a viscous and a Reynolds shear stress, i.e. $\tau = \tau_{vis} + \tau_{tur} = \mu\partial_{x_i}u_i$.

The Reynolds stresses $\rho\overline{u_i\prime u_j\prime}$ appear as an additional unknown variable next to the mean flow properties $\overline{u_i}$ and $\overline{p}$ in equations (2.23)-(2.24). As a result, this set of equations cannot be solved without additional information. This is known as the closure problem of turbulence for boundary-layer flow and is usually solved by expressing the new unknowns, the Reynolds stresses, in terms of other existing unknowns, i.e. with the use of turbulence modelling.

### 2.3.2 Considerations near to the wall

In the region closest to the wall the viscous shear layer dominates the total shear stress. Because of the no-slip boundary condition, velocity fluctuations becomes zero at the wall and the Reynolds stresses vanish. Hence, the shear stress on the wall $\tau_w$ will be fully determined by the mean velocity gradient at the wall, i.e. for the two-dimensional case

$$\tau_w = \mu(\partial_y \overline{u})_{y=0}, \tag{2.25}$$

where $\mu$ is the dynamic viscosity ($\mu = \rho\nu$). In dimensionless form the wall shear stress is called the skin friction, written as

$$C_f = \frac{\tau_w}{0.5\rho u_\infty^2}. \tag{2.26}$$

It is evident that close to the wall, the dynamic viscosity $\mu$ and the wall shear-stress $\tau_w$ are important parameters. The appropriate velocity scales and the length scales in the near-wall region are defined by the viscous scales that are given by these parameters. They are the friction velocity

$$u_\tau = \sqrt{\frac{\tau_w}{\rho}}, \tag{2.27}$$

and the viscous length scale

$$\delta_\mu = \frac{\mu}{u_\tau}. \tag{2.28}$$

The friction Reynolds number is defined by $Re_\tau = \frac{u_\tau \delta}{\mu}$. Another important parameter in this analysis is the distance from the wall measured in viscous lengths or wall units, denoted by

$$y^+ = \frac{u_\tau y}{\nu}. \tag{2.29}$$

Different regions in the near-wall flow are defined on the basis of $y^+$, as shown in Fig. (2.2). In the linear sublayer of a turbulent boundary layer a linear dependence of flow speed on wall distance exists, i.e. $U^+ = y^+$, where $U^+ = U/u_\tau$ is the non-dimensional velocity. The buffer-layer is the region where the viscous and Reynolds stresses have the same order of magnitude. In the viscous wall region ($y^+ < 50$), there is a direct effect of molecular viscosity on the shear stress; whereas, in the outer layer ($y^+ > 50$) the direct effect of viscosity is negligible. Within the viscous wall region, in the viscous sublayer ($y^+ < 5$), the Reynolds shear stress is negligible when compared with the viscous stress [63].

Outer scales of the boundary layer depend on the global properties of the flow, e.g. the boundary layer thickness $\delta$, and the velocity at the edge of the boundary layer $U_\infty$. Note that $\delta$ by itself is understood to be the distance from the wall to the location at which the velocity is $0.995U_\infty$.

Between the inner viscous sublayer and the the outer layer, a layer exists in which the Reynolds stresses are dominant over the viscous stresses. This is known as the logarithmic layer ($y^+ > 50$) and the structure of velocity can be expressed in the form of the logarithmic relation $U^+ = 1/\kappa\ ln(Ey^+) + B$, where $\kappa \approx 0.41$ is the von Karman constant, $E = 8.8$ is a constant which determines the degree of a roughness (for a smooth wall) and $B \approx 5$ is a dimensionless constant [64].

In general terms, two types of coherent structures or organized motions can be defined in the turbulent boundary layer. The first is a quasi-cyclical ordered sequence of events in the near-wall region that is responsible for the majority of turbulence production in the boundary layer. The second is a large-scale motion in the outer portions of the boundary layer with a scale on the order of the boundary-layer thickness $\delta$. These two scales of motion are consistent with the two-scale character of boundary-layer flows. When the mean velocity in the outer part of an incompressible flat-plate boundary layer is plotted as $U - U_\infty/u_\tau$ versus $y/\delta$, for different $Re$, the profiles appear to be similar (outer scaling). The same behavior of similarity is noticed when $U/u_\tau$ is plotted versus $y^+$ (inner scaling).

The described regions are usually considered overall as one inner region, which occupies about 20% of the thickness of a turbulent boundary layer and in which about 80% of

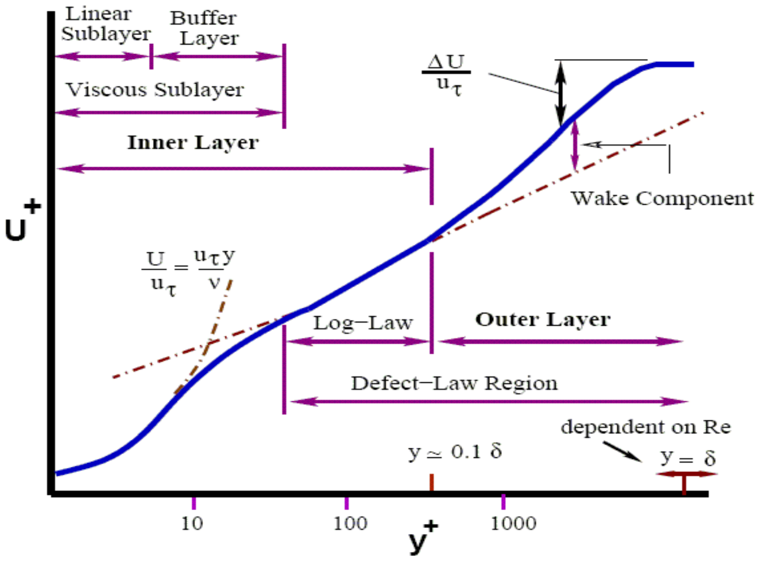

Figure 2.2: Regions of velocity profile of a turbulent boundary layer near to the wall [1].

all energy of turbulence is generated. One of the important properties of the inner region is that the structure of the velocity profile depends only weakly on the *Re*, longitudinal gradients and other external conditions. This property is the basis for the construction of an universal relation, connecting parameters of the flow with the distance from a wall (wall functions). Alongside the universality of the structure of velocity in the inner region, the wall functions method is based on the hypothesis of the local balance of production of turbulent fluctuations with isotropic dissipation of energy in the vorticies, i.e. production is equal to dissipation of turbulent kinetic energy.

## 2.4 Large-Eddy Simulations (LES)

In LES, the larger three-dimensional unsteady turbulent motions are directly represented, whereas the effects of the smaller-scales are modelled. The use of LES to predict transitional and turbulent flows is appealing, since such simulations promise to provide accurate results at greatly reduced computational cost in comparison with fully resolved Direct Numerical Simulations (DNS). However, transitional flows are substantially different from turbulent flows in many respects. Not only is there no fully developed energy cascade[1], but also slow growth and subtly complex iterations between the base flow and various instability modes can affect the physical changeover from the laminar to the turbulence state and must thus be resolved.

In LES, four conceptual steps must be followed [57]: 1) The filtering operation decomposes the velocity $\hat{u}$ into the sum of a resolved component $\overline{u}$ and a residual component $\overline{u}'$. The filtered velocity field $\hat{u}$, represents the motion of the large eddies; 2) The equations for the evolution of the $\hat{u}$ are derived from the Navier-Stokes equations; 3) The closure is obtained by modelling the residual-stress tensor, most simply by using an eddy-viscosity model[2]; 4) and the model filtered equations are solved numerically for $\overline{u}$, which provides

---

[1] The classical Kolmogorov theory of three-dimensional turbulence is based on the concept of energy transfer from larger to progressively smaller scales of motion, known as the energy cascade.

[2] A model of the Reynolds stresses in turbulent flow, which is based on the idea that turbulent mixing, analogous to molecular mixing, is governed by an effective viscosity (the eddy viscosity), which is not a property of the fluid but a consequence of the local state of turbulence.

an approximation to the large-scale motions in one realization of the turbulent flow.

The filtering and modelling are independent of the numerical method, and in particular they are independent of the grid employed. By applying the filter operation

$$\hat{f}(x) = \int_{\Omega} f(x')G(x,x')dx', \tag{2.30}$$

where $G$ is the filter function and $\Omega$ is the entire domain to Eqs. (2.4)- (2.6). The governing equations for the large-scale velocity and pressure can be obtained from:

$$\begin{aligned} \partial_{x_i}\overline{u}_i &= 0 && (2.31) \\ \partial_t\overline{u_i} + \partial_{x_i}(\overline{u}_i\overline{u}_j) &= \partial_{x_i}\overline{p} - \frac{\tau_{ij}}{\partial x_j} + \frac{1}{Re}\frac{\partial^2\overline{u}_i}{\partial x_j \partial x_j} + F_i, && (2.32) \end{aligned}$$

where the non-resolved small scales are given by $\tau_{ij} = \overline{u_i u_j} - \overline{u}_i\overline{u}_j$, which must be modelled, because the filtered quantities $\overline{x_i}$ cannot be obtained alone. $\tau_{ij}$ must thus be modelled by an appropriate sub-grid scale (SGS) model. Then $\epsilon_{SGS} = \tau_{ij}\overline{S}_{ij}$ is the energy dissipation due to the SGS stresses $\tau_{ij}$, with the large-scale strain rate

$$\overline{S}_{ij} = \frac{1}{2}\left(\frac{\partial\overline{u_i}}{\partial x_j} + \frac{\partial\overline{u_j}}{\partial x_i}\right). \tag{2.33}$$

The energy dissipation describes the amount of kinetic energy which is dissipated by the SGS model in addition to the viscous dissipation in the physical space.

### 2.4.1 Smagorinsky model

The most well-known fine-structure model was already formulated in 1963 by Smagorinsky [65]. This model is an eddy-viscosity model, where the effect of the subgrid scales is modeled purely as an enhanced diffusivity for the large-scale flow. For the subgrid tensor $\tau^*_{ij}$, a proportionality factor for the turbulent viscosity is used

$$\tau^*_{ij} = -2\nu_\tau\overline{S}_{ij}. \tag{2.34}$$

This factor, the turbulent viscosity $\nu_\tau$, can be deduced from the Prandtl mixing length, whereby velocity gradients are given by

$$\nu_\tau = l^2\sqrt{2\overline{S}_{ij}\overline{S}_{ij}}. \tag{2.35}$$

The longitudinal dimension $l$ is a characteristic length of the small scales and is defined by the Smagorinsky constant $C_s$ and the filter width $\Delta$ as:

$$l = C_s\Delta, \tag{2.36}$$

where the filter width $\Delta = (\Delta x \Delta y \Delta z)^{\frac{1}{3}}$. The magnitude of the strain rate is defined by (2.33).

### 2.4.2 Germano method

The dynamic Smagorinsky model, introduced by Germano, Piomelli and Cabot [66] and slightly modified by Lilly [67], is one of the most popular sub-grid scale models for LES. The dynamic procedure was developed such that the smallest scales resolved by the grid are similar to the non-resolved scales. For this reason a so-called test filter is introduced. The width of this filter $\widetilde{\Delta}$ is larger than the width of the grid $\Delta$.

In this method, the turbulent viscosity for the non-resolved small scales given by (2.34) is modified by

$$\nu_t = C_g \Delta^2 \sqrt{2\overline{S}_{ij}\overline{S}_{ij}}, \tag{2.37}$$

where the constant $C_g = C_g(x, y, z, t)$ is evaluated dynamically. The optimum value varies from flow to flow and that value should be reduced near solid walls to reduce the amount of dissipation introduced by the SGS model. In the present work $C_g$ is evaluated from the dynamic procedure

$$C_g = -\frac{1}{2}\frac{L_{ij}M_{ij}}{M_{ij}M_{ij}}, \tag{2.38}$$

where $M_{ij} = a_{ij}(\tilde{\bar{u}}) - \tilde{a}_{ij}(\bar{u})$ represents the resolved turbulent stress of the scales between $\Delta$ and a coarse $\widehat{\Delta}$ (where $\widehat{\Delta} = 2\Delta$), and $L_{ij} = C_g a_{ij}(\tilde{\bar{u}}) - C_g \tilde{a}_{ij}(\bar{u})$ represents the contribution of the modeled stress of the small structures, where $a_{ij}$ is the tensor of small structures.

The dynamic procedure to obtain the Smagorinsky constant ($C_g$) ensures correct near-wall behavior of the turbulent viscosity, eliminating the necessity to include wall-damping functions. Furthermore, the dynamic Smagorinsky method has been chosen in this work because of the following advantages:

- Self-contained and self-consistent, i.e no need to specify any parameter: this makes the method inexpensive; adds 10-15% to cost (versus constant coefficient Smagorinsky); removes some of the problems associated with the constant coefficient Smagorinsky model but requires a method to stabilize the simulation; eliminates the need to prescribe length scales; no need to choose formula for $\Delta$ with anisotropic grid; dynamic method actually computes $\nu_t$ rather than $C_g$. If $\Delta$ changes, $C_g$ changes automatically to compensate; predicts zero eddy viscosity in laminar regions of the flow.

- No need for near-wall corrections. Thus it models proper near-wall behavior automatically; no need for wall-damping functions; no need to modify for extra strains and the stratification; and rotation effects are automatically included.

- Applied successfully to many flows: for example, homogeneous flows, simple free shear flows, rotating flows, stratified flows, atmospheric boundary layer and others.

- When it works well, it is self-compensating. Suppose that there is too much energy in smallest resolved scales, the dynamic model will increase eddy viscosity; result is the reduction of energy in small scales and opposite behavior if energy is too small.

This method has also some disadvantages. For example, the parameter variation is too large, i.e. the variance is ten times the mean $C_g(x, y, z, t)$ so it produces large negative values of $\nu_t$ and can be negative for long times over sizeable regions, resulting in numerical instabilities. These instabilities can be reduced by involving a refined numerical mesh in the proximity of the walls in order to more fully-resolve the boundary layer.

## 2.5 Direct Numerical Simulations

In Direct Numerical Simulations (DNS), the Navier-Stokes system of equations is solved directly with refined meshes capable of resolving all turbulence length scales including the Kolmogorov scales,

$$\eta = (\nu^3/\epsilon)^{1/4}. \tag{2.39}$$

All turbulence scales ranging from the large energy-containing eddies to the dissipation scales, $0.1 \leq \kappa\eta \leq 1$, with $\kappa$ being the wave number, must be resolved [68]. To meet this requirement, $L/\eta \approx Re^{3/4}$, where $L$ is the characteristic length and $Re$ is the Reynolds number referenced to the integral scale of the flow. This leads to the number of grid points in three dimensions to be proportional to $N = Re^{9/4}$.

The number of grid points required for a channel flow may be estimated in terms of turbulence Reynolds number $Re_T$ [69] as

$$N = (3Re_T)^{9/4} \tag{2.40}$$

with $Re_T = \frac{u_T H}{2\nu}$, where $u_T$ is the shear velocity and $H$ is the channel height.

Similarly, the time step is limited [69] by the Kolmogorov time scale, $\tau = (\nu/\epsilon)^{1/2}$ as

$$\Delta t \cong \frac{0.003H}{u_T\sqrt{Re_T}}. \tag{2.41}$$

These restrictions are clearly too severe for DNS to be practical design tool in industry in view of currently available computer capacity. For instance the turbulent Reynolds number in the present work can be estimated to be of the order of N=66 million, leading to a grid size of 5.6 million points. For this reason only a two-dimensional domain has been calculated using DNS.

# 3 Numerical Procedure

The numerical procedure for simulating flow-fields can be divided into five main steps:

- Specification of the geometrical model;
- Numerical grid generation;
- Discretisation of the conservation equations;
- Solution of the set of equations and
- Evaluation of the results.

The specification of the geometrical model is usually performed with commercial software tools, in this case ANSYS ICEM. The geometry of the problem is then exported in an exchange format (e.g. TBC or GRD) to the grid generation software. A numerical method (flow solver) can then be used to solve the conservation equations on the generated grid.

Although the basic procedure of Computational Fluid Dynamics (CFD) are well established, some problem-specific aspects for the present case are discussed in the following sections.

## 3.1 Numerical grid

The solution of the conservation equations, described in Chapter 2, requires an arrangement of a discrete set of grids or cells in the flow field; their determination for a given body is known as a grid generation and is discussed in this section. The grid generation is necessary to divide the domain of solution in small elements (triangles, quadrilaterals, polygons and tetrahedrons). The set of points generated by the vertices of these polygons is essential to numerical methods, which use finite differences, finite volumes or finite elements for solving the partial differential equations (PDEs).

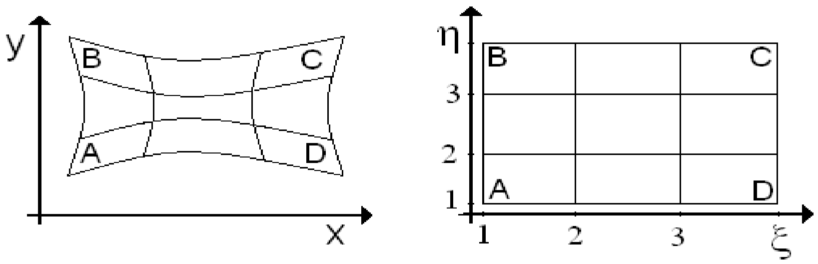

Figure 3.1: Mapping an irregular, simply-connected region into the computational domain; physical plane (left) and computational plane (right).

The numerical grid arrangement predefines the quality of the solution with respect to the geometry, the physics and the numerical accuracy and stability. The generation of the numerical grid can take a large part of the total effort for a numerical solution. Gridding is the process of subdividing a region to be modeled into a set of small control volumes. Associated with each control volume there will be one or more values of the

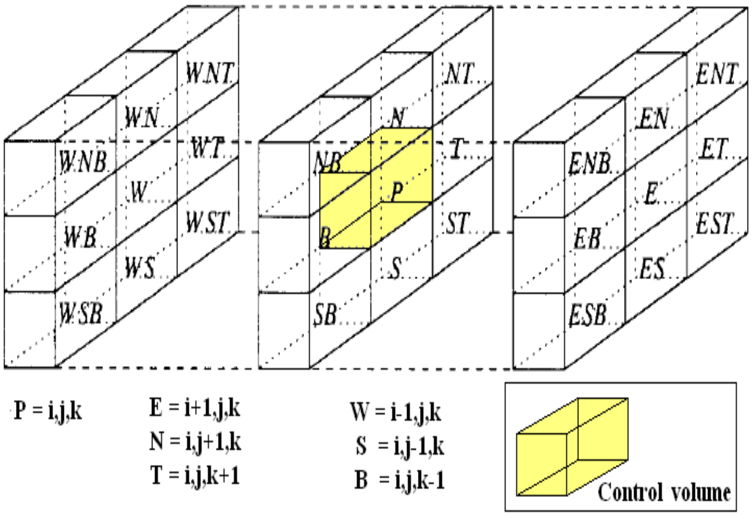

Figure 3.2: Neighboring relations for one control volume [2].

dependent flow variables (velocity, pressure, temperature). Usually these represent some type of locally-averaged values. Numerical algorithms representing approximations to the conservation laws of mass, momentum and energy are then used to compute these variables in each control volume. Some computational schemes use grids that deform to follow the motion of a fluid while others use fixed grids, as the grid used in the current work.

As an example, consider an irregular region ABCDA in the physical plane in the $(x, y)$ cartesian coordinates and determine its mapping into the computational domain in the $(\xi, \eta)$ Cartesian coordinates such that the mapped region will have a rectangular shape and allow the construction of a square mesh as shown in Fig. (3.1). In addition, the boundaries of the physical domain must be coincident with the $(\xi, \eta)$ coordinate lines of the boundary of the transformed region in the computational domain. Furthermore, the mapping must be one-to-one, the coordinate lines of the same family ($\xi$ or $\eta$ must not cross; the lines of different families must not cross more than one). These are important requirements placed on the mapping.

In this thesis, structured grids were used. Regular or structured grids consist of families of grid lines with the property that members of a single family do not cross each other and they cross each member of the other families only once. This allows the lines of a given set to be numbered consecutively. The position of any grid point (or control volume) within the domain is uniquely identified by a set of three indices, e.g. $(i, j, k)$. Each point has six nearest neighbors; one of the indices of each neighbor of a point $P$ (indices $i, j, k$) differs by $\pm 1$ from the corresponding index of $P$, as shown in the Fig. (3.2). The disadvantage of structured grids is that they can be used only for geometrically simple solution domains.

The best choice for a grid system depends on several factors: convenience in generation, memory requirements, numerical accuracy, flexibility to conform to complex geometries and flexibility for localized regions of high or low resolution. The grid arrangement influences strongly the accuracy and efficiency of the numerical method. Essential requirements of the grid arrangement consist of: a clustering of grid points in regions of high gradients (viscous layers, strong gradients, separation zones and plasma actuator position); orthogonality in particular in viscous layers; smooth distribution of step sizes to reduce the order of the truncation errors; and avoiding or at least reducing mesh singularities, e.g. by domain decomposition or block structures. All of these requirements can not be satisfied simultaneously, especially for complex problems. Therefore, compromises must be made, which are in fact reflected in the variety of different mesh concepts and grid refinements. Some grid refinement results are present in the following section.

### 3.1.1 Grid refinement

In this thesis four different grid resolutions were tested to obtain an adequate refinement of the computational grid suitable for executing a Large Eddy Simulation, whereby not only the accuracy of the results was considered but also the computational cost. In table (3.1) a comparison between the grid specifications is given using the mean flow profile from channel flow simulations at low Reynolds number ($Re_\delta \approx 900$). The channel flow simulations were performed using a second-order central difference scheme on a staggered grid with a grid stretching factor of approximately 1.05 in the wall-normal direction without any local coordinate transformation, as shown in Fig. (3.3).

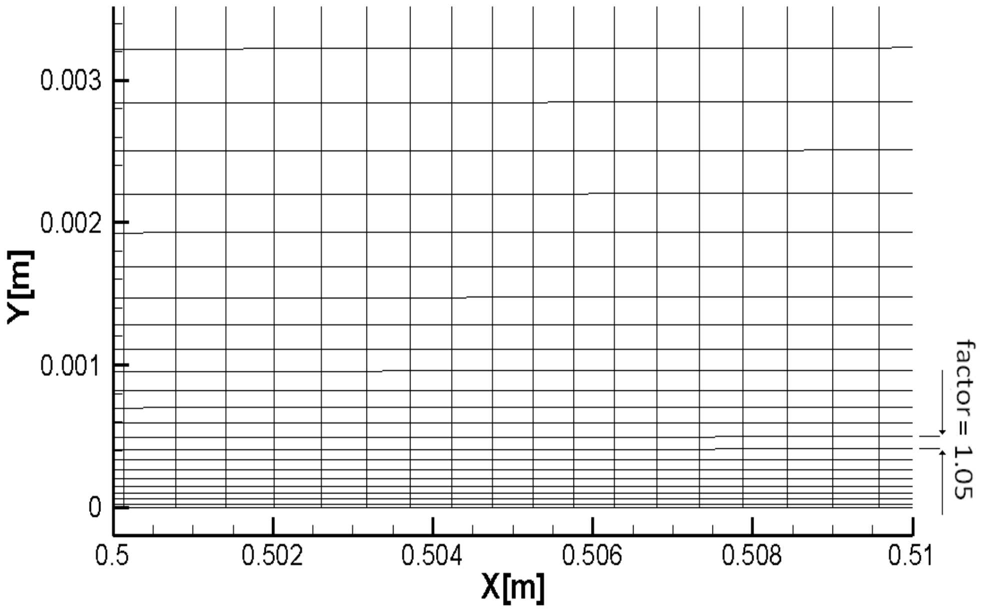

Figure 3.3: Schematic of grid stretching factor.

One of the computational grids used in the current tests is presented in Section 5.2. The first grid uses 480,000 cells and was found to be much too dissipative, resulting in deviations from the known mean velocity profile in the turbulent boundary layer. Using approximately 1 million cells an improvement in the results was obtained; however many instabilities were introduced into the flow using LES, such that small perturbations caused random motions and a diverging solution or a converging solution with large deviations. Using 3 million cells, one obtains the best comparison with results found in the literature. This resolution isn't expensive computationally and presents the same results compared to the finest resolution using more than 6 million cells. The Reynolds stresses and the mean streamwise velocity profile using the dynamic Smagorinsky model (Germano) with different grid resolutions are presented in Fig. (3.4) at x=1.3m downstream of the flat-plate leading edge. These results confirm that grid 3, with approximately three million points is adequate to capture the logarithmic region of a turbulent flat-plate boundary layer.

Table 3.1: Resolution of the computational grids used in LES simulations.

| Grid | resolution | $\Delta x^+$ | $\Delta y^+$ | $\Delta z^+$ | no. of cells |
|---|---|---|---|---|---|
| 1 | 600x50x16 | 66 | 54 | 46 | 480,000 |
| 2 | 1100x50x16 | 38 | 54 | 46 | 880,000 |
| 3 | 1100x90x32 | 38 | 26 | 22 | 3,168,000 |
| 4 | 2200x90x32 | 23 | 26 | 22 | 6,336,000 |

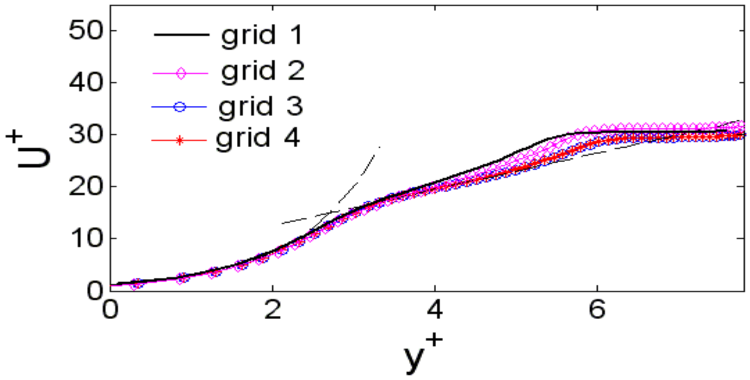

Figure 3.4: Mean streamwise velocity profile in a turbulent flat-plate boundary layer using different grid resolutions.

## 3.2 FASTEST

LES using the dynamic Smagorinsky sub-grid scale model was implemented in the CFD code "Flow Analysis Solving Transport Equations with Simulated Turbulence" (FASTEST). This code solves the three-dimensional, incompressible Navier Stokes equations using a finite volume method on block-structured, unstaggered grids. Pressure-velocity coupling is achieved by the Semi Implicit Method for Pressure Linked Equations (SIMPLE) method [70]. The time discretization is accomplished by applying the 2nd-order implicit Crank-Nicolson method. FASTEST-3D is parallelized based on domain decomposition in space using the Message Passing Interface (MPI) message passing library. MPI is currently the most popular parallel programming approach, which has been accepted as a standard [71]. The user is expected to decompose the computational domain into subdomains with preferably equal number of grid cells. This enables an efficient parallel computation on PC clusters which usually contain processors with the same speed and available memory.

In general, FASTEST-3D is based on the following features [64]:

- Finite-volume discretization method based on hexahedral control volumes;
- Cartesian coordinate and basis vector system;
- Boundary-fitted, non-orthogonal, block-structured grid with matching interfaces and collocated variable arrangement;
- Implicit and semi-implicit temporal, and first-and second-order spatial discretisation schemes;
- In order to obtain an iterative solution, a strongly implicit procedure is used for the linearized equation system;

- Parallelization based on domain decomposition in space using the MPI message passing library.

## 3.3 Finite-volume method

The main objective of the numerical discretization is to convert the PDEs into a solvable algebraic form. There are several approaches to discretization: finite elements, boundary element, finite volume, finite difference, spectral methods, etc. Each has advantages and disadvantages, a discussion of which is beyond the scope of this work.

In this study the finite-volume discretization was chosen because:

- in this method, the discretized equations lead to a balance of the properties at the level of elementary volumes (the wish is to solve the differential conservation equations at the infinitesimal level for each property).
- it is the most widely used method to evaluate flows in general, which underlines the good acceptance and applicability [72].

To examine the numerical solution of the conservation integral equation using the finite-volume approach, consider the generic form of the momentum conservation integral equation given by:

$$\underbrace{\frac{\partial}{\partial t}\int\int\int_{\Omega} U d\Omega}_{convective\ terms} + \underbrace{\int\int_{S} \vec{F}\cdot d\vec{S}}_{source} = \underbrace{\int\int\int_{\Omega} Q_v d\Omega + \int\int_{S} Q_S d\vec{S}}_{diffusive\ terms} \tag{3.1}$$

where according to the usual sign convention for control volumes, positive $\vec{S}$ is perpendicular to the control surface in a direction away from the control volume.

The discretization of the integral conservation equations in the form given by Eq. (3.1) considers the volume $\Omega_{ij}$ as a control volume. The convective terms of Eq. (3.1) become

$$\frac{\partial}{\partial t}\int\int\int_{\Omega} U d\Omega = \frac{\partial}{\partial t}(U_{ij}\Omega_{ij}). \tag{3.2}$$

The source and diffusive terms can be written as:

$$\int\int_{S} \vec{F}\cdot d\vec{S} = \sum_{sides}(\vec{F}\cdot\vec{S}) \tag{3.3}$$

$$\int\int\int_{\Omega} Q_v d\Omega = (Q_v)_{ij}\Omega_{ij} \tag{3.4}$$

$$\int\int_{S} Q_S d\vec{S} = \sum_{sides}(Q_S)_{ij} S \tag{3.5}$$

where the sum of the flux terms refers to all the external sides of the control volume $\Omega_{ij}$. Thus obtains the discretized form of the conservation equation represented by (3.1) as follows

$$\frac{\partial}{\partial t}(U_{ij}\Omega_{ij}) + \sum_{sides}(\vec{F}\cdot\vec{S}) = (Q_v)_{ij}\Omega_{ij} + \sum_{sides}(Q_S)_{ij} S, \tag{3.6}$$

for each cell in the physical space.

In order to implement equation (3.6), it is necessary to divide the physical space into a discrete network of cells. Two kinds of meshes can be used for this purpose, corresponding to structured and unstructured meshes. The use of unstructured meshes require more computer memory and time because the mesh points cannot be represented by a set of integers such as $i$, $j$, but must be numbered individually in a certain order. The structured meshes are efficient to use for simpler geometries, like the geometry used in this research. Thus the structured meshes to describe the numerical solution of Eq. (3.1) with the finite-volume approach are realized. To identify the sides given by Eq. (3.6), it is necessary to use the general notation using the Cardinal points (south,north,east,west) as shown in Fig. (3.5). These cardinal points serve to identify specific cells and do not coincide with a fixed point in space. The points $A$, $B$, $C$ and $D$ represent the fixed points in space, specifying the location of the vertices of the cell denoted by $P$. The cells shown in a two-dimensional $x, y$-plane in Fig. (3.5) are planar quadrilaterals and should be visualized such that each cell has a unit depth perpendicular to the page; hence each cell has a finite volume equal to the area of the cell times the unit perpendicular distance. Therefore, for the cell identified by $P$ the volume denoted by $\Omega_{ij}$ actually refers to the area of the cell $P$.

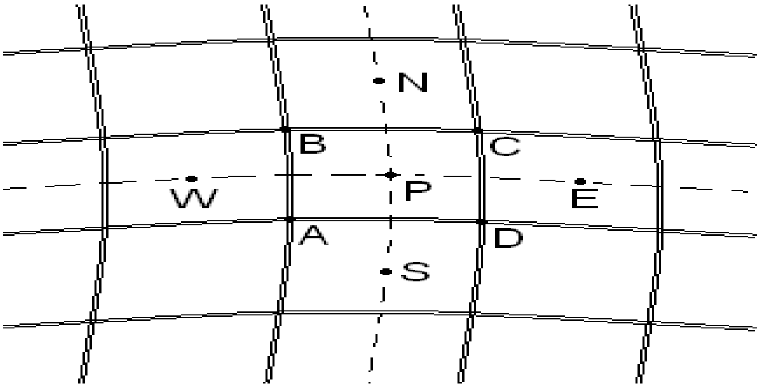

Figure 3.5: Two-dimensional finite-volume mesh system using cell-centered structured arrangement.

## 3.4 Pressure-velocity coupling

The special feature of the momentum equations, distinguishing them from other generic transport equations, is the non-linearity of the convective terms. In the iterative solution a linearization of the convective terms is performed by assuming the mass flux (3.1) through the control volume face to be known and calculated from the velocity values from the previous iteration. Only the pressure gradients contribute to the transport of momentum. A kinematic constraint is used in order to construct the pressure field so that fulfillment of the continuity equation is guaranteed. The pressure-velocity coupling procedure used in FASTEST-3D is that proposed by Rhie and Chou [64] and then further refined by Peric [71]. This procedure was intentionally designed for collocated grids.

For each new outer iteration $m$ the mass fluxes and pressure values from the previous outer iteration $m-1$ are used. The linear equation system given by

$$A_p {\phi_p}^{n+1} - \sum_{nb_1} A_{nb_1} \phi_{nb_1} = S_p n(nb_2) \tag{3.7}$$

for each velocity component $u_i$ can be written as

$$A_p^{u^{m-1}} u_{i,p}^m - \sum_{nb} A_{nb}^{u^{m-1}} u_{i,nb}^m = Q_p^{m-1} - (\delta_i p^{m-1})_p, \tag{3.8}$$

where $nb_1$=E, W, N, S, T, B and $nb_2$=EN, WN, ES, WS, NT, NB, ST, SB, ET, EB, WT, WB, ENT, ENB, WNT, WNB, EST, ESB, WST, WSB, based on Fig. (3.2).

Note that the source term $S_p$ on the right side is decomposed into the pressure gradient denoted here as $(\delta_i p^{m-1})_p$ and the remaining part $Q_p^{m-1}$. The superscripts $u^{m-1}$ emphasize that the matrix coefficients are computed using the velocity field from the previous outer iteration. For a given pressure field $p^* = p^{m-1}$ a velocity field $u^*$ is obtained resolving (3.8) with regard to ${u_{i,p}}^*$ as

$$u_{i,p}^* = \frac{1}{A_p^{u^{m-1}}} \left[ \sum_{nb} A_{nb}^{u^{m-1}} u_{i,nb}^* + Q_p^{m-1} - (\delta_i p^*)_p \right]. \tag{3.9}$$

This field $u_i^*$ satisfies the discretised momentum equation but does not satisfy the discretised continuity equation. An unphysical mass source appearing in each control volume is

$$\Delta m_p^* = F_e^* - F_w^* + F_n^* - F_s^* + F_t^* - F_b^*, \tag{3.10}$$

where the fluxes through the control-volume faces are obtained from the interpolated $u_i^*$ velocity field as $F_e^* = \rho_e u_{i,e}^* b_{i,e}^1$.

In order to satisfy the momentum and continuity equations simultaneously the corresponding velocity field $u_i^{**}$ and pressure field $p^{**}$ are introduced. They are related to the previously calculated *wrong* pressure and velocity fields via corresponding corrections $u_i^{**} = u_i^* + u_i^r$ and $p_i^{**} = p_i^* + p_i^r$. Since both $u_i^{**}$ and $p_i^{**}$ must satisfy the momentum equation, the following expression should be satisfied:

$$u_{i,p}^{**} = \frac{1}{A_p^{u^{m-1}}} \left[ \sum_{nb} A_{nb}^{u^{m-1}} u_{i,nb}^* + Q_p^{m-1} - (\delta_i p_i^{**})_p \right]. \tag{3.11}$$

Here, the neighboring velocity components $u_{i,nb}^*$ and not $u_{i,nb}^{**}$ are used, assuming the difference between $u_{i,nb}^*$ and not $u_{i,nb}^{**}$ to asymptotically approach zero once the method converges ($r \to 0$). Now subtracting (3.8) from (3.11) one obtains the relation between the velocity and the pressure corrections, i.e. $u_{i,p}^r = (\delta_i p^r)_p$. The correction for the mass fluxes $F_e^r = \rho_e (\delta_i p^r)_e b_{i,1}^e$ must satisfy the equation

$$\Delta m_p^* = F_e^r - F_w^r + F_n^r - F_s^r + F_t^r - F_b^r \tag{3.12}$$

in order to remove the mass source $\Delta_p^*$ appearing from the false velocity field $u_i^*$. Rearranging the terms into this expression gives a linear equation for the pressure corrections

$$\Delta m_p^* = A_p p_p^r - \sum_{nb} A_{nb} p_{nb}^r, \tag{3.13}$$

which can be solved using the strongly implicit method.

The procedure used in FASTEST consist of two steps: Eq. (3.8) is solved for a given pressure and velocity field from the previous outer iteration $m-1$, resulting in the estimated velocity field $u_i^*$. The estimated velocity field $u^*$ and the pressure field $p^* = p^{m-1}$ is used in order to interpolate the estimated velocity values at the control-volume boundaries and to compute the mass source $\Delta m_p^*$ according to (3.10) (predictor); and the mass source $\Delta m_p^*$ is substituted into the pressure correction equation (3.13) which is solved, obtaining the pressure correction field $p^r$. This pressure correction field is added to the pressure field from the previous iteration: $p^{**} = p^* + \alpha_p p^r$, $0 < \alpha_p \leq 1$ (corrector). Here $\alpha_p$ is an under-relaxation factor in order to avoid instabilities due to the large pressure changes during the first iterations. The corrected pressure field $p^{**} = p^m$ is used in the next $m-1-st$ iteration.

## 3.5 Time discretization

The momentum-conservation equation is examined in this section. Suppose that the equation is given by Eq. (3.1). The time dependent term is approximated as

$$\int_{v_p} \frac{\partial \rho \phi}{\partial t} dV \approx \frac{\partial}{\partial t} (\rho \phi)_p \Delta V_p, \tag{3.14}$$

where $\Delta V_p$ is the volume of the control volume.

By the approximation specified above one receives the general transport equation in its discretised form for each control volume i:

$$\frac{\partial \rho \phi_{i,p}}{\partial t} \Delta V = -a_{i,p} \phi_{i,p} - \sum_{nb} a_{i,nb} \phi_{i,nb} + Sp, \tag{3.15}$$

where $S_p$ is the explicit part of the solution.

The coefficients are summed, so that one obtains for each control volume with the center $p$

$$a_{i,p} = \sum_{nb} a_{i,nb}. \tag{3.16}$$

In the equation (3.15) the term needs to be discretized. For this the time interval is divided into subintervals $\Delta t_n$. A simplified notation for writing a value of variables at time $t_n$ is obtained using the superscript $n$, i.e.

$$\phi(t_{n+1}) = \phi^{n+1}. \tag{3.17}$$

For the time discretization the Crank-Nicolson procedure is used. One receives this implicit discretisation method, where for each component of the variable $\phi_i$ the time derivative at the time $t_{n+0.5}$ is approximated by the upward gradient of the straight lines between $\phi_i^{n+1}$ and $\phi_i^n$.

For the time-dependent variables $\rho$ and $u_i$ equation (3.15) yields:

$$\begin{aligned} \frac{(\rho u_{i,p} \Delta V)^{n+1} - (\rho u_{i,p} \Delta V)^n}{\Delta t} &= \frac{1}{2} \left[ \sum_{nb} a_{i,nb}^{n+1} u_{i,nb}^{n+1} - a_{i,p}^{n+1} u_{i,p}^{n+1} + S_p^{n+1} \right] + \\ & \frac{1}{2} \left[ \sum_{nb} a_{i,nb}^{n+1} u_{i,nb}^{n} - a_{i,p}^{n+1} u_{i,p}^{n} + S_p^{n} \right] \end{aligned} \tag{3.18}$$

The temporal truncation error of this procedure is of second order.

## 3.6 Boundary conditions

The boundary conditions and sometimes the initial conditions, dictate the particular solutions to be obtained from the governing equations. The applicability of a numerical algorithm can be always assessed based on stability and accuracy considerations. The overall accuracy and physical relevance is determined by the selection and implementation of the boundary conditions. There is a hierarchy of decisions which are to be made when the boundary condition problem is considered. The important aspects of boundary condition development are:

- The physical definition of the flow problem must be satisfied. For example, inviscid flow requires tangency at the solid surfaces, or it may be desirable to specify pressure at the same boundary;
- The physical conditions must be posed in terms of the mathematics of the problem and are numerically approximated, e.g. the no-slip condition for viscous flow is imposed by setting the flow velocities to zero at solid surfaces;
- The interior numerical scheme may require more boundary information than the physics provide. Additional numerical boundary conditions may be necessary. For example, all velocity components and the temperature can be explicitly provided, while the pressure is extrapolated from the interior solution;
- The combination of the interior numerical scheme and the boundary scheme should be checked for stability and accuracy;
- The efficiency and generality of a flow code with boundary conditions must be assessed in terms of its ability to handle a wide variety of problems and flow conditions.

In general, there are two types of boundaries which are provided to solve the Navier-Stokes equations. The first type are natural boundaries, consisting of impermeable walls which may be stationary or moving, and the second type are the flow boundaries, which cut through the flow and are artificially introduced to reduce the size of the solution domain, which otherwise may be infinitely large. Depending on the type of flow and the available information about dependent variables on the boundary, there are a number of flow boundaries, the most commonly encountered being inlets, outlets, periodicity plane and symmetry planes.

In addition, the discrete formulation requires concepts such as characteristic boundary conditions, extrapolation based approaches, and non-reflecting conditions. Methods to specify both physical and numerical boundary conditions for Navier-Stokes equations have been extensively discussed by Poinsot and Lele [73].

### 3.6.1 Wall and tangential velocity

Interaction between the fluid and its solid boundaries is very often of major engineering interest. Therefore, a correct formulation of solid-wall boundary conditions is often essential for the validity of the computations. Here, the boundary condition on a surface assumes zero relative velocity between the surface and the fluid on the surface. This is called the no-slip condition

$$\overrightarrow{u} = \overrightarrow{v} = \overrightarrow{w} = 0, \tag{3.19}$$

as shown in Fig. (3.6).

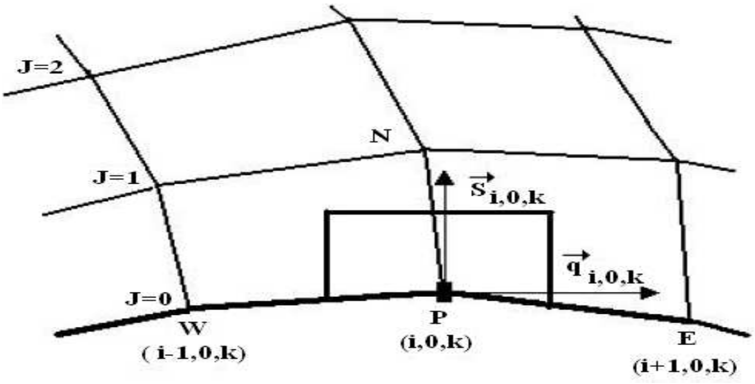

Figure 3.6: Wall-boundary condition.

The tangency condition is necessary if a geometric boundary is to be used for the solution of the Navier-Stokes equations.

As suggested in boundary-layer theory, the wall pressure can be determined by the outer flow, for example, the pressure is considered to be imposed on the boundary layer in that it appears as a boundary condition rather than as an independent variable.

In case of turbulent flows there is a very rapid variation of dependent variables near the solid wall and one has to use a very fine mesh in the near-wall region in order to resolve those rapid variations of the variables. To represent the turbulence structures in the near-wall region the first grid point must be located as close as $\Delta y^{+}{}_{min} \leq 2$ to the wall without wall models and in the streamwise and spanwise direction the grid spacing must be of order $\Delta x^{+} \simeq 15$ and $\Delta z^{+} \simeq 5$, respectively. Piomelli stated in [66] that LES without any wall model can give good results with $\Delta x^{+} \simeq 15-50$, $\Delta z^{+} \simeq 5-15$. In all present simulations the following constraints of $0.5 \leq \Delta y^{+}{}_{min} \leq 1.5$, $0.5 \leq \Delta x^{+}{}_{min} \leq 30$ and $10 \leq \Delta z^{+}{}_{min} \leq 17$ are satisfied.

### 3.6.2 Periodicity

Periodic boundary conditions imply that the computational domain repeats itself an infinite number of times. They are convenient, since they eliminate the need to specify inflow and outflow conditions, and they are easy to implement and efficient, since they allow use of smaller computational domains. The use of periodic boundary conditions is similar to studying the time rather than the spatial development of a flow. If one looks at the spatial evolution of a perturbation in plane channel flow for example, the use of periodic boundary conditions is equivalent to studying the flow in a convecting frame of reference. When periodic boundary conditions are used, the computational domain must be at least as long as the wavelength of the longest structure present in the flow. In the present work a periodic boundary layer in the spanwise direction was used. By using 32 cells in the spanwise direction with a computational domain 0.1mm wide, it was possible to represent the three-dimensional structures of the flow quite reasonably.

### 3.6.3 Outflow

Most turbulent flow simulations have an unbounded spatial domain. Thus, it is necessary to introduce an artificial boundary to make the computational domain finite and thereby reduce the computational time and costs. One needs to impose a numerical boundary condition on this artificial boundary to complete the statement of the problem. In most cases, the boundary condition on the boundaries of a truncated domain is not known a priori. An incorrect specification of the boundary conditions gives rise to spurious reflections, which are entirely numerical in nature. These numerical reflections propagate into the interior domain as the solution progresses in time, eventually contaminating the entire solution. Thus, one needs non-reflecting numerical boundary conditions, which will allow the waves from inside to leave while preventing the occurrence of non-physical waves. A well designed non-reflecting boundary condition should minimize the amount of spurious reflections, minimize the computational effort, and the boundary condition together with the numerical method employed must result in a stable scheme.

In general there are many ways of specifying a numerical boundary condition: using zero-order extrapolation (to supersonic flows); based on the asymptotic solution of the governing equations in the far field, and those based on the characteristics of the governing differential equations. The last two types are designed to minimize the numerical reflections in incompressible flows. The outflow based on the characteristics of the governing differential equations was used in this work because the outflow involves single-directional waves.

### 3.6.4 Inflow

The inflow problem appears to be more troublesome, since in most cases the influence of the upstream conditions persists for large distances downstream. Of course, one way to avoid the problem is to prescribe a small orderly perturbation on an incoming laminar flow and follow the flow through transition to turbulence. However, in addition to more stringent requirements on the treatment of the small-scale motions in transitional flows, the required length of the computational box for the entire process is prohibitively large. This approach has been used in incompressible boundary-layer simulations of [74], [75] and [76]. The use of turbulent inflow conditions appears to be a practical necessity for flows such as those found in boundary layers.

The specification of the inflow conditions for unsteady flows can, however, be more problematic, since the flow variables on the entire inflow plane must be specified as a function of time. If one is interested in turbulent flows, the development of turbulence from perturbed boundary conditions may require excessively long streamwise domains, since turbulence must be allowed to develop from the imposed perturbation.

In this work the laminar inflow velocity profile with free-stream velocity $u_\infty = 8m/s$ was used.

## 3.7 Convergence criterion

The numeric solution of flow problems has some imprecisions, which can be determined by the convergence criterion. The best choice of criteria on which to determine the execution of the algorithm is not an easy decision.

In this study, because one is dealing with a incompressible flow, the relative error in the pressure was used as convergence criterion, which is defined in the following form

$$\varepsilon \geq \sqrt{\frac{\sum \Delta_p^2}{\sum \Delta_{po}^2}}, \tag{3.20}$$

where

$$\Delta_p = \frac{p - p_o}{\Delta t} \tag{3.21}$$

and $\Delta_{po}$ are the values in the first iteration.

In the analysis realized in this research, $\varepsilon = 10^{-4}$ was found to be sufficiently small. Smaller values of $\varepsilon$ increase the computational cost significantly; however, they do not improve the results.

## 3.8 Initial conditions

The initial conditions refer to the values of the flow field at the beginning of the simulation. In the present case, an initial velocity of 8m/s was chosen, corresponding to the experimental values used in the wind tunnel studies. The other initial conditions are presented in Table 3.2.

Table 3.2: Initial conditions used in the simulations

| | |
|---|---|
| streamwise velocity | u = 8m/s |
| wall normal velocity | v = 0m/s |
| spanwise velocity | w = 0m/s |
| turbulence intensity | tu = 0% |
| dynamic viscosity | $\mu = 1.77e^{-05}$kg/ms |
| kinematic viscosity | $\nu = 1.45e^{-05}$ |
| density | $\rho = 1.225$ kg/$m^3$ |
| timestep | $t = 9.1e{-}06$s |

# 4 Plasma Actuator

In this chapter the operating principles of dielectric barrier discharge (DBD) plasma actuators are presented, followed by discussion of two possible simulation models and their calibration.

Dielectric Barrier Discharge (DBD) Actuators, or, in short, plasma actuators, consist of two electrodes. The lower electrode is covered by an insulating film, the dielectric barrier, while the upper one remains blank. A high AC voltage of 10 kV and 6 kHz applied to the electrodes causes the air molecules to break down, creating a weakly ionized plasma above the lower electrode. The charges are accelerated and collide subsequently with neutral air molecules. The ionized air (plasma), in the presence of the electric field gradient produced by the electrodes, result in a body force vector acting on the flow which induces steady or unsteady velocity components. In quiescent fluid, this force creates a wall jet with a velocity of several meters per second (Fig. 4.1). In a boundary-layer flow the actuator can be used to impart momentum into the near-wall layer and to alter the velocity profile [77], the turbulence distribution or to promote transition from a laminar to turbulent state. The momentum transfer occurs very close to the surface of the actuator itself, typically in the viscous sublayer region [78]. Varying the driving voltage changes the amplitude of the induced body force.

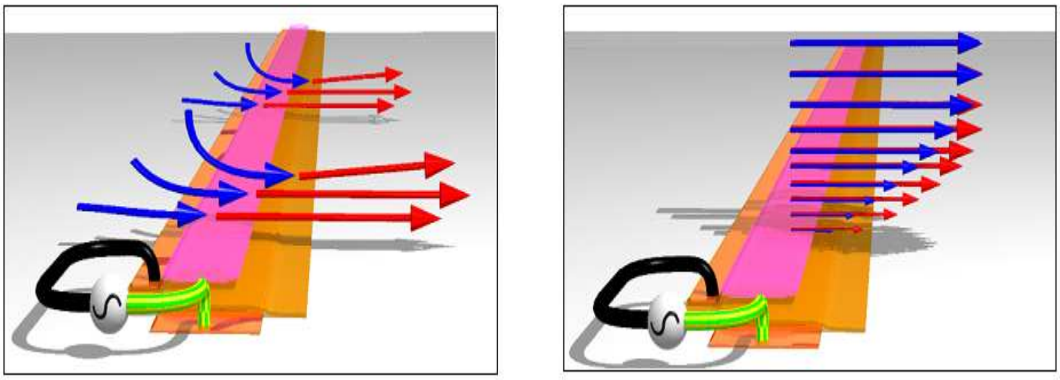

Figure 4.1: Plasma actuator creating a wall jet (left) and modifying boundary-layer profile (right) [30].

## 4.1 The physical working principle

Numerous theories have been put forward to describe the interaction of the plasma actuator with the surrounding gas and flow field. Yet the physics behind the involved processes is not yet fully understood or described in detail. A plasma is a ionized gas, which contains free charge carriers such as ions and electrons to a considerable portion. Plasmas are normally quasi-neutral and are an equipotential particle system in the form of gaseous or fluid like mixtures of free electrons and ions, frequently also containing neutral particles. One characteristic of plasmas is the typical illuminescence, which is caused by radiation emission of lively gas atoms, ions, electrons or molecules. In the present application the plasma actuator influence on the neutral molecules of the carrier gas is of crucial importance. The added energy causes the gas to dissociate as a result of collisions between those particles whose thermal kinetic energy exceeds the molecular binding energy. Based on the extent of ionization, one observes either a fully ionized or a weakly ionized plasma. Weakly ionized plasmas consist partly of ions and electrons and partly of neutral gas particles, i.e., atoms and molecules. Our interest is in weakly ionized gases.

A second classification of plasmas is based on the temperature, i.e. high- and low-temperature plasmas. Low-temperature plasmas can be classified as (i) only the electrons have a large mean kinetic energy, for example, non-thermal plasma, and (ii) all components have a large kinetic energy compared to the neutral gas, i.e., thermal plasma. High-temperature plasmas are characterized by kinetic electron temperatures of $Te \sim T > 10^7 K$. Here, $Te$ is the kinetic temperature of the electron component and $T$, the overall kinetic temperature. Low-temperature thermal plasmas are characterized by a value of $Te \approx T < 23104K$. Finally, low-temperature non-thermal plasmas are characterized by a temperature of $T \approx 300K$ and $Te < 105K$ [79]. In the present study we are concerned with low-temperature, non-thermal plasmas.

The electric field acting on the charged particles, and especially on the electrons, is the main power source for the plasma considered. Owing to the small mass of the electrons, only a low momentum transfer of the electrons with the heavy neutral particles of the plasma is realized by elastic collisions. Consequently, the electrons reach mean kinetic energy levels much higher than those of the neutral and charged heavy components, and the plasma becomes non-thermal. A significant portion of the electrons is energetically capable of overcoming the threshold above which inelastic electron collision processes take place. However, in each of these inelastic collision processes, the corresponding electron loses at least the threshold energy for the process, and the electron is transferred from a region of high kinetic energies to a low-energy region. Thus, the occurrence of inelastic collisions causes an efficient reduction of the electron energy. Consequently, the electron population in the region of inelastic collisions decreases markedly with increasing energy. This interplay between the action of the electric field and the elastic and inelastic collision processes causes the electron component to reach a state far from thermodynamic equilibrium.

According to Enloe et al. [80], when a high-voltage AC source of several kV at several kHz is applied across the electrodes, a localized ionization of the air occurs around the exposed electrode. During the negative phase of the AC cycle, electrons are emitted from the exposed electrode, ionize the local gas, and travel to the dielectric surface through a series of micro discharges. The dielectric surface charge subsequently builds up and opposes the charge on the exposed electrode, inhibiting further emission. Thus the plasma is a self-limiting process [81], which enables the plasma to be formed in air at atmospheric pressure without collapsing into an arc. During the positive half-cycle, electrons travel back from the dielectric to the exposed electrode, completing the chain of events. Regions of net charge density have been shown to exist, particularly near the exposed electrode and near the dielectric surface. Consequently, the electric field will exert a force on the plasma [82].

## 4.2 The mathematical description

The gas movement induced by a plasma can be regarded on different scales: as single particle movement, on microscopic or on macroscopic levels. On the level of the single particle movement one examines how individually charged molecules react to different electrical and magnetic fields. Here the Maxwell equations are the center of attention

[83].

In order to be able to describe the interaction of such particles and also their reaction to given electric fields, a larger number of particles must be regarded. In this way one arrives at the microscopic description. Here an assumption is to be made about the distribution of the charged particles (ionization stages and energy conditions), the so-called distribution function. Thus a detailed description of the individual particles is avoided. For the determination of the distribution function however the complex *Boltzmann* equation must be solved. In thermal equilibrium and with not too high densities for example, the distribution of the particles is described according to their different energy conditions by a Boltzmann statistic $n_a = n_0 e^{-E_a/(KT)}$. In this case, 0 is the initial state, $a$ the excited condition, $E_a$ designates the appropriate excitation energy, $T$ is the absolute temperature and k is the Boltzmann constant.

In similar form, the so-called *Saha* formula describes the equilibrium between ionization and recombination, similar to the mass action law for chemical reactions, i.e. $n_i n_e / n_0 = Ae^{-E_s/(KT)}$, where $i$ represents ion; $e$ electron and $A$ a gas-dependent parameter.

An important approach with the mathematical treatment of particles charged by systems is the *Debye* or *Debye Hückel* theory. Here the *Poisson* equation for the electrical potential Φ is considered, on which the charge pattern depends. With the assumption of thermal equilibrium the particle number density of the charged particle component $g$ can be expressed by the Boltzmann distribution specified above as follows: $n_g = n_{g0} e^{ze\Phi/(KT)}$. Here $z$ is the charged particle number, which indicates the size and the sign of the charge particle as a multiple of the elementary charge $e$. In addition it is accepted that the electrical reciprocal effect energy is small in relation to the thermal energy. This condition implies that $|ze\Phi| << KT$.

In the Boltzmann distribution, the exponent is small and can be expanded into a series, which is truncated after the linear terms. This approximation is known as the *Debye Hückel* approximation . Thus the potential can now be determined. In this way one arrives at a plasma length, also considered a characteristic length in the problem. The potential of such a charged particle corresponds to the well-known Coulomb potential of a ball for distances smaller than the plasma length, while it drops for larger distances exponentially. Due to this spatially limited electrical characteristics special effects and behaviors of the charged particle medium can occur, for example, the electrosmosis in a capillary. Apart from the Debye theory a set of kinematic equations exists, which describe the plasma movement with different assumptions and degrees of simplification. These are for example the *Liouville* equation, the hierarchy equations, the *Wlassow* equation and the *Klimontovich* equation.

Analyzing the plasma actuator on a macroscopic level, it is possible to describe a plasma independently of complicated distribution functions, using instead averaged and/or integrated quantities. For example the density can be regarded as an integral of the distribution function over a volume element. Instead of the speed of each particle one uses an averaged speed according to each component. Using these assumptions, a plasma can be described using the hydrodynamic equations (continuity equation, impulse balance, energy balance, etc.). The plasma is considered then to consist of a multi-component current; electrons, ions and a neutral gas (multi-equation models). In this case the mass conservation is applied to each component separately, and if necessary the chemical reactions taking place between the components is also captured. The number of such components can vary depending upon application. Under the condition of thermal equilibrium it is possible to add the continuity equations for the individual components and over the en-

Table 4.1: Scales involved in DBD actuator modelling [35].

| Temporal | scales |
|---|---|
| Maxwell relaxation time | $10^{-12}$s |
| CFL time - electrons | $10^{-12}$s |
| CFL time - ions | $10^{-10}$s |
| Plasma formation | $10^{-9}$s |
| Voltage generator | $10^{-4}$s |
| Ambipolar diffusion | $10^{-4}$s |
| Generated flow | $10^{-2}$s |
| **Spatial** | **scales** |
| Shealth | $10^{-6}$m |
| Plasma dimension | $10^{-3}$m |
| CFL | $10^{-1}$ |
| Generated flow | $10^{-1}$m |

tire plasma an averaged magnitude for the density to form velocity; hence only one mass balance is necessary. The macroscopic description is therefore the means of choice for the description of the plasma actuator because of its simplicity. The implementation of such a model takes place with the help of electrical hydrodynamics.

## 4.3 Multiscale problem

It is clear from the above discussion, and as discussed in Boeuf et al. [35], the analysis of plasma actuators is a multiscale problem. Table (4.1) summarizes the scales encountered in this context.

It is computationally impractical to capture all scales in a model; hence for the present purposes the macroscopic approach will be adopted, neglecting microscopic effects. In fact, a comprehensive theory bridging the microscopic to macroscopic scales does not yet exist. Therefore two phenomenological models of the plasma actuators will be used.

## 4.4 Plasma actuator models

To numerically simulate the effect of plasma actuators on a flow field two existing models based on experimental results will be used in this work. The first is a phenomenological model developed by Grundmann et al. [84], which is an improvement of the model originally developed by Jayaraman and Shyy [85]. The second model to be implemented was developed by Wilke at the "Deutsches Zentrum für Luft und Raumfahrt (DLR)" in Göttingen [86], who derives a spatially distributed body force from measured velocity fields, as described in more detail below. The first model will be denoted "calibration based model", the second "PIV based model" (Particle Image Velocimetry)

### 4.4.1 Calibration based model

To reduce the computational cost and also simplify the equations involved in the numerical simulations, the calibration based model assumes that the plasma is present only within a triangular region directly above the lower electrode and only inside this region is a body force present. This model has its origins in the Poisson equation and the Coulomb law.

Assume that no interaction exists between the charge density and the electrical field and that ions accelerated by the electrical field pass their entire impulse on to the molecules of the neutral gas. Thus,

$$\nabla \cdot \vec{E} = \frac{\rho_c e_c}{\epsilon_0} \Leftrightarrow \rho_c = \frac{\epsilon_0}{e_c} \nabla \cdot \vec{E} \tag{4.1}$$

where the operator $\nabla = (\frac{\partial}{\partial x}, \frac{\partial}{\partial y}, \frac{\partial}{\partial z})$, $e_c$ is the elementary charge, $\epsilon_0$ is the vacuum permissivity and $\rho_c$ is the charge density. The body force $\vec{f}$, which affects the charge carriers in the electrical field, can be determined by means of the equation

$$\vec{f} = \vec{E} \rho_c e_c. \tag{4.2}$$

Jayaraman et al. [85] assume a linear decrease of the field strength with its maximum at the point the shortest distance between the electrodes, which can be expressed by

$$|\vec{E}| = E_0 - k_1 x - k_2 y. \tag{4.3}$$

where $E_0$ is the electric field above the insulated electrode described in Fig. 4.2. This linear distribution satisfies the Poisson equation with a constant charge density distribution. In general, the constant $E_0$ is large and, $k_1$ and $k_2$ are two positive constants which represent the gradient of electric field intensity along the two mutually perpendicular directions, namely $x$ (streamwise) and $y$ (wall normal). The sign of these two constants ensures that the electric field intensity decreases as one move along the positive directions of the axes [85]. In Eq. 4.3, $E_0$ can be approximated as

$$E_0 = \frac{V}{d}, \tag{4.4}$$

where $d$ is the distance of separation between the two electrodes in the $x$ direction and $V$ is the applied voltage potential.

The scaling parameters $k_1$ and $k_2$ are given by

$$\frac{k_1}{k_2} = \frac{a}{b} \Leftrightarrow \frac{k_1 + k_2}{k_2} = \frac{a+b}{b} \; and \; \frac{k_1}{k_1 + k_2} = \frac{a}{a+b}. \tag{4.5}$$

The distances $a$ and $b$ insure a linear scaling of the force with voltage and distance from the electrodes.

Additionally a linear growth of the triangular domain with increasing voltage is assumed. This leads to an expression for the total force acting on the flow field, which becomes negative at higher voltages. This is not reasonable and results from the fact that the linear decreasing electric field strength becomes negative at a certain distance from its maximum. To avoid this nonphysical behavior, a new distribution of the electric field has been introduced as

$$|\vec{E}| = E_0 e^{m_1 x} e^{m_2 y}, \tag{4.6}$$

in which the field strength approaches zero and does not become negative.

Consider the equations

$$\begin{aligned} \rho_c &= \rho_{c0} \frac{V}{V_0} \\ a &= a_0 \frac{V}{V_0} \\ b &= b_0 \frac{V}{V_0}. \end{aligned}$$

Mathematically, using the Poisson equation to electrostatic, the charge density $\rho_c$ can be written

$$\begin{aligned}
\rho_c &= \frac{\epsilon_0}{e_c}\nabla \cdot \vec{E} && (4.7)\\
&= \frac{\epsilon_0}{e_c}\left(E_0(-m_1)e^{m_1x}e^{m_2y} + E_0(-m_2)e^{m_1x}e^{m_2y}\right) && (4.8)\\
&= (-1)\frac{\epsilon_0}{e_c}E_0\left(\frac{a_0}{a_0+b_0}\frac{\rho_{c0}e_c d}{\epsilon_0 V_0}e^{m_1x}e^{m_2y} + \frac{b_0}{a_0+b_0}\frac{\rho_{c0}e_c d}{\epsilon_0 V_0}e^{m_1x}e^{m_2y}\right) && (4.9)\\
&= (-1)\frac{\epsilon_0}{e_c}\frac{V}{d}\frac{\rho_{c0}e_c d}{\epsilon_0 V_0}\left(\frac{a_0}{a_0+b_0}e^{m_1x}e^{m_2y} + \frac{b_0}{a_0+b_0}e^{m_1x}e^{m_2y}\right) && (4.10)\\
&= (-1)\frac{\rho_{c0}V}{V_0}\left(\frac{a_0}{a_0+b_0}e^{m_1x}e^{m_2y} + \frac{b_0}{a_0+b_0}e^{m_1x}e^{m_2y}\right). && (4.11)
\end{aligned}$$

The gradients of the electric field should be of the same value as in the model of Jayaraman et al. [85]. This leads to the expressions

$$\begin{aligned}
m_1 &= \frac{a_0}{a_0+b_0}\frac{\rho_{c0}e_c d}{\epsilon_0 V_0} && (4.12)\\
m_2 &= \frac{b_0}{a_0+b_0}\frac{\rho_{c0}e_c d}{\epsilon_0 V_0} && (4.13)
\end{aligned}$$

where the geometric constants $a_0$, $b_0$ and $d$ are showed in the Fig. (4.2).

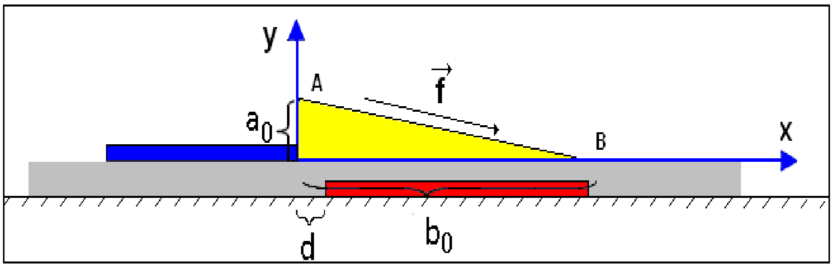

Figure 4.2: Calibration based model scheme.

The field strength still has its maximum at the same point as the linear model, equation (4.3), but has an asymptotic approach to zero and therefore never becomes negative. $m_1$ and $m_2$ are parameters of the model depending on the electrode gap $d$. This distribution leads to the following expression of the body force:

$$\begin{aligned}
\vec{f} &= \vec{E}\rho_c e_c && (4.14)\\
&= \vec{E}e_c\frac{\rho_{c0}V}{V_0}\left(\frac{a_0}{a_0+b_0}e^{m_1x}e^{m_2y} + \frac{b_0}{a_0+b_0}e^{m_1x}e^{m_2y}\right) && (4.15)\\
&= E_0e^{m_1x}e^{m_2y}\frac{\rho_{c0}V}{V_0}\left(\frac{a_0}{a_0+b_0}e^{m_1x}e^{m_2y} + \frac{b_0}{a_0+b_0}e^{m_1x}e^{m_2y}\right) && (4.16)\\
&= \left(\frac{a_0}{a_0+b_0}e^{2(m_1x+m_2y)} + \frac{b_0}{a_0+b_0}e^{2(m_1x+m_2y)}\right)\frac{\rho_{c0}V^2}{dV_0}e_c && (4.17)\\
&= \frac{\rho_{c0}V^2}{dV_0}e^{2(m_1x+m_2y)}\vec{n}e_c && (4.18)
\end{aligned}$$

The normal vector of the volume strength $\vec{n}$ depends on the arrangement of the triangular area and acts constant over the entire all field, specifically in the wall-normal direction.

That means that the body force acts in the same direction. To model the plasma actuator it is necessary to know the voltage $V$ and the electrode gap $d$. The dimensions of the triangular area depends only on the voltage $V$ (linearly) and the geometric arrangement of the actuator. The force is implemented directly in the Navier-Stokes equations.

The model was calibrated using PIV measurements of the wall jet created by a plasma actuator operated at different voltages. The numerical simulations for the calibration have been carried out on a 2D grid of 5500 cells with the SST-turbulence model and the low Reynolds treatment for boundary layers provided by the CFD solver Fluent [84]. The inlet boundary conditions were set to laminar with a turbulent viscosity ratio of unity. The product of the momentum flow rate and the mass flow rate is constant for a wall jet. Therefore it is justified to calibrate the model in terms of momentum flux at a single downstream position of the jet. To adjust the charge density $\rho_c$ within the triangular region of influence of height $a_0(V = V_0)$ and length $b_0(V = V_0)$, the maximum horizontal velocities at $x = 100\,\text{mm}$ were examined and the model coefficients were tuned until the simulations showed the same magnitude for all measured voltages. All following simulations were conducted with these coefficients. The correlation between the operating voltage and the maximum velocity is given by $U \sim V\sqrt{a - e^{bV}}$. The correlation of Jayaraman [85] is of the type $U \sim \sqrt{aV^4 - bV^5}$, whereas Corke et al. [87] found what they call the 7/2-power-law, which is $U \sim V^{\frac{7}{2}}$. As Fig. 4.3 shows, all the correlations fit quite well with the experimental results.

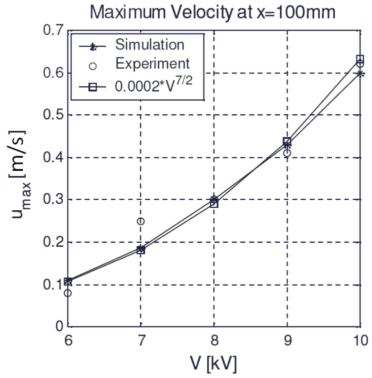

Figure 4.3: Maximum velocity.

### 4.4.2 PIV based model

A recent investigation conducted by Wilke [86] at the Deutsches Zentrum für Luft- und Raumfahrt (DLR) proposes a determination of the induced body forces by the plasma actuator using measured velocity field data. Such an approach, named here the 'PIV based model' is possible under certain assumptions, outlined in more detail in [86] and summarized briefly here.

The very first assumption is that of two-dimensionality, i.e. that the flow has no cross-stream components ($z$ coordinate). Then the Navier-Stokes equations for the $x$ and $y$ components of momentum can be written as

$$\rho\left(\frac{\partial u}{\partial t} + u\frac{\partial u}{\partial x} + v\frac{\partial u}{\partial y}\right) = f_{a,x} - \frac{\partial p}{\partial x} + \mu\left(\frac{\partial^2 u}{\partial x^2} + \frac{\partial^2 u}{\partial y^2}\right) \tag{4.19}$$

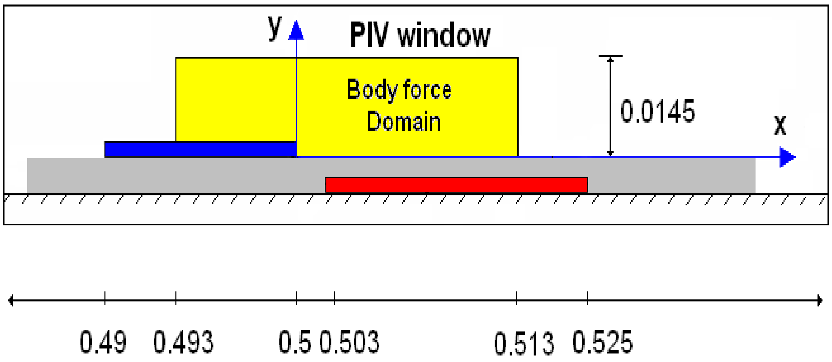

Figure 4.4: PIV-based model scheme.

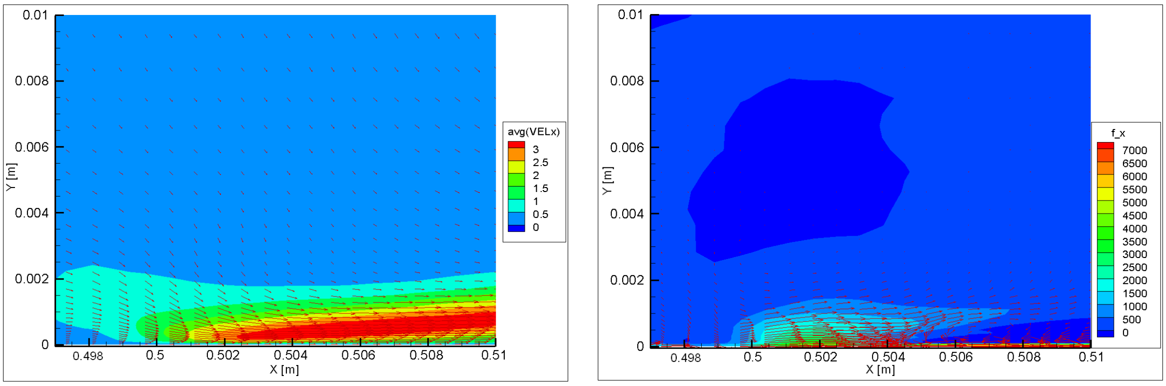

Figure 4.5: Average velocity field obtained by PIV measurements, and body force derived using Eqs. (4.23)-(4.24).

$$\rho\left(\frac{\partial v}{\partial t}+u\frac{\partial v}{\partial x}+v\frac{\partial v}{\partial y}\right)=f_{a,y}-\frac{\partial p}{\partial y}+\mu\left(\frac{\partial^2 v}{\partial x^2}+\frac{\partial^2 v}{\partial y^2}\right), \tag{4.20}$$

where $\vec{f}(t,x,y)$ is the unknown, time-dependent body force induced by the plasma actuator. A further assumption is that the density is constant, which implies that the temperature and pressure fluctuations in the vicinity of the plasma are below limits which would result in density fluctuations exceeding 5%. This is discussed in [86] and is found to be a legitimate assumption, based on experimental findings of various authors. Additionally, the kinematic viscosity ($\nu$) is considered constant, which can also be shown to be a reasonable assumption, assuming a maximum temperature fluctuation and refering to Sutherland's formula for the temperature dependence of viscosity.

Having measured time-dependent velocity fields in the immediate vicinity of the actuator, as shown in Fig. 4.4, the time derivatives and spatial derivatives in Eqns. 4.19 and 4.20 can be evaluated such that body force, together with the pressure gradient can be deduced for each time instant, i.e.

$$f_{a,x} = f_x+\frac{\partial p}{\partial x} \tag{4.21}$$

$$f_{a,y} = f_y+\frac{\partial p}{\partial y}. \tag{4.22}$$

The sum of these two terms (for each component) can then be averaged over many individual velocity field realizations. In Fig. 4.5a an average measured velocity field is shown and in Fig. 4.5b an average of the $f_{a,x}$ and $f_{a,y}$ terms is shown (color gives magnitude). The question arises how significant the pressure gradient term is compared to the induced body forces? This cannot be determined directly from the measurements, since no pressure measurements are available from the flow field. Nevertheless, the pressure gradient terms were shown in [86]to be negligible by retroactively computing the flow field, using as an estimate for the body forces the relations:

$$f_x = \rho\left(u\frac{\partial u}{\partial x} + v\frac{\partial u}{\partial y}\right) - \mu\left(\frac{\partial^2 u}{\partial x^2} + \frac{\partial^2 u}{\partial y^2}\right) \tag{4.23}$$

$$f_y = \rho\left(u\frac{\partial v}{\partial x} + v\frac{\partial v}{\partial y}\right) - \mu\left(\frac{\partial^2 v}{\partial x^2} + \frac{\partial^2 v}{\partial y^2}\right), \tag{4.24}$$

i.e. ignoring the pressure gradient terms. These numerical simulations yielded very good agreement with the measured mean velocity field; hence the pressure gradient terms were deemed to be insignificant.

Note that such an estimation of the body forces requires a time-resolved flow field measurement. In principle the body force is also obtained time resolved, but in the present work only the averaged field has been used for subsequent simulations. Using the time-resolved field is actually not feasible at the present time, it would require a time resolution in the simulations of the order of the alternating current to the actuators, typically 5-10 kHz, rather than a scale resolution of the order of the pulsed operation of the actuators, or in continuous mode, of typical boundary-layer time scales.

Note further, that for every new actuator geometry another velocity field investigation must be performed, which is tedious and reduces completely the universality of the model from one actuator to the next.

Analyzing the phenomenological plasma actuator models described in the foregoing sections, each model has advantages and disadvantages depending on the purpose for which it is to be used. For example, the calibration based model presents advantages when the type of electrode material is being tested or the Reynolds number of the flow changes considerably. However, the computational cost necessary to incorporate this model into the simulations is high compared with the PIV based model. The PIV based model yields good result, once the calibration data has been directly obtained in the flow. However any alteration in the flow, type of electrode material, geometry, etc. requires a new velocity field measurement, increasing the overall cost of implementing this calibration. This model has low computational cost, once the equations are reduced because the body force is read directly into the grid.

# 5 Results using Continuously Operated Actuators

## 5.1 Boundary-layer stabilization

The experimental work on transition delay by means of plasma actuators is accompanied by numerical investigations to provide more insight into the mechanism of cancelation and attenuation of TS-waves in a laminar boundary layer. In the current section two tests are presented to evaluate this mechanism. The first test presents the comparisons of the calibration based model implemented into an LES computation with the experimental and DNS results using two control plasma actuators. The second test compares the calibration based actuator model with the PIV based model using only one control actuator. It can be shown that the simulation of the plasma actuator as a stationary body force is sufficient to capture the observed stabilization of a laminar boundary layer, and the delayed transition is predicted very precisely using both models.

### 5.1.1 Introduction

Boundary-layer control using plasma actuators is an innovative technique to directly influence the growth of TS-waves in laminar flows. Two different methods for delaying the transition have been developed, each employing a different operational mode of the actuators. The first method uses continuously working actuators and locally damps the disturbances, leading to a stabilization of a laminar boundary layer [77]. The second approach uses pulsed actuator operation and is a direct cancelation of TS-waves [41]. Both methods have been successfully demonstrated in experiments by Grundmann and Tropea [26], [41], [88] at the Center of Smart Interfaces (CSI) at the Technische Universität Darmstadt. The first method will be examined in the present chapter and it will be shown how these methods can be reliably simulated using LES.

### 5.1.2 Computational domain

The three-dimensional computational domain contains a spanwise slice of 100mm width across the wind-tunnel test section in which the experimental results were obtained, (Fig. (5.1)). A flat plate is placed in the test section of the wind tunnel and an insert is placed on the upper wall of the test section. The insert is designed to create a constant positive pressure gradient and promote the transition process. A plasma actuator 400mm downstream of the leading edge is operated in pulsed mode to induce TS-waves into the boundary layer. This actuator is denoted as a 'excitor'. It establishes a controlled transition, which is necessary for the experiments as well as for the numerical simulations. Its position is in the smallest cross section of the setup where the pressure gradient (25pa/m) begins.

### 5.1.3 Computational grid

Figure (5.2) shows the entire computational domain which is divided into 30 structured blocks, using a cell-centered scheme and a total of 3 million cells. The near-wall resolution is chosen to realize a $y^+$ of 1 to 1.5 on the plate. Refinements have been carried out in the vicinity of the actuators to reduce the aspect ratio of the cells.

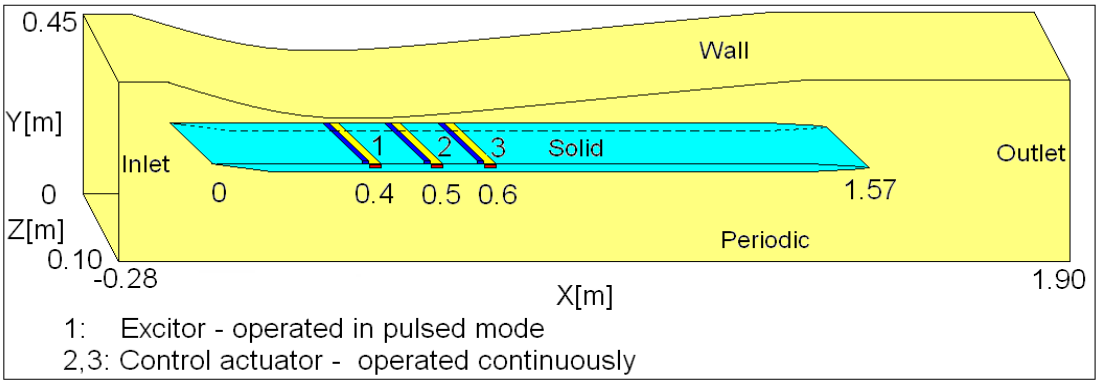

Figure 5.1: Overview of flow domain and actuator positions.

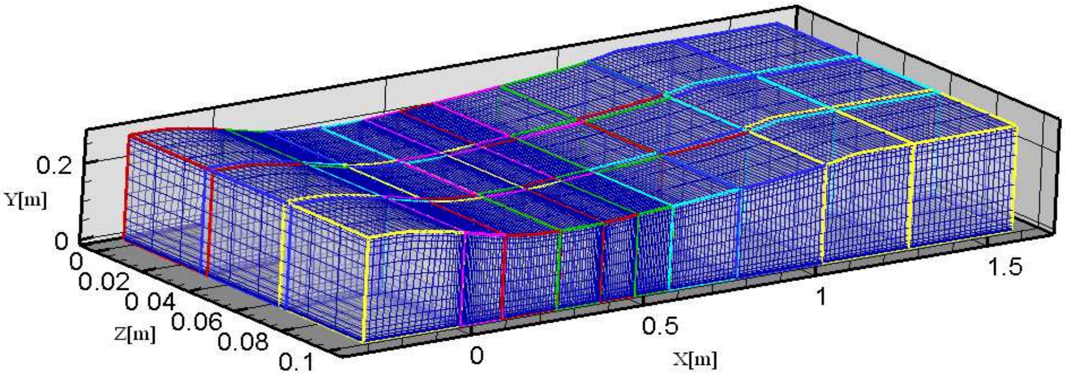

Figure 5.2: Computational grid.

In the following the results of the simulations for two different situations are presented. One situation is the base flow with only the excitating actuator working and no attempt at flow control. The second is the case with the two downstream control actuators also working. Two test cases are presented for each of these two situations. In the first test case two control actuators will be used to influence the flow field and these simulation results will be compared with experimental and two-dimensional DNS results. In the second test case only one control actuator is working and the comparison between two different calibration models of plasma actuators are discussed. Both control actuators are operated continuously and using the same frequency $f = 6$kHz and a voltage of v= 10kV. In the following subsections results are presented concerning these cases.

### 5.1.4 Direct Numerical Simulations

For the Direct Numerical Simulation (DNS), the well established and highly accurate spectral element solver PRISM [89] has been used. The incompressible Navier-Stokes equations are solved by a three-step, semi-implicit splitting scheme, treating only the nonlinear term explicitly. A stiffly-stable time integration scheme of second order accuracy has been used.

In contrast to the LES, only a two-dimensional, rectangular domain $70\,\text{mm} \leq x \leq 1000\,\text{mm}$ has been modeled. For stability and efficiency reasons, the laminar inflow velocity profile and the far-field boundary condition at $y = 150\,\text{mm}$ (30 times the boundary layer thickness $\delta_{99}$) have been extracted from the time-averaged LES results.

The mesh consists of $141 \times 16$ spectral elements of polynomial degree $N = 7$, where about 50 nodes (6 elements) are located within the boundary layer, which is in agreement with previous transition control studies by the present [24] and other authors [90].

The same forcing model, consisting of an excitation actuator and two control actuators as described above, is incorporated into the DNS by an additional source term.

The DNS results presented in this thesis was conducted in the Institute for Aerospace Engineering at Technische Universitaet Dresden by Albrecht et al. [25], being performed non-dimensionally. Given the kinematic viscosity of air $\nu = 1.5 \cdot 10^{-5}\,\mathrm{s}^2/\mathrm{m}$, the relevant velocity at the inflow $x = 70\,\mathrm{mm}$ of $U_{in} = 8.9\,\mathrm{m/s}$ and the inflow displacement thickness $\delta_1 = 1.08\,\mathrm{mm}$, the inflow Reynolds number is 641.

## 5.2 Control of transition to turbulence - test case 1

### 5.2.1 Boundary-layer profiles

Figure (5.3) shows experimental and numerical results for the mean (left column) and fluctuating (RMS, right column) streamwise velocities of both cases, at different downstream locations.

Upstream of the excitation actuator, at $x = 350\,\mathrm{mm}$, the boundary layer is laminar. Yet, the wind tunnel data shows some minor fluctuations, due to weather influences on the wind tunnel at low speeds (the tunnel draws air directly from outside the laboratory). These disturbances reach 3% in some cases. Downstream of the excitation actuator ($x = 450\,\mathrm{mm}$), the calculated streamwise velocity fluctuations nicely match the experimental ones. Due to continuity and the charge of tunnel cross-sectional area, the controlled flow is slightly accelerated already 50 mm upstream of the first plasma actuator.

The next position at $x = 510\,\mathrm{mm}$ is just downstream of the first actuator. LES and DNS velocity profiles almost coincide. Numerical and experimental data, is in very good agreement, clearly demonstrating the increased near-wall velocity when this actuator is operated. The velocity fluctuations of both cases exhibit a typical TS wave-like shape. Yet, at this stage, their amplitudes do not differ considerably.

Downstream of the second actuator ($x = 620\,\mathrm{mm}$), DNS and LES data for the base flow start to differ. Apparently, 3-D effects of secondary instability are already present, where 2-D DNS must fail. For the "control-on" case, numerical data show a slightly accelerated flow of the outer boundary layer; however, this distinction is not found in the measurements. On the contrary, fluctuations reduce by approximately 50% as compared to the uncontrolled case, which is supported by all three data sources.

Typical turbulent-boundary layer profiles are found for the base flow at $x = 750\,\mathrm{mm}$, where LES and experimental data are in good agreement for both mean and fluctuating velocities. The controlled flow is still laminar here, but shows a strong inflection point profile due to the adverse pressure gradient. The velocity fluctuations are five times smaller when the plasma actuators are operated.

At the final position shown ($x = 1050\,\mathrm{mm}$), the flow is fully turbulent in both cases. Again, LES and experimental data are in excellent agreement.

### 5.2.2 Shape factor and wall shear stress

Deeper insight into the capability of the numerical method to capture the transition delay can be obtained by evaluating the development of the shape factor in experiment and simulation. The shape factor is defined by the ratio of the displacement thickness $\delta_1$ and

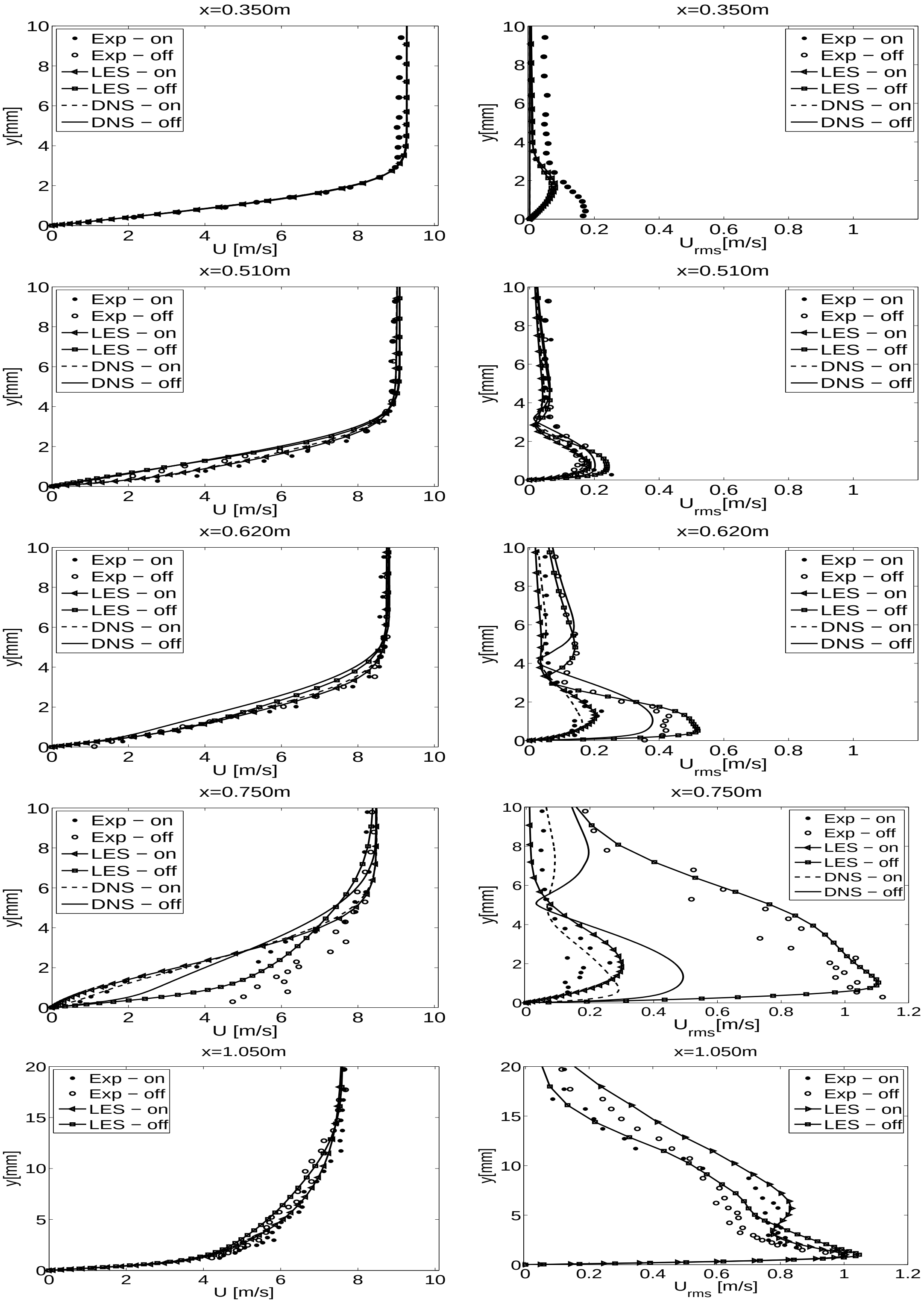

Figure 5.3: Mean and fluctuating streamwise velocity component obtained from LES, DNS, and experiments at different downstream locations.

the momentum thickness $\delta_2$ of the boundary layer:

$$H_{12} = \frac{\delta_1}{\delta_2} \tag{5.1}$$

where the displacement thickness and the momentum thickness are given by

$$\begin{aligned}\delta_1 &= \int_0^\infty \left(1-\frac{U}{U_\infty}\right) dy \\ \delta_2 &= \int_0^\infty \frac{U}{U_\infty}\left(1-\frac{U}{U_\infty}\right) dy.\end{aligned}$$

A laminar boundary layer at zero pressure gradient has a shape factor of 2.6 (Blasius), whereas a turbulent boundary layer exhibits shape factor of approximately 1.4.

Figure(5.4) shows the shape factors of the numerical and experimental results at all positions that were measured in the experiment. The dotted lines mark the case without control. The shape factor rises quickly due to the adverse pressure gradient and the boundary layer becomes highly unstable.

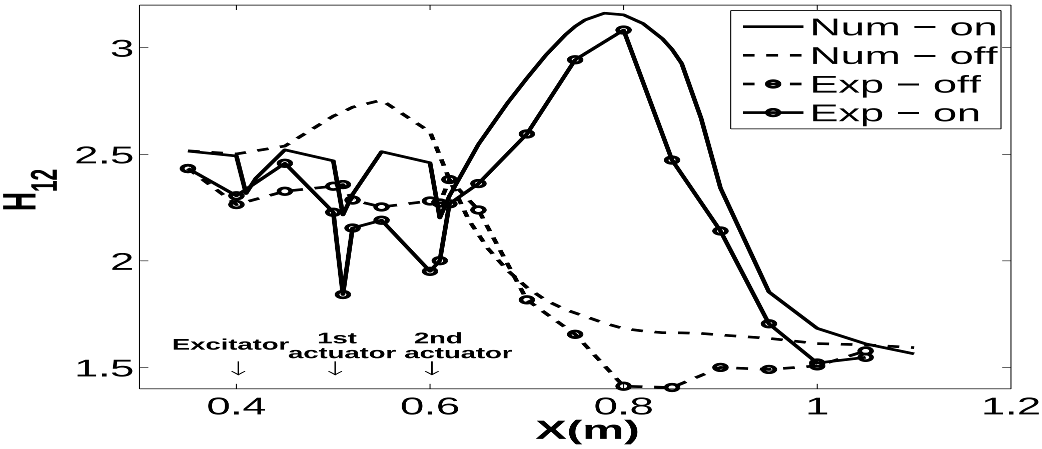

Figure 5.4: Comparisons and development of the shape factor in experiment and simulation.

At about $x = 600$mm the shape factor decreases rapidly where the transition starts and its value ends at 1.6, which corresponds closely to a turbulent profile. With the control actuators working the shape factor drops at the position of the actuators due to their acceleration and deformation of the profiles for a short distance. This is the position where the boundary layer is accelerated and where the waves are attenuated. Due to the longer extent of the laminar boundary layer the positive pressure gradient causes the shape factor to increase to relatively high values of approximately 3 in the experiment as well as in the numerical results. The transition occurs approximately 250mm further downstream, compared to the case without actuation. The mechanism which leads to the attenuation of the waves has obviously been captured correctly in the simulations, since the velocity profiles, the $u_{rms}$-profiles, the shape-factor diagrams and the distance by which the transition is delayed agree very well with the experimental results.

The wall shear stresses in Fig. (5.5) are not available from the experiment but only from the numerical simulations. They yield valuable insight into the wall friction balance. All actuators cause thin peaks in this diagram. The control actuators accelerate the boundary-layer profiles resulting in an increased wall friction directly downstream of the actuators. The altered velocity profiles decay rapidly after a short length downstream of both control actuators. The delay of transition can also be clearly seen in this diagram. The friction-force balance of the LES reveals a large reduction of the friction force on the plate. An overall reduction of 20% can be achieved.

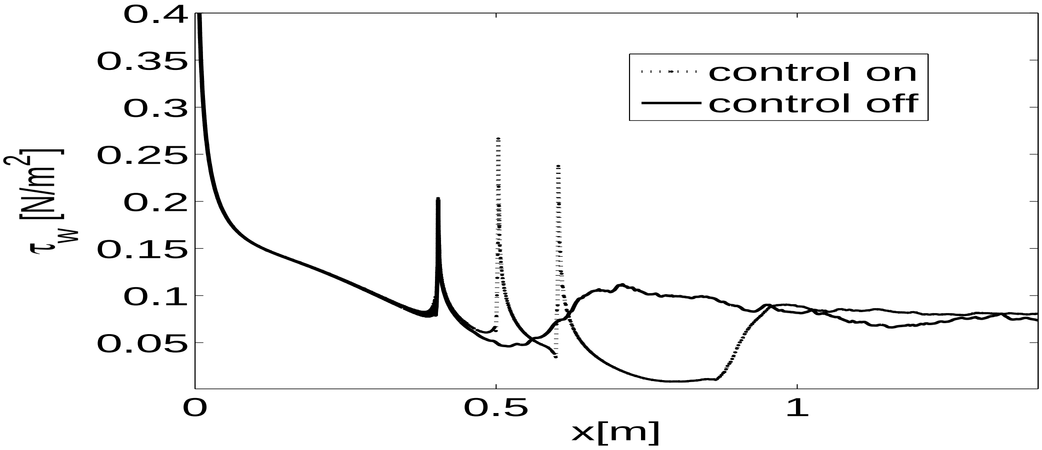

Figure 5.5: Wall shear stress of the numerical simulations.

### 5.2.3 Normalized Reynolds shear stresses

The profiles of the velocity fluctuations of the transitional boundary layer are now examined more closely. In Fig. (5.6), the root mean square of all three velocity component fluctuations, turbulent kinetic energy and the components of the Reynolds shear stress normalized by the friction velocity are plotted at 6 downstream positions. This diagram shows that the energy of turbulence production due to the shear forces is initially supplied to the horizontal component.Through the continuity equation, it is then transferred to the other components. For this reason, $v_{rms}$ and $w_{rms}$ are smaller than $u_{rms}$. At the point $x = 450$mm the fluctuations are basically in the streamwise component and the amplitudes of this component are almost the same for the cases with and without control. At $x = 550$m, the first control actuator apparently damps the fluctuating velocities of eddy disturbances. This damping effectively increases the dissipation of kinetic energy in the eddies, which reduces the fluctuation amplitudes in the flow, leading to a delayed transition. The delayed transition reduces the overall drag of the plate significantly, as previously shown in Fig. (5.5). In the case without control actuators working, the fluctuation amplitudes increase considerably in wall normal and spanwise component. At $x = 650$mm the turbulence intensity profiles of all velocity components are again smaller in the case with control actuators working Fig. (5.6). The lower diagram in Fig. (5.6) shows two downstream positions where the transition is complete in both cases.

### 5.2.4 Tollmien-Schlichting wave cancellation

Based on LES data, Fig. (5.7) shows a streamline originating from a point $x = 0$, $y = 1\,\text{mm}$. In the upper part, the amplitude of the forced fluctuations grows at constant rate, reaching high levels in the turbulent region.

With control actuators working, a significant reduction of the fluctuation amplitude is obvious in the lower part of the figure. Overall, the oscillations are damped down to values of $20 - 30\%$ as compared to uncontrolled boundary layer. Oscillations of a higher frequency than artificially excited arise further downstream due to the highly unstable velocity profiles caused by the adverse pressure gradient.

A quantitative measure of the primary instability can be gained from the local TS-wave amplitude $A$, which is calculated by finding the maximum root mean square value over the

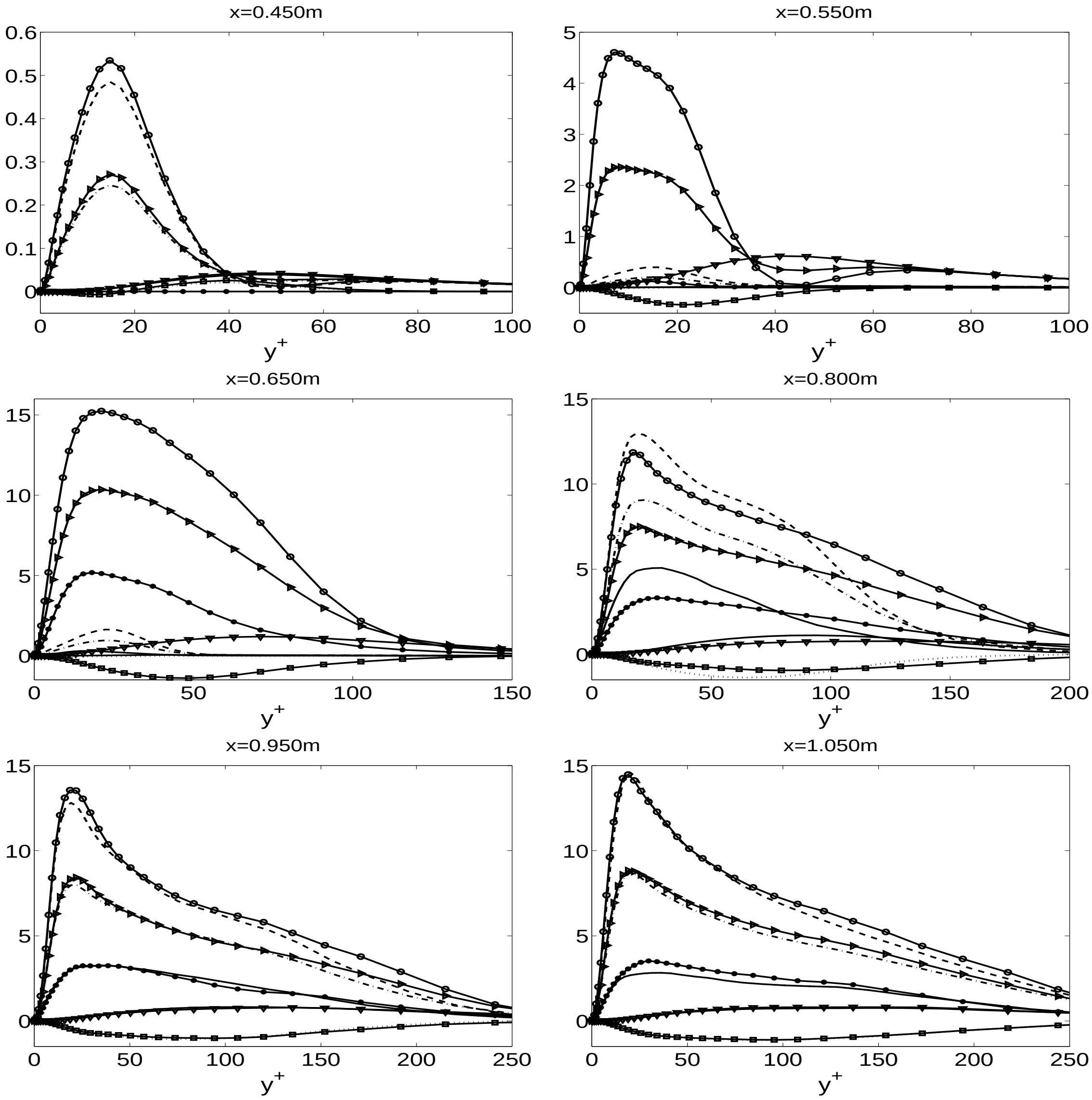

Figure 5.6: Normalized Reynolds shear layer stresses. Control off (— ○ — $u_{rms}/u_\tau$; −∇− $v_{rms}/u_\tau$; −◇− $w_{rms}/u_\tau$; −●− $uv/u_{\tau^2}$;−▷− $ke/u_{\tau^2}$;). Control on (−−− $u_{rms}/u_\tau$; − $v_{rms}/u_\tau$; −·− $w_{rms}/u_\tau$; ··· $uv/u_{\tau^2}$; and ·−· $ke/u_{\tau^2}$;)

wall-normal direction at a given $(x,z)$:

$$A(x,z) \equiv \max_{y=0}^{\infty} u_{rms}(x,y,z) \tag{5.2}$$

This evolution is plotted in Fig. (5.8). No attempt has been made to filter or smooth the experimental data.

Downstream of the wave excitation at $x = 400$ mm, the amplitude calculated by DNS grows at a constant rate until it reaches nonlinear saturation. This corresponds to the experimentally observed onset of turbulence at $x = 650$ mm, which is also nicely captured by the LES data. Beyond that point, the 3D fluctuations are of course much higher than the 2D ones; hence the 2D DNS simulations are no larger considered valid. Looking at the controlled flow, it is interesting to note that the wave amplitude continuously decays for approximately 80 mm downstream of the first actuator, while it is kept more or less constant by the second actuator over the same streamwise length. Probably, these different

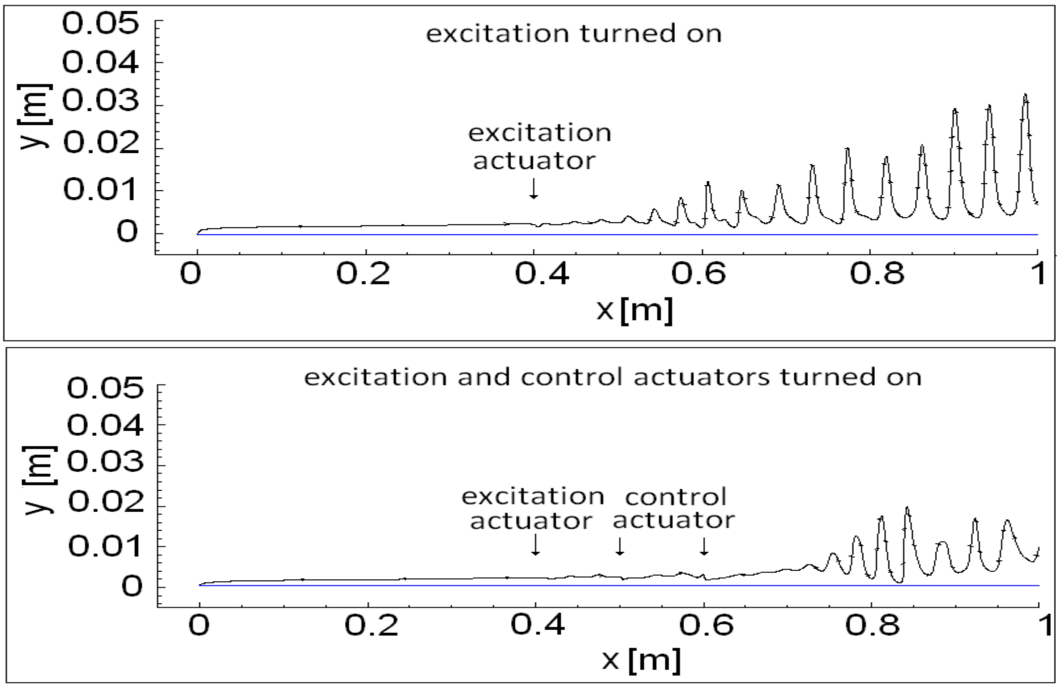

Figure 5.7: Streamline originating from $x = 0, y = 1\,\text{mm}$ with and without control actuator operation.

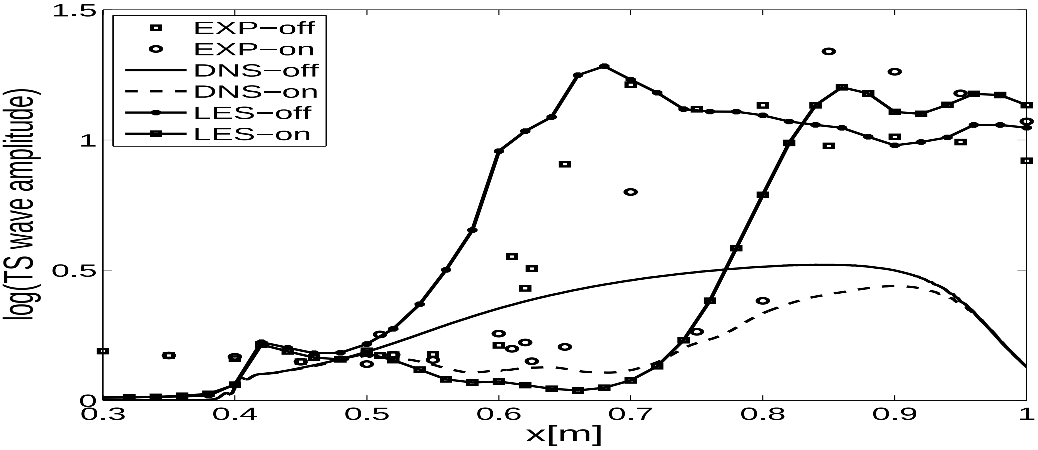

Figure 5.8: TS-wave amplitude, obtained from LES, DNS, and experiments for control actuators off ad on.

damping characteristics can be attributed to the strong non-self-similarity of the velocity profiles in the adverse pressure gradient region. The strong damping of the fluctuations for $x > 900\,\text{mm}$ is caused by an artificial buffer region in the DNS.

Additionally, the influence of the plasma actuators on the transition process is shown in Fig. (5.9) using a top view of the flow structures, visualized by isosurfaces of the Q-criterium ($Q = \frac{1}{2}(S_{ik}S_{kj} - \Omega_{ik}\Omega_{kj})$, where $S_{ij} = 0.5(\partial u_i/\partial x_j + \partial u_j/\partial x_i)$ denotes the strain-rate tensor and $\Omega_{ij} = 0.5(\partial u_i/\partial x_j - \partial u_j/\partial x_i)$ the vorticity tensor [91]). In the case without a control actuator, the amplification of initially 2D instability waves starts downstream of the excitation actuator at $x = 400\,\text{mm}$. Then, through the development of 3D structures at $x \approx 600\text{mm}$, streamwise vortical structures are formed from which strong shear layers arise, followed by a rapid breakdown to turbulence. When the two control actuators are working, a notable reduction of the TS-wave amplitude is evident in the

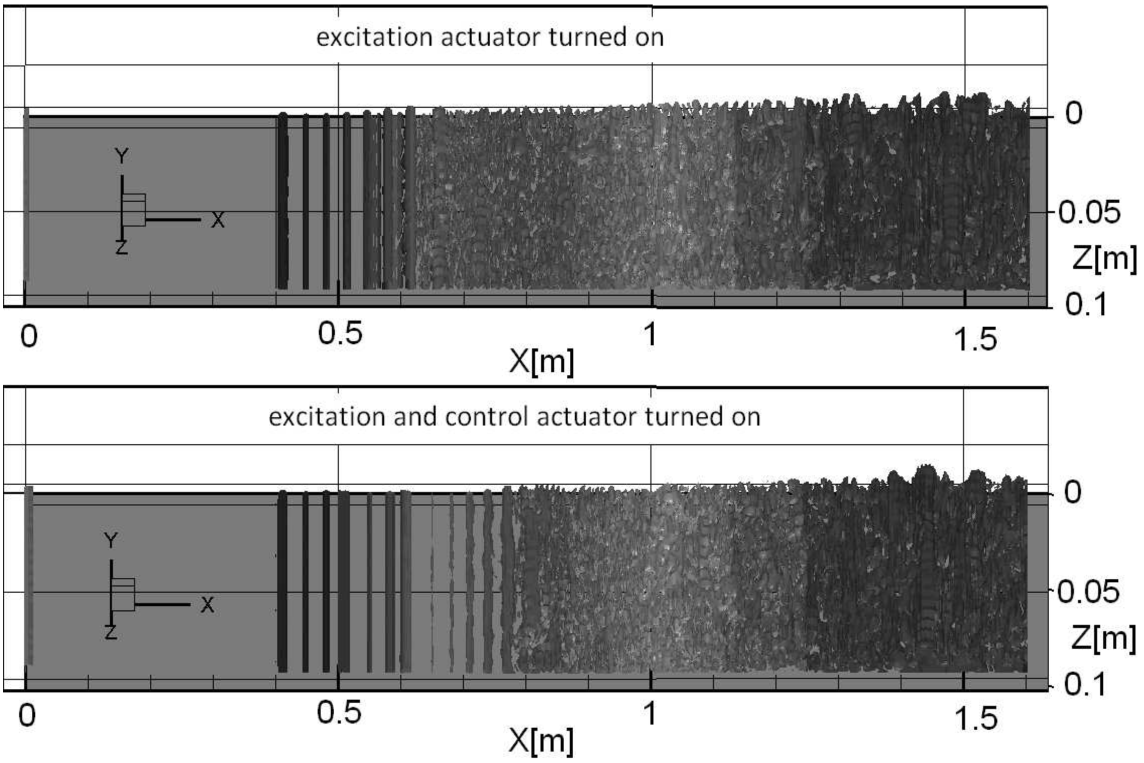

Figure 5.9: Top view of the three-dimensional flow structures for controlled and uncontrolled flow using plasma actuators.

lower part of Fig. (5.9). The increasing fluctuations of the streamwise velocity component caused by the plasma actuator increases the dissipation of kinetic energy within an eddy. This increased dissipation reduces the fluctuation amplitudes in the flow, which leads to a delayed transition. A fully turbulent boundary layer occurs approximately 200 mm further downstream as compared to the uncontrolled case.

### 5.2.5 Frequency spectrum

To reveal more information about the frequency content of both base and controlled flow, spectra of the streamwise velocity component are shown in Fig. (5.10). They were obtained from the LES data at three streamwise locations, one upstream and two downstream of the first actuator.

The spectral peaks at the excitation frequency and its harmonics are distinct at all streamwise locations shown. Special care was taken [92] to ensure that these peaks are actually due to the unsteady flow field generated by the excitation actuator at $x = 400\,\mathrm{mm}$. Interestingly, while these peaks still coincide for both cases at the first x-position (20 mm upstream of the first actuator), the background noise is already considerably lower for the controlled case as compared to the base flow.

At $x = 590\,\mathrm{mm}$, the peak of the fundamental frequency is reduced by the first actuator, corresponding to a decreased TS-wave amplitude. The background noise further decays, especially for higher frequencies. In subsequent diagrams, also the higher harmonics decrease significantly.

For the controlled flow, the last location ($x = 750\,\mathrm{mm}$) corresponds to the late stage of transition. Here, the streamwise velocity fluctuations are even higher than those of the fully turbulent base flow, which is consistent with the diagram $x = 800\,\mathrm{mm}$ in Fig. (5.6).

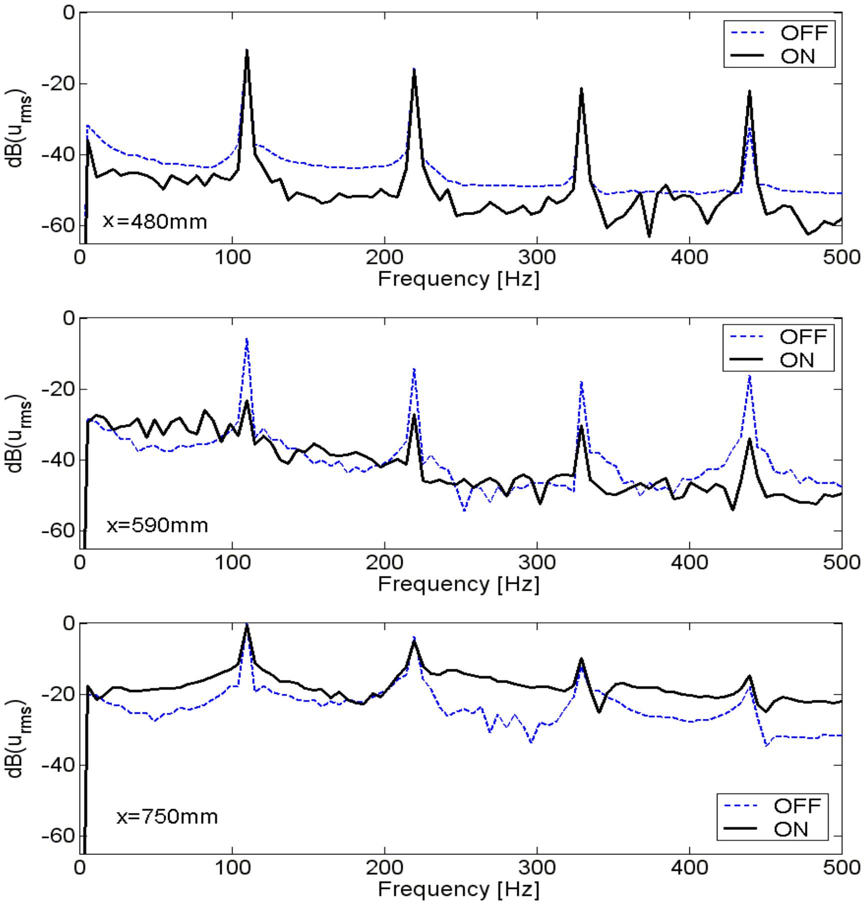

Figure 5.10: Velocity spectra at three streamwise locations with and without control actuator. The data was collected for $y = 0.5\,\delta_{99}$.

## 5.3 Control of transition to turbulence - test case 2

In this test case only one control actuator is used. However both calibration based and the PIV based model are involved and comparisons between the models are presented.

The computational domain used in the present case is presented in the Fig. (5.11).

The excitation actuator that provokes TS-waves in the boundary layer on the flat-plate is operated using a sinusoidal modulation. The control actuator is operating in continuous mode, using the frequency $f = 6$kHz and a voltage $v = 10$kV.

In the following subsections the results concerning this case are presented.

### 5.3.1 Boundary-layer profiles

The comparisons of numerical results for the mean and fluctuating velocities of cases with and without control actuator using calibration and PIV-based methods are shown in Fig. (5.12). The upper figure shows the boundary layer at the position $x = 480$mm. At this position the boundary layer is laminar and only the effect of the excitation actuator is present in both cases. The fluctuations shown in the $u_{rms}$-profile without control actuators clearly shows the typical profile of strong TS-waves. The middle diagram shows the profile and the fluctuations 50mm downstream of the control actuator. The velocity profile presents some differences between the two models because the effect of the PIV based model is concentrated closer to the wall. The largest difference is present in the velocity

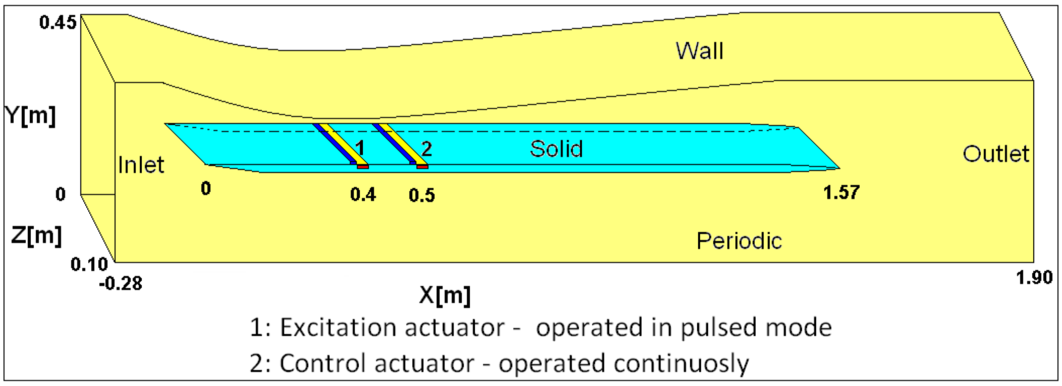

Figure 5.11: Overview of flow domain and actuator positions used in the second test case.

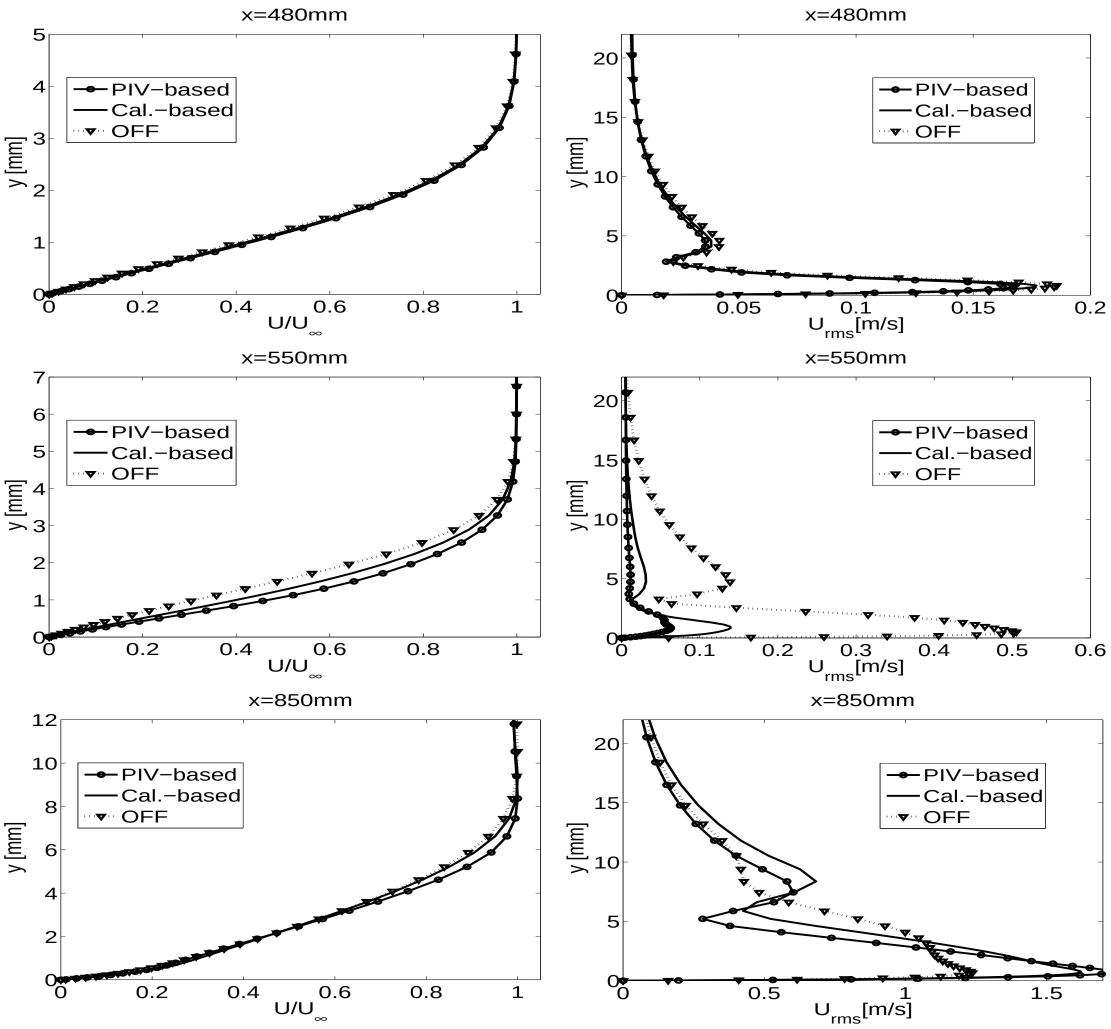

Figure 5.12: Boundary-layer velocity profile and fluctuations compared for the two control actuator models.

fluctuations. A reduction of 90% in the $u_{rms}$ was observed using the PIV based method. The calibration based method reduced 80% of the streamwise velocity fluctuations. In the lower diagram, the velocity profile represents a tendency to the turbulent form and the higher fluctuations indicates that the transition is occurring at this position. The difference between the two models are minor.

### 5.3.2 Shape factor and wall shear stress

Figure (5.13) shows the shape factors of the both numerical methods implemented in this work at all positions that were presented in the Fig. (5.5). The square symbols mark the case without control. The shape factor rises quickly due to the adverse pressure gradient and the boundary layer becomes highly unstable.

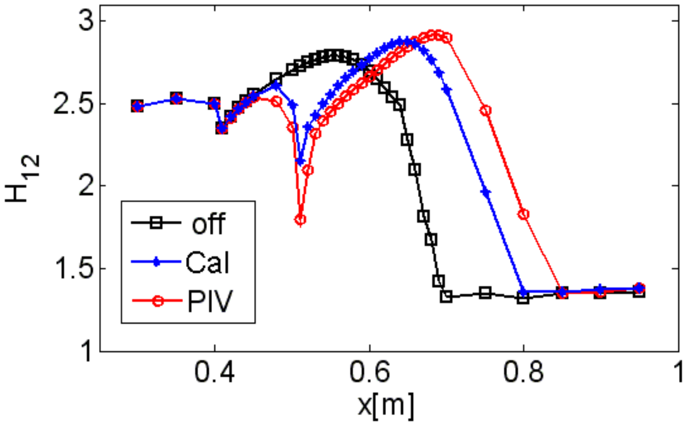

Figure 5.13: Comparisons and development of the shape factor of both phenomenological models.

At about $x = 600$mm the shape factor decreases rapidly where the transition starts and its value ends at 1.4, which corresponds closely to a turbulent profile. With the control actuators working, the shape factor drops at the position of the actuators due to their acceleration and deformation of the profiles for a short distance. This is the position where the boundary layer is accelerated and where the waves are attenuated. Due to the longer extent of the laminar boundary layer the positive pressure gradient causes the shape factor to increase to relatively high values of approximately 3. The strong acceleration close to the wall realized by the control actuator increase quickly the instability of the boundary layer, maintaining such instabilities for more time; hence delaying transition. The transition occurs approximately 100mm further downstream compared to the calibration based.

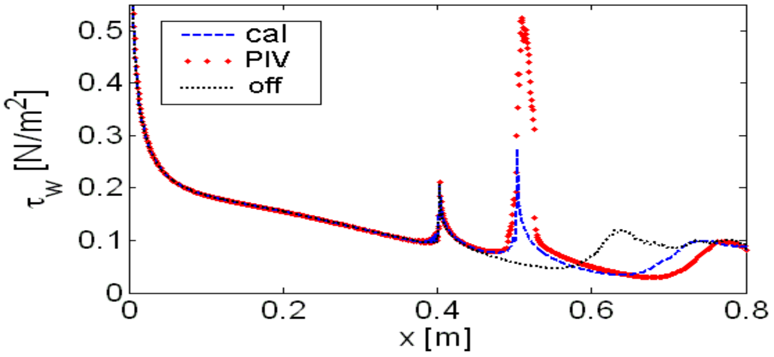

Figure 5.14: Wall shear stress comparisons for both phenomenological models.

The wall shear stresses in Fig. (5.14) yield valuable insight into the wall friction balance. The control actuators accelerate the boundary-layer profiles resulting in an increased wall friction directly downstream of the actuators. The wall skin friction using the PIV based model at $x = 500$mm exhibit higher values in comparison with the calibration based method, since the PIV-based method creates the wall jet closer to the wall. The altered velocity profiles decay rapidly after a short length downstream of both control actuators. The delay of transition with both methods can be clearly seen in this diagram. The friction force balance of the LES reveals a large reduction of the friction force on the plate. An overall reduction of 22% can be achieved using the PIV based method. The skin friction force was integrated using the complete flat plate, i.e. from leading edge until x=1,57m.

## 5.4 Conclusions

It is desirable to draw now conclusions as to which model of the plasma actuator is most preferable to properly capture the effects on a laminar boundary layer or on a boundary layer in the linear regime of transition. Some attempt to summarize the performance of each of the two models ('Calibration based' and 'PIV based') has been made in Table 5.1. The calibration-based model is an analytic model and, once calibrated, can be used for varying operation parameters of the actuators; thus it displays a certain universality for this type of actuator. The PIV-based model is very specific for given operating conditions and actuator geometries, but is also computational efficient, since the body force is projected directly onto the computational grid. The actual computational results differ only marginally using the two different models, although the PIV-based model exhibits somewhat better agreement with experimental findings.

Table 5.1: Plasma actuator model comparison.

| | Calibration | PIV |
|---|---|---|
| Implementation | analytical | experimental |
| Calibration | numerically | experimentally |
| Streamwise RMS (%) | 80 | 90 |
| Delay transition (mm) | 80 | 100 |
| Drag reduction (%) | 20 | 22 |

# 6 Optimization of Actuator in Pulsed Operation

Recent years have seen many advances in the analysis of flow control and optimization problems, especially for viscous, incompressible flows governed by the Navier-Stokes system of equations. These advances rely on similar advances in the theory of partial differential equations and in the analysis of algorithms for such equations. They have played a significant role in the successful development of computational strategies for solving flow control and optimizations problems.

This field is particularly attractive in the context of the present work because one of the main advantages of having the ability to numerically simulate the complex laminar-turbulent transition under the influence of DBD plasma actuators, is that tedious experimental studies can be replaced by numerical experiments. The attractiveness of such an approach becomes evident when the number of possible parameters to be varied is examined. These include not only the geometric parameters of the actuators themselves, but especially the operating parameters: e.g. high voltage, frequency, duty-cycle (for pulsed mode), signal form, etc. Systematic variations of all these parameters in search of the most appropriate actuators and operational conditions is prohibitive in cost, both experimentally and through numerical simulation. Hence, the need for optimization strategies becomes very clear.

## 6.1 The structure of optimization problems

Optimization problems of flow control usually have four components:

**i)** state variables;

**ii)** control variables or design parameters;

**iii)** an objective, cost, or performance functional; and

**iv)** constraints that the control variables must satisfy.

The state variable could be velocity vector or potential, pressure, density, temperature and/or internal energy. The state variable is the mechanical and thermodynamical variable that describes the flow or a reason why one wants to control the flow. In this work, we will control the TS-waves trying to delay the transition to turbulence.

The control or design variables are one or more of the data specified that determine the state variables, e.g, heat flux, temperature at the wall, inflow mass flow rate, body force in the flow, phase shift of the waves and others. In fact, an optimization procedure often leads to the elimination of certain control variables as being instrumental in achieving the objective function.

The objective functional can take many forms, for instance, how close the velocity field is to a given field, or the amplitude control of the TS-wave with in a specified region, or the magnitude of the drag or lift, etc. In this research, the objective function is the amplitude reduction of TS-wave in a flat-plate boundary layer at low Reynolds number, i.e.

$$\sum_{j=i}^{i+m-1} \frac{(\tilde{Y}(t_{j+1}) - \tilde{Y}(t_j))^2}{t_{j+1} - t_j}, \tag{6.1}$$

where $\tilde{Y}$ is the TS-wave amplitude and $\lambda = |[t_i, t_{i+m}]|$ with time $t_i$.

There are two kind of constraints: the main constraint, that corresponds to the governing flow equations, for example, the Navier-Stokes equations, and the auxiliary constraints such as minimum drag, minimum power requirements, maximum amplitude reduction of TS-waves and others. Mathematically, such an objective is expressed as a cost, or objective, or performance functional.

The constraints determine what type of flow one is interested in and this places direct or indirect limits on candidate optimizers. One must, for example, decide what type of fluid model is adequate, i.e., decide if one is satisfied with assuming that the flow is a potential, an inviscid, a viscous, an incompressible, a compressible, a stationary, a time dependent flow, etc. Mathematically, the type of flow is expressed in terms of a specific set of partial differential equations. One may also impose constraints motivated by practical necessities, e.g., to minimize the drag on an airfoil subject to the lift and/or the volume being greater than a specific value.

The four components are put together in an optimization problem by seeking optimal states and controls that satisfy the constraint and minimize the objective functional.

In this thesis, the optimization problem is to find state and control variables that minimize the objective functional subject to the requirement that the constraints are satisfied. So, an algorithm was developed to find the best parameters to create the body force to maximize the reduction of amplitude of TS-waves in the wall and so reduce the wall shear stresses, delaying transition to turbulence.

## 6.2 Optimization algorithm for optimal control of TS-waves using plasma actuators

In this section, a methodology for active flow control which couples unsteady flow fields and controls is described. Active control methods are used to maintain laminar flow in a region in which the natural instabilities lead to turbulent flow. The simplest form of control which might achieve this objective is the active wave cancellation using plasma actuators. Two optimization methods will be described and compared to a closed-loop control developed in this work. The Nelder-Mead is a simplex method which uses a pattern search comparing function values at the three vertices of a triangle [48]. The NEWUOA method includes the choice of the initial quadratic model to find the least value of a objective function $F(x)$, where this function can be calculated for any vector of variable $x$.

Some results using the closed loop algorithm developed in this work and a comparison with the two different algorithms cited above are presented. This section describes in detail the optimization algorithms used for the automatic parameter adjustment. The constraint equations are the full, two-dimensional Navier-Stokes equations. A two-dimensional characterization of TS-waves in the region which the plasma actuator control is executed, the high computational cost expended to optimize the parameters and the similarity of the results using two and three-dimensional Navier-Stokes equations justify this constraint. The objective function uses measurements of temporal velocity magnitude at y=1.0mm above the wall.

### 6.2.1 Phenomenological closed-loop control

The first approach to optimal parameter selection is a closed-loop control, mimicking the approach successfully demonstrated in experiments using various boundary-layer actuators [31]. The system is schematically represented in Fig. 6.1 and can be realized both experimentally (real-time) and numerically. Simple gradient methods have been implemented in this controller. The algorithm follows the steps outlined below:

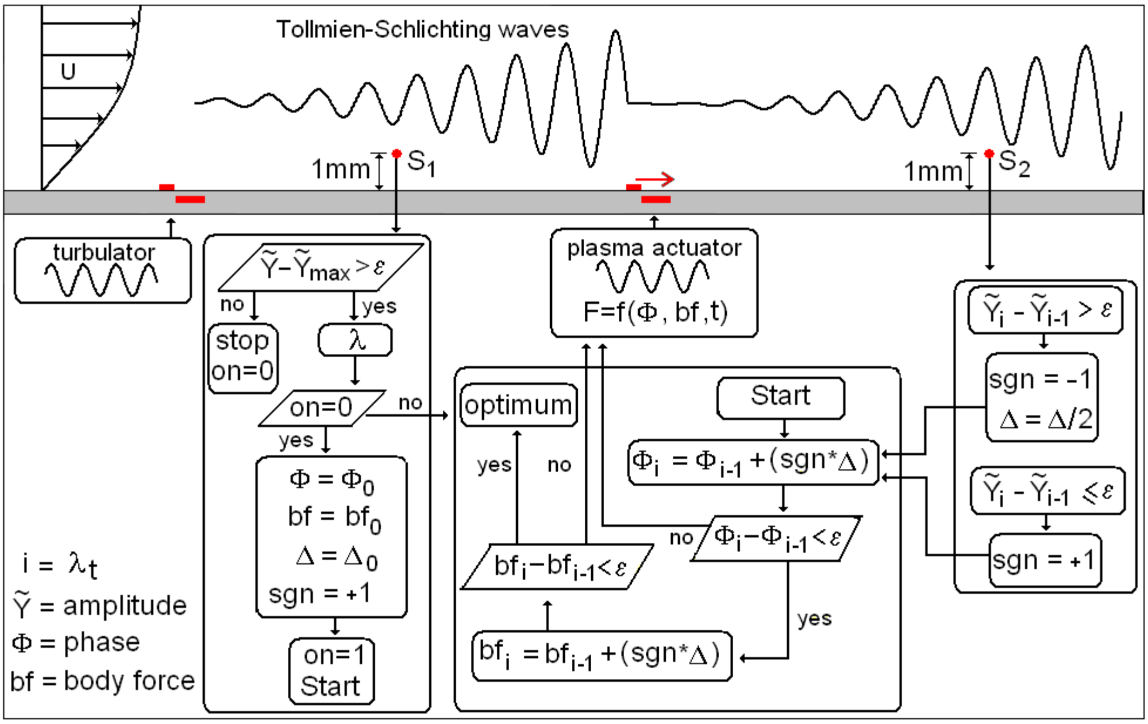

Figure 6.1: Schematic diagramm of closed-loop control.

1. The signal of the first velocity sensor ($S_1$) indicates when the amplitude of TS-wave ($\tilde{Y}_i, i = \lambda$) is larger than the prescribed amplitude ($\tilde{Y}_0$). Then the initial conditions ($\Phi_0, bf_0, \Delta_0$) are read and the closed-loop circuit starts to operate. $\Phi_0$ is the initial phase of the TS-waves, $bf_0$ is the initial body-force applied in the control actuator and $\Delta_0$ corresponds to the initial time step of the parameters.

2. These conditions are used in a sinusoidal function $F^* = f(\Phi, bf, \Delta t)$ that is coupled to the plasma actuator model implemented in the LES solution of the Navier-Stokes momentum equation, beginning the process of active wave cancellation.

3. After a period that corresponds to two wavelengths ($\lambda = \frac{v}{f}$), the signal of the second velocity sensor ($S_2$) is used to analyze the amplitude of the attenuated wave. If the amplitude of the controlled TS-wave ($\tilde{Y}_{i+1}$) is smaller than ($\tilde{Y}_i$), a control parameter signal takes a positive value and the operating parameter changes adding a step increment. Otherwise, if the amplitude ($\tilde{Y}_{i+1}$) increases in time, the step increment of the operating parameter will be reduced ($\Delta\Psi_i = 0.2\Delta\Psi_{i-1}$) and the control parameter takes a negative value and turns to $\Phi = \Phi - (sgn)\alpha^*\Delta\Phi$, where $\alpha^*$ depends of the signal ($sgn$) as follows:
   - positive *sgn*: $\alpha^* = 0.8$;
   - negative *sgn*: $\alpha^* = 0.2$.

4. Return to step 2 again until the controlled parameter remains unchanged in time, i.e. the convergence error $\epsilon \approx 0$.

The procedure is similarly applied to all operating control parameters. Convergence is obtained within only a few iterations.

The sensor position used for these simulations corresponds the same position used in experiments. In the experiments however, the choice of this position was quite restricted because the electrical disturbances from the plasma actuator influencing the hot-wire probe used to monitor velocity fluctuations. The resulting position was 50mm downstream of the excitation actuator. In the simulations the "pseudo"-velocity sensor were positioned 1mm above the surface, yielding good resolution of the TS-wave oscillations.

### 6.2.2 NELDER-MEAD method

The Nelder-Mead method is a simplex method for finding a local minimum of a function of several variables. It's discovery is attributed to J. A. Nelder and R. Mead [48]. For two variables, a simplex is a triangle, and the method is a pattern search that compares function values at the three vertices of a triangle. The worst vertex, where the objective function $f(x,y)$ is largest, is rejected and replaced with a new vertex. A new triangle is formed and the search is continued. The process generates a sequence of triangles (which might have different shapes), for which the function values at the vertices becomes smaller and smaller. The size of the triangles is reduced and the coordinates of the minimum point are found once some truncation condition is reached. The description of the method will follow closely the treatment of Mathews [93]. The algorithm is described using the term simplex (a generalized triangle in $n$ dimensions) and will find the minimum of a function of $n$ variables. The NELMEAD algorithm scheme is represented schematically in Fig. (6.2).

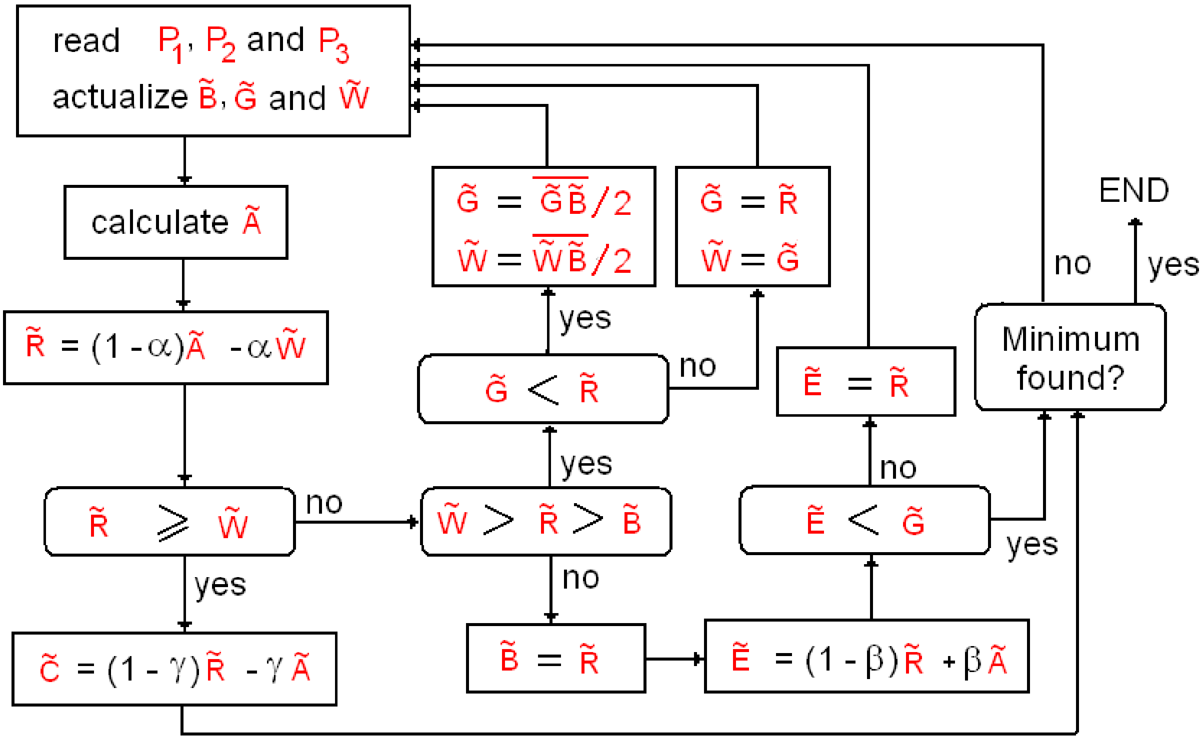

Figure 6.2: Nelmead algorithm scheme.

The simplex method NELMEAD for $n \geq 2$ has four basic operations:

1. Reflect $\tilde{R}$;

2. Expand $\tilde{E}$;
3. Contract $\tilde{C}$;
4. Shrink $\tilde{S}$.

Let $f(x_1, x_2, ..., x_n)$ be the function that is being minimized and $\tilde{A}$, $\tilde{B}$, $\tilde{C}$, $\tilde{W}$, $\tilde{R}$, $\tilde{E}$ and $\tilde{G}$ vertices of a triangle. To start the optimizations process, suppose 3 vertices of a triangle given by $\tilde{B} = (x_1, y_1, z_1, ...)$, $\tilde{G} = (x_2, y_2, z_2, ...)$ and $\tilde{W} = (x_3, y_3, z_3, ...)$, to $\tilde{B} \neq \tilde{G} \neq \tilde{W}$. The function $f(x_1, x_2, ..., x_n)$ is then evaluated at each of the three points, such that $\tilde{W} \geq \tilde{G} \geq \tilde{B}$. Remember that $\tilde{W}$ is the worst point, $\tilde{G}$ is next to the best (good point) and $\tilde{B}$ is the best point. In this particular application the function $f$ represents the amplitude of TS-waves, where the components of this function corresponds the body force and phase shift evaluated in each iteration.

The construction process uses the midpoint of the line segment joining the two best vertexes, in this case $\tilde{B}$ and $\tilde{G}$. It is found by averaging the coordinates

$$\tilde{A} = \frac{\tilde{B} + \tilde{G}}{2}. \tag{6.2}$$

To the first operation, observe that the function decreases as we move along the side of the triangle from $\tilde{W}$ to $\tilde{B}$, and it decreases as we move along the side from $\tilde{W}$ to $\tilde{G}$. Hence it is feasible that $f(x_1, x_2, ..., x_n)$ takes on smaller values at points that lie away from $\tilde{W}$ on the opposite side of the line between $\tilde{B}$ and $\tilde{G}$. Then chosen a test point $\tilde{R}$ that is obtained by reflecting the triangle through the side $\overline{\tilde{B}\tilde{G}}$. To evaluate $\tilde{R}$ take the distance $d$ between the line segment from $\tilde{W}$ to $\tilde{A}$, then using the equation

$$\tilde{R} = \tilde{A} + \tilde{\alpha}(\tilde{A} - \tilde{W}), \tag{6.3}$$

where $\tilde{\alpha} = 1$, the point $\tilde{R}$ is found, as showed on the Fig. (6.3).

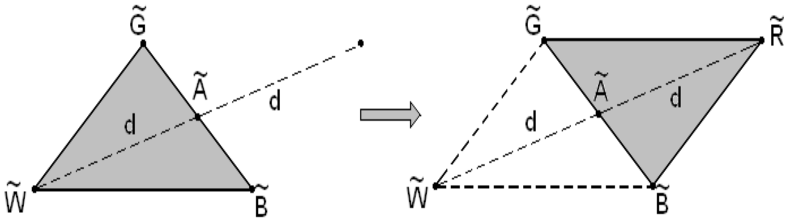

Figure 6.3: Reflection point $\tilde{R}$ for Nelder-Mead method.

The vector formula for expansion $\tilde{E}$ is given by

$$\tilde{E} = \tilde{A} + \tilde{\beta}(\tilde{A} - \tilde{W}), \tag{6.4}$$

where $\tilde{\beta} > \tilde{\alpha}$. If the function value at $\tilde{R}$ is smaller than the function value at $\tilde{W}$, then one moves in the correct direction toward the minimum. Maybe the minimum is just a bit farther than the point $\tilde{R}$. So extend the line segment through $\tilde{A}$ and $\tilde{R}$ to the point $\tilde{E}$. This forms an expanded triangle $\overline{\tilde{B}\tilde{G}\tilde{E}}$. The point is found by moving an additional distance $d$ along the line joining $\tilde{A}$ and $\tilde{R}$, as showed on the Fig. (6.4). If the function value at $\tilde{E}$ is less than the function value at $\tilde{R}$, than it has found a better vertex than $\tilde{R}$.

The contraction form $\tilde{C}$ is found solving the equation

$$\tilde{C} = \tilde{A} + \tilde{\gamma}(\tilde{W} - \tilde{A}), \tag{6.5}$$

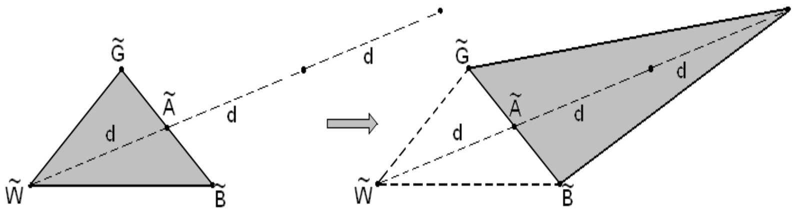

Figure 6.4: Extention $\tilde{E}$ for Nelder-Mead method.

where $\tilde{\gamma} = 1/2$ and must be used when the function at $\tilde{R}$ and $\tilde{W}$ are the same. Perhaps the function is smaller at $\tilde{A}$, but this point cannot replace $\tilde{W}$ otherwise a triangle no longer exists. Considering the two midpoints $\tilde{C_a}$ and $\tilde{C_b}$ of the segments $\overline{\tilde{W}\tilde{A}}$ and $\overline{\tilde{M}\tilde{R}}$. The point with the smaller function value is called $\tilde{C}$ and the new triangle is $\overline{\tilde{B}\tilde{G}\tilde{C}}$, as described in Fig. 6.5.

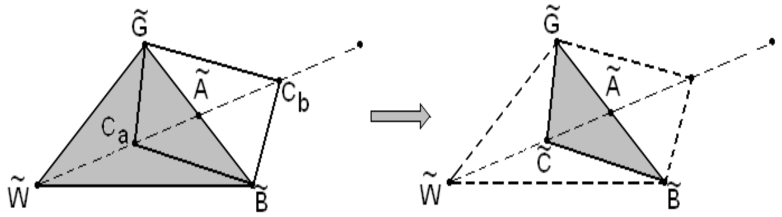

Figure 6.5: The contraction point $\tilde{C}$ for Nelder-Mead method.

Finally, if the value at $\tilde{C}$ is not less than the value at $\tilde{W}$, the points $\tilde{G}$ and $\tilde{W}$ must be shrunk toward $\tilde{B}$. The point $\tilde{G}$ is replaced with $\tilde{A}$, and $\tilde{W}$ is replaced with $\tilde{S}$, which is the midpoint of the line segment joining $\tilde{B}$ with $\tilde{W}$. The next step will be used the triangle $\overline{\tilde{B}\tilde{S}\tilde{M}}$. The scheme is presented in Fig. (6.6).

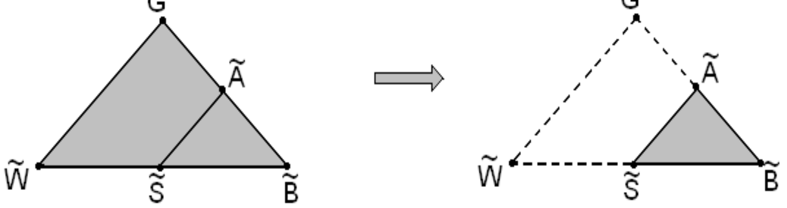

Figure 6.6: Shrinking the triangle toward $\tilde{B}$.

The triangulation process follows till the difference between previous and current verticies approach to zero, i.e., a final point concerns the criterion used to terminate the procedure. Observe that the coefficients $\tilde{\alpha}$, $\tilde{\beta}$ and $\tilde{\gamma}$ give the factor by which the volume of the simplex is changed by the operations of reflection, expansion or contraction respectively and the success of the criterion depends on the simplex not becoming too small in relation to the curvature of the surface until the final minimum is reached.

### 6.2.3 NEWUOA method

A recent derivative-free optimisation algorithm, called NEWUOA (NEW Unconstrained Optimisation Algorithm), conducted by Elsemüller [4] has also been implemented in this work.

Modern optimisation algorithms often use a local model of the objective function $F(x)$. According to Powell [3] the original idea is from Winfield (1973) [94] who created a quadratic model $Q(x)$ of the objective function $F(x)$, $x \in \mathbb{R}$. In such cases the model $Q(x)$ is built to fit $F(x)$, and the optimum of $Q(x)$ is considered to match the one of $F(x)$. With a non-quadratic function, this is not true, so the model $Q(x)$ is updated with the value of $F(x)$ corresponding to the previous optimum of $Q(x)$, and some iteration is performed until a stopping criterion is reached:

$$F(x_{opt}) = min_x F(x). \tag{6.6}$$

The quadratic model $Q(x)$ is created using $m \in [n+2, 0.5(n+1)(n+2)]$ sample points of $F(x)$, where $n$ is the problem dimension. A point $x_0$ is the initial parameter provided by the user. Interpolation points are selected inside a neighborhood of $x_0$. This neighborhood is called the trust-region. The point $x_{opt}$ is the optimal point computed inside the trust-region. The algorithm updates $Q(x)$ by selecting the interpolation point $x_t$ that is the farthest from the point $x_{opt}$. The point $x_t$ is replaced by $x_{opt}$ and $Q(x)$ is updated with the value of $F(x_{opt})$. The trust-region ratio decreases during the optimisation process when the optimum of $Q(x)$ stops decreasing the value of $F(x)$. The iterations stop either when the trust-region ratio reaches a user-defined final ratio or when Q(x) is considered close enough to $F(x)$. NEWUOA usually show good behaviour for optimisation when the number of samples is selected as $m = 2n + 1$, which is the value used for the following experiments.

Summarizing, the NEWUOA proposed by Powell [3], is an optimisation algorithm briefly outline as follows (see Fig. (6.7)):

1. Create a quadratic model $Q(x)$ of the function $F(x)$ to optimize within a trust-region; $Q(x)$ interpolates $F(x)$ at some chosen sample points;
2. Compute the minimum of $Q(x)$ inside a trust-region;
3. Improve the model using the latest optimum;
4. stop if the latest trust-region is lower than the user-defined and value;
5. stop if the distance between $Q(x)$ and $F(x)$ is small enough (perfect match of the model and the objective function $F(x)$);
6. decrease the trust-region ratio, if the values computed for $F(x)$ stops decreasing.

### The initial quadratic model

Let $x^{(k)}$, $k = 1, 2, 3, ...$ be the best vector of variables at the beginning of the $k-th$ iteration, which means that $F(x^{(k)})$ is the least calculated value of $F$ so far. Let the quadratic model at the beginning of $k$th iteration be the function

$$Q^{(1)}(x_0 + d) = Q(x_0) + d^T \nabla Q(x_0) + \frac{1}{2} d^T \nabla^2 Q d, \ d \in \mathbb{R}^n \tag{6.7}$$

$x_0$ being the initial vector of the variables that is provided by the user. When the number of interpolation condition

$$Q(x_i) = F(x_i), \ i = 1, 2, ..., m, \tag{6.8}$$

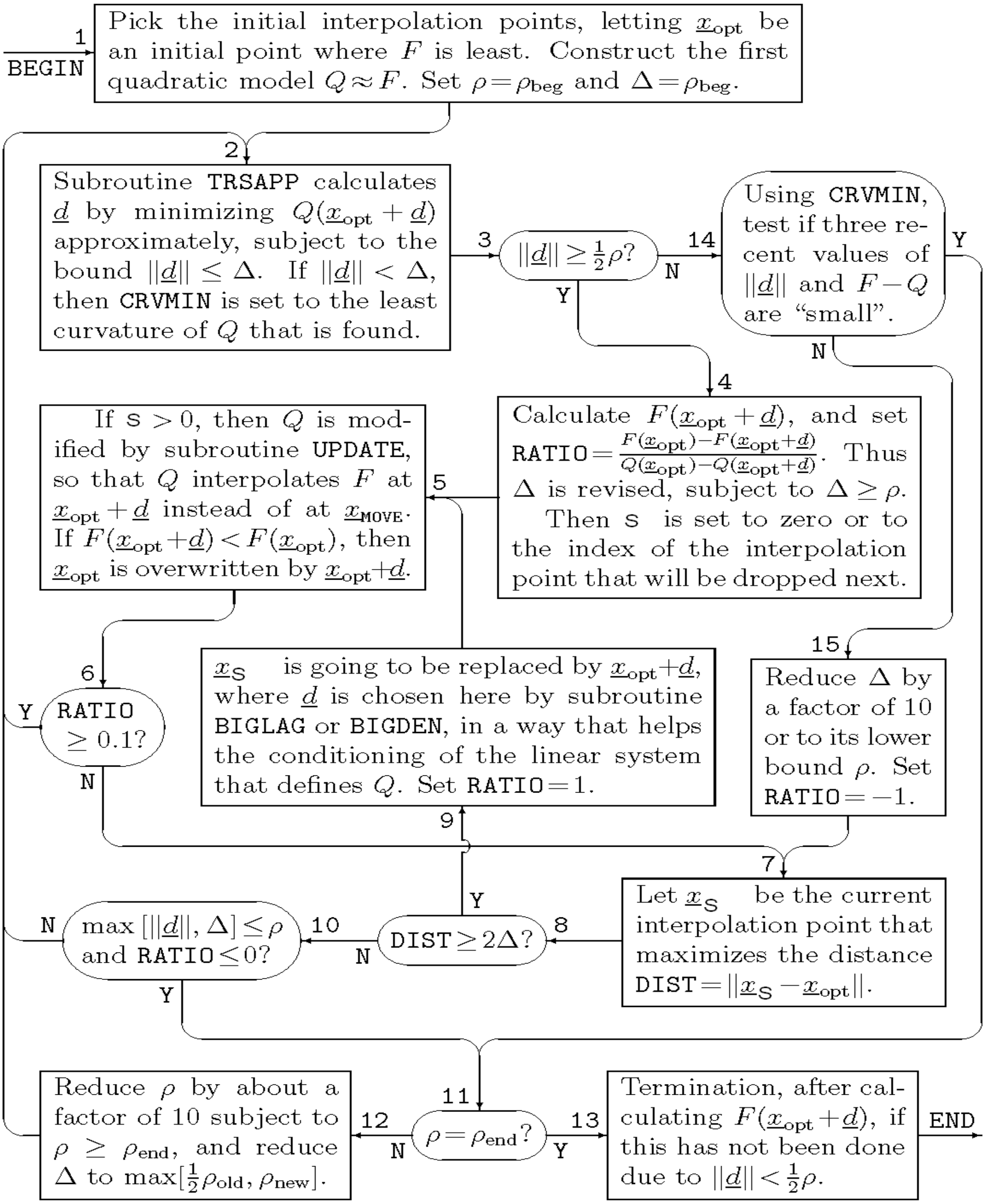

Figure 6.7: An outline of the NEWUOA method [3].

for $m \geq 2n+1$, the first $2n+1$ of the points $x_i$, $i = 1,2,...,m$, are chosen to be the vectors

$$\begin{aligned} x_1 &= x_0, & (6.9) \\ x_{i+1} &= x_0 + \rho_{beg} e_i & (6.10) \\ x_{i+n+1} &= x_0 - \rho_{beg} e_i & (6.11) \end{aligned}$$

for $i = 1,2,...,n$, where $\rho_{beg}$ is provided by the user. The parameter $e_i$ is the $i-th$ coordinate vector in $\mathbb{R}^n$ (see Fig. (6.8). They contain thus $x_0$ and fulfill the characteristic

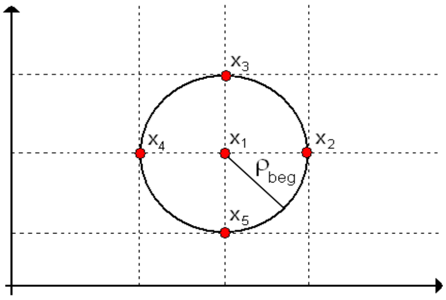

Figure 6.8: Initial iteration points of the NEWUOA method for $\mathbb{R}^2$.

$$\|x_i - x_0\|_\infty = \rho_{beg} \qquad (6.12)$$

Hence it follows that $Q(x_0)$, $\nabla Q(x_0)$ and the diagonal element of $(\nabla^2 Q)_{ii}$, $i = 1,2,...,n$ are clearly certain. $\rho^{(1)}$ one sets to $\rho_{beg}$, exactly the same as $\Delta^{(1)}$. $\Delta$ is the trust-region ratio, for all $\Delta \leq \rho$.

### The updating procedures

Here is considered the change that is made to the quadratic model $Q$ on each iteration of NEWUOA that alters the set of interpolation points.

Let $x_{opt}^{(k)}$, $k = 1,2,...$ the best vector variable to start the $k-th$ iteration, that $F(x_{opt}^{(k)})$ is the smallest computed value of $F$.

The quadratic model to start the $k-th$ iteration is the function

$$Q^{(k)}(x_{opt}^{(k)} + d) = F(x_{opt}^{(k)}) + d^T g^{(k)} + \frac{1}{2} d^T \nabla^2 Q^{(k)} d, \; d \in \mathbb{R}^n, \qquad (6.13)$$

with the vector $g^{(k)} \in \mathbb{R}^n$ and the symmetric $n \times n$ matrix $\nabla^2 Q^{(k)}$.

The interpolation conditions of $Q^{(k)}$ are the equations:

$$Q^{(k)}(x_j^{(k)}) = F(x_j^{(k)}), \; j = 1,2,...,m, \qquad (6.14)$$

where the point $x_j^{(k)} \in \mathbb{R}^n$, $j = 1,2,...,m$ are chosen automatically. One from them is the $x_{opt}^{(k)}$ and has the characteristic

$$F(x_{opt}^{(k)}) = min \left\{ F(x_j^{(k)}) : j = 1,2,...,m \right\}. \qquad (6.15)$$

The parameters $\rho^{(k)}$ and $\Delta^{(k)}$ are likewise needed in the $k-th$ iterations. $\Delta^{(k)}$ is a trust-region ratio, that the condition

$$\Delta^{(k)} \geq \rho^{(k)}, \; k = 1,2,..., \qquad (6.16)$$

fulfilled and $\rho^{(k)}$ is a positive number, which is degraded automatically by $\rho_{beg}$ on $\rho_{end}$. The most iterations is valid $\rho^{(k+1)} = \rho^{(k)}$, because the alternative $\rho^{(k+1)} < \rho^{(k)}$ is selected only if the barrier (6.16) prevents further progress. Therefore NEWUOA is also suitable for the minimization of very inaccurate target functions.

## Iterations

Exist two different iterations type, one is the "trust region" iteration and the other is the "alternative" iteration, as sketched on Fig. (6.9).

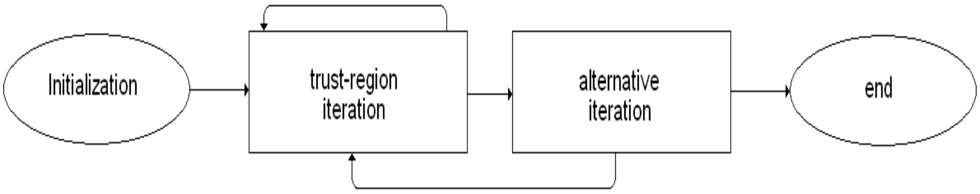

Figure 6.9: Iterations type for NEWUOA method [4].

**a) Trust-region iterations**

The trust-region iteration corresponds to the points 2-6 from the Fig. (6.7), summarizing on the Fig. (6.10). These points are processed in a sequence, a new value of $F$ is computed. The trust-region iteration generates a step $d^{(k)}$ of $x_{opt}^{(k)}$, the one approximate solution of the subproblems

$$min Q^{(k)}(x_{opt}^{(k)} + d)$$

and

$$||d|| \leq \Delta^{(k)}. \tag{6.17}$$

In the NEWUOA software this happens in the subroutine "TRSAPP". $d$ is computed with

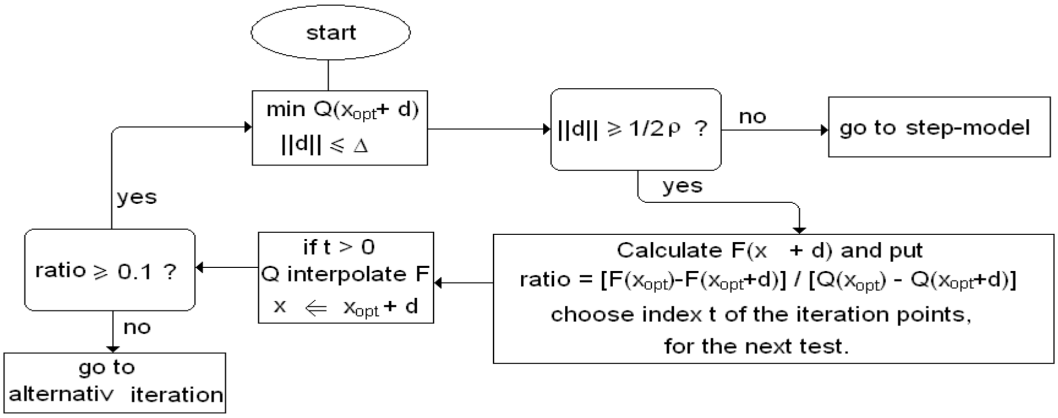

Figure 6.10: Trust-region iteration [4].

a version truncated the conjugate gradient method (described in appendix (9)). The decision if the new trust-region ratio $\Delta^{(k+1)} \geq \rho^{(k+1)}$ to be made smaller or larger, is given by

$$RATIO = \frac{F(x_{opt}^{(k)}) - F(x_{opt}^{(k)} + d^{(k)})}{Q^{(k)}(x_{opt}^{(k)}) - Q^{(k)}(x_{opt}^{(k)} + d^{(k)})}. \tag{6.18}$$

The numerator describes the actual reduction of $F$, while the denominator is the reduction forecast by the square model.

Determine

$$\Delta_{int} = \tfrac{1}{2}||d||, \quad RATIO \leq 0.1 \tag{6.19}$$

$$\Delta_{int} = \max\{||d||, 0.5\Delta^{(k)}\}, \quad 0.1 \leq RATIO \leq 0.7 \tag{6.20}$$

$$\Delta_{int} = \max\{2||d||, 0.5\Delta^{(k)}\}, \quad RATIO > 0.7. \tag{6.21}$$

For $\Delta^{k+1}$ arises then

$$\Delta^{k+1} = \rho, \quad \Delta_{int} \leq 1.5\rho \tag{6.22}$$

$$\Delta^{k+1} = \Delta_{int}, \quad \Delta_{int} > 1.5\rho. \tag{6.23}$$

For the case that

$$F(x_{opt}^{(k)} + d^{(k)}) < F(x_{opt}^{(k)}), \tag{6.24}$$

results for the new points of interpolation $x_j^{(k+1)}$, where

$$x_j^{(k+1)} = x_{opt}^{(k)} + d^{(k)}, \quad j = t, \ j = 1, 2, ..., m \tag{6.25}$$

$$x_j^{(k+1)} = x_j^{(k)}, \quad j \neq t, \ j = 1, 2, ..., m. \tag{6.26}$$

One of the current points $x_s^{(k)}$ for a time $t$ $[1; m]$ is replaced by $x_{opt}^{(k+1)} = x_{opt}^{(k)} + d^{(k)}$, all other points remain unchanged. The number $t$ describes which index of the interpolation point is replaced. Thus it is ensured with a reduction of the target function that the best computed values are for $F$ under the new interpolation conditions.

If $F$ does not decrease,

$$F(x_{opt}^{(k)} + d^{(k)}) \geq F(x_{opt}^{(k)}) \tag{6.27}$$

and the interpolations equation remain

$$x_j^{(k+1)} = x_j^{(k)},$$

for all

$$j = 1, 2, ..., m \tag{6.28}$$

and $t$ is set to zero.

If $RATIO < 0.1$, one changes $F(x_{opt}) - F(x_{opt} + d^{(k)})$ in the target function , which is unfavorable compared to the expected reduction $Q(x_{opt}) - Q(x_{opt} + d^{(k)})$. Normally this happens, if the positions of the points $x_i$ in the interpolation conditions (6.14) are unsuitable. On one trust-region iteration follows a further trust-region iteration, if the RATIO (6.18) is $RATIO \leq 0.1$, otherwise is the next iteration the "alternative".

**b) Alternative iterations**

Generally one tries "alternatives" to improve iterations of the square model, by shifting the point of interpolation which is the furthest from $x_{opt}^{(k)}$. This can be expressed, as a $s$ from $[1, m]$ evaluating the equation

$$DIST = \|x_s^{(k)} - x_{opt}^{(k)}\| = max \left\{ \|x_j^{(k)} - x_{opt}^{(k)}\| : j = 1, 2, ..., m \right\} \tag{6.29}$$

**b.1) First variant**

If the distance "DIST" is smaller than $2\Delta$, one uses the first variant described on Fig. (6.11). If the current points of interpolation $x_i^{(k)}$, $i = 1, 2, ..., m$ the norm

$$\|x_i^{(k)} - x_{opt}^{(k)}\| < 2\Delta, \ i = 1, 2, ..., m, \tag{6.30}$$

must be examined whether $\rho$ cannot be reduced. If one or several of the following conditions are valid:

1. $\|d\| > \rho$;

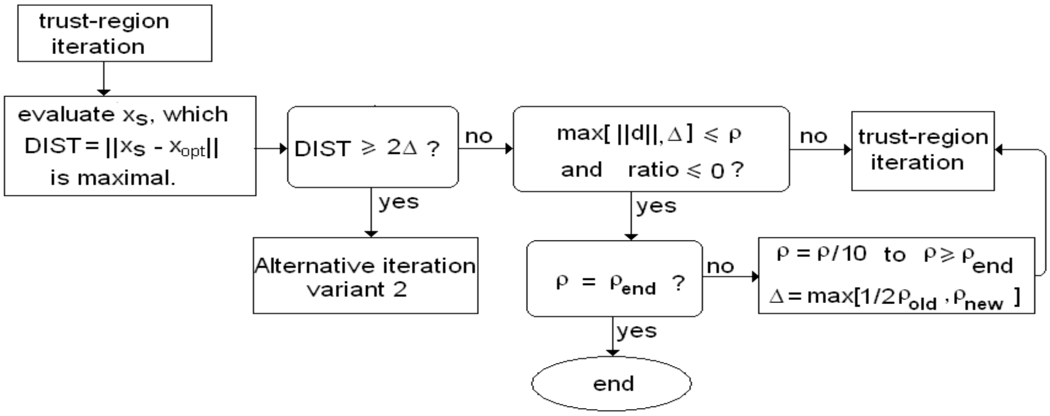

Figure 6.11: Alternative iteration - first variant [4]

2. $\Delta > \rho$ or
3. $RATIO > 0$.,

then$\rho^{(k+1)} = \rho^{(k)}$ and the trust-region will be started. In the first case, $\rho^{(k)}$ has the last choice of $d$ not limited. In the third case was $F(x_{opt} + d) < F(x_{opt})$ and as long as strict reductions in the target function are reached, one retains $\rho^{(k)}$.

Theoretically an infinite loop in $\rho$ could result. In practice however, the finite precision of computer arithmetic makes an upper barrier available for the number of the different values of $F$ which can occur. If $||x_s^{(k)}|| \leq 2\Delta^{(k)}$ then it is accepted that $x_s^{(k)}$ must not be shifted. Instead the trust-region iteration is rerouted or the iteration sequence with the current $\rho^{(k)}$ is terminated. The trust-region iteration without reduction of $\rho^{(k)}$ is preferred if one or both of the conditions $\Delta^{(k)} > \rho^{(k)}$ and $F(x_{opt}^{(k)}) < F(x_{opt}^{(k-1)})$ are fulfilled. If both conditions are not met, the next action depends whether on the lower bound of $\rho^{(k)}$ is reached or not. A time limitation enters the case $\rho^{(k)} = \rho^{(end)}$, and otherwise both $\rho^{(k)}$ and $\Delta^{(k)}$ are reduced,

$$\rho^{(k+1)} = \frac{\rho^{(k)}}{10} \; to \; \rho \geq \rho_{end} \tag{6.31}$$

$$\Delta^{(k+1)} = max\left[\frac{1}{2}\rho^{(k)}, \rho^{(k+1)}\right] \tag{6.32}$$

before the trust-region iteration is switched.

### b.2) Second variant

The variant 2 is described in Fig. 6.12. If $||x_s - x_{opt}|| \leq 2\Delta^{(k)}$, then $Q$ can be improved, as the interpolation condition $Q(x_s) = F(x_s)$ is replaced by $Q(x_{opt} + d) = F(x_{opt} + d)$, for a step $d^{(k)} \leq \Delta^{(k)}$. To update $Q$, the new function value $F(x_{opt} + d)$ must be computed before. If $RATIO = 1$, the trust-region iteration follows. So the algorithm can make immediately use of the new information in the quadratic model.

### c) Step-model

If in the trust-region enters

$$||d^{(k)}|| < \frac{1}{2}\rho^{(k)}, \tag{6.33}$$

then one assumes that $x_{opt}^{(k)} + d^{(k)}$ lies too near $x_{opt}^{(k)}$, therefore $d^{(k)}$ is rejected and changes the current iteration into one alternative iteration, or a test decides that the work with the

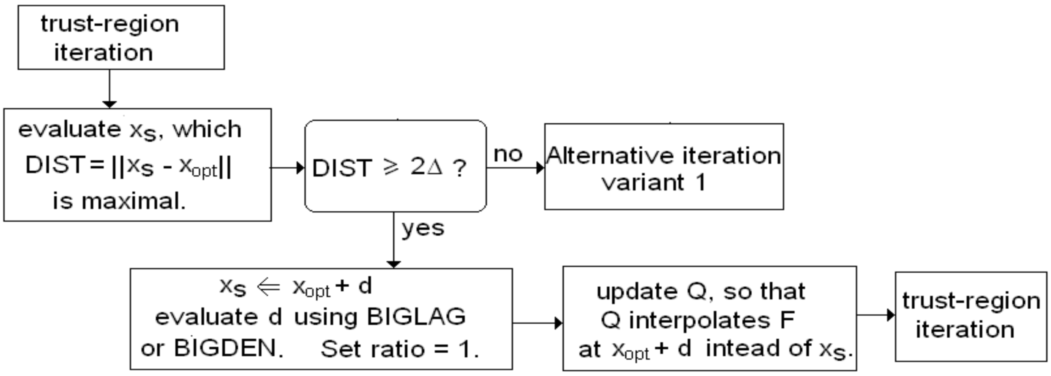

Figure 6.12: Alternative iteration - second variant [4].

current $\rho^{(k)}$ should be terminated. The target function $F(x_{opt}^{(k)}+d^{(k)})$ not will be evaluated.

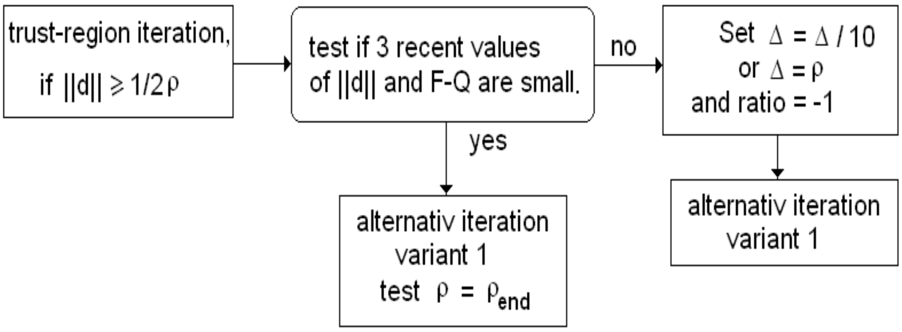

Figure 6.13: Step-model [4]

The difference $F(x_{opt}^{(k)})-F(x_{opt}^{(k)}+d^{(k)})$ tends to yield misleading information about the real target function if $||d^{(k)}||$ is small. If $||d^{(k)}|| \leq \Delta$ $Q$ has positive curvature along each search direction, and "CRVMIN" is set to the smallest value of these curvatures.

$$CRVMIN = min\left\{\frac{s_i^T\nabla^2 Q s_i}{||s_i||} : i = 1,2,...,j\right\} \tag{6.34}$$

with $j$ equal to the iteration numbers of the TCG-method.

The number of iterations of the last three cases are saved in the volume $\mathfrak{J}$. In addition the conditions

$$||d^{(j)}|| \leq \rho \tag{6.35}$$

and

$$|Q^{(j)}(x_{opt}^{(j)} + d^{(j)}) - F(x_{opt}^{(j)} + d^{(j)})| \leq \frac{1}{8}\rho^2 CRVMIN,\ j \in \mathfrak{J} \tag{6.36}$$

are examined. $Q^{(j)}$, $d^{(j)}$ and $x_{opt}^{(j)}$ are the $j_t h$ iteration. If the test fails negatively, either $\Delta^{(k+1)}$ becomes $\frac{1}{10}\Delta^{(k)}$ or reduces to $\Delta^{(k+1)} = \rho$ and $RATIO = 1$. Afterwards the first variant is executed as an "alternative" iteration. Therefore, either the interpolation points $x_s$ is replaced, the trust-region iteration is implemented with a new $\Delta^{(k+1)}$, or the work is finished with the current $\rho^{(k+1)}$. If the conditions 6.35 and 6.36 are fulfilled, then in the first variant the "alternative" iteration can be terminated with the evaluation of the current $||x_i^{(k)} - x_{opt}^{(k)}$, $i = 1,2,...,m$, although some distances $2\rho^{(k)}$ exceed the limits. The vector $d^{(k)}$ for which $||d^{(k)}|| \leq \frac{1}{2}\rho^{(k)}$ is often a good step of $x_{opt}^{(k)}$ into that area of the variables, therefore its use is desirable. There the square model in the following trust-region iteration remains the same and the new $\Delta^{(k+1)}$ with the characteristic

$$\Delta^{(k+1)} \geq \frac{1}{2}\rho^{(k)} > \|d^{(k)}\| \tag{6.37}$$

is retained; also $d^{(k+1)} = d^{(k)}$ is selected.

## 6.3 Computational details

In the present section artificially excited TS-waves are cancelled using plasma actuators operated in pulsed mode with two different signal modulations: rectangular and sinusoidal. Two different models of the actuator will be used: calibration based model and PIV based model, as discussed in Chapter 4. A pulsed excitation actuator is used upstream to excite oscillations in the boundary layer, provoking TS-waves. These are amplified by an adverse pressure gradient induced by an insert on the upper wall of the test section. A control plasma actuator creates an unsteady body force to attenuate the waves. As a result the amplitude of the velocity fluctuations at the excitation frequency is reduced. Numerical investigations using LES are conducted to identify the influence of the operation parameters of the control actuator for the two different modulations. The optimization algorithms were implemented in the FASTEST code, in which the operation parameters can be adjust during the simulation to obtain best cancellation results.

### 6.3.1 Computational domain

Fig. (6.14) shows the computational domain, identical to that used in previous chapters. However now, two velocity sensors are positioned at $x = 450$mm and $x = 550$mm, exactly 1mm from the wall. The control circuit uses the signal of the first velocity sensor to position the pulses of the first control actuator onto the maximum amplitude of the TS-waves. The signal of the second velocity sensor is used to analyze the downstream amplitude of the TS-waves. The circuit modifies three parameters involved in this process: duty cycle, phase shift and voltage, to achieve best cancellation results.

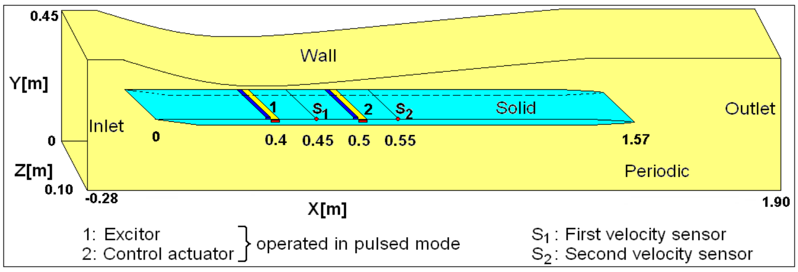

Figure 6.14: Overview of flow domain and actuator positions.

### 6.3.2 Operating modes

The body force induced by the plasma actuator is used to manipulate the transition process in boundary-layer flows, since the actuator accelerates the fluid in the lower parts of the boundary layer close to the surface, which leads to a modified boundary-layer profile. The body force created by the plasma actuator can be modified in several ways. Three possibilities are illustrated in the upper part of Fig. (6.15). The steady operation mode

(a) induces a steady body force generating a constant acceleration of the fluid close to the surface. Compared to the unsteady modes (b) and (c), mode (a) consumes considerable more energy. The two pulsed operation modes consume less energy but need very precise adjustment of several operating parameters to be effective in cancelling TS-waves. The use of complex control circuits is essential. However, a steady acceleration of the boundary layer can be advantageous as pointed out in [95]. This mode was presented in the previous chapters. The results of the wave cancellation with the two unsteady operation modes (rectangular and sinusoidal waves) are presented in the next sections.

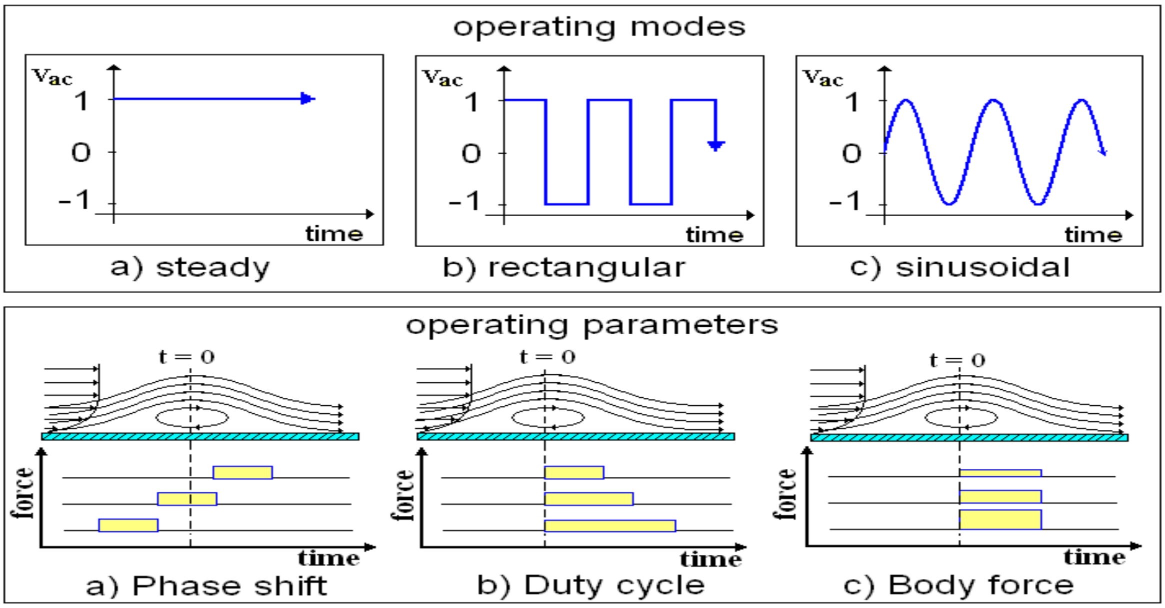

Figure 6.15: Three operating modes and parameters of the control actuator.

### 6.3.3 Operating parameters

Three parameters are identified to be significant for the quality of the cancellation. The lower left diagram of Fig. (6.15) illustrates the timing of the control pulse relative to the TS-wave, represented by the phase shift. The second sketch illustrates the duration of the pulse and the force, called duty cycle. The third parameter is the magnitude of the body force, illustrated by the right diagram (6.15). This parameter is controlled by the operating voltage of the plasma actuator. Changes of these parameters can be arbitrarily combined. For the sinusoidal modulation the parameter the duty cycle is no longer a relevant quantity and only the phase shift and the amplitude have to be controlled.

In both cases only one parameter can be controlled at a time. The change of each parameter produces different cancellation results. A combined change of more than one parameter cannot be analyzed by the present control algorithms. Optimal parameter combinations for the cancellation will be shown in the following sections.

## 6.4 Active wave cancellation (AWC)

In this section different methods to attenuate TS-waves using the optimization procedures described above will be presented. The closed-loop circuit was tested for two different operating modes (rectangular and sinusoidal). The NELMEAD and NEWUOA methods were tested only for the sinusoidal mode.

### 6.4.1 Rectangular modulation

In this case all of the 3 operating parameters have to be adjusted to reduce the amplitude of the TS-waves. The duration of each control pulse depends on the time in which the signal of the first velocity sensor (amplitude) exceeds this threshold. The change of the duty cycles for example relies on a threshold, as shown in Fig.(6.16). The level of this threshold is altered by the algorithm as described previously. This procedure yields maximal flexibility of the control circuit, since the circuit reacts on each wave individually. If the amplitude or the frequency of the TS-wave changes, the circuit will immediately adapt the operation parameters. The change of the duty cycle for example relies on an amplitude threshold from the first velocity sensor.

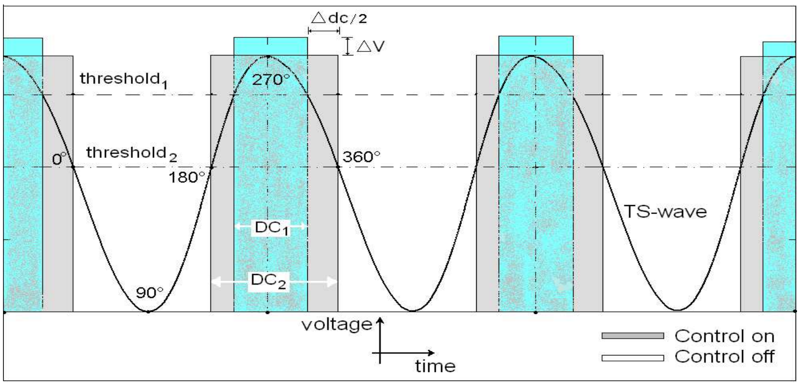

Figure 6.16: Outline of the operating parameters using threshold.

Fig. (6.17) shows the influence of the threshold in AWC using a constant positive variation of the threshold ($\Delta T^*$) in time. After t=3ms the closed-loop is turned on and the threshold takes the value $T^* = 0.65$m/s, obtained using the equation

$$T^* = (\tilde{Y}_{max} - \tilde{Y}_{min})/c, \tag{6.38}$$

where $\tilde{Y}_{max}$ and $\tilde{Y}_{min}$ is the maximum and minimum values of the TS-wave amplitude, respectively. The constant $c$ is reduced in time, increasing the threshold gradually. Amplifying the threshold, the duty cycle changes. As a result, the amplitude of the TS-wave is modified. When the duty cycle reaches a minimum, i.e., at t=12ms in this case, the parameters used in the plasma actuator control reduce significantly and the amplitude of TS-waves increases. Observe that in this simulation, the optimization algorithm was not working and the duty-cycle was changed from 50% until 0% to illustrate the effect of the duty cycle in the simulations.

In Fig. (6.18), the phase shift has been continuously changed in time in order to demonstrate the influence of this parameter on the amplitude of velocity fluctuations on the downstream sensor. In this picture, the best phase shift parameter can be observed at approximately $t = 18$ms ($\phi = 210^o$). The phase shift in this example has $\Delta\phi = 15^o$ per $\mu$s, where the complete cycle is achieved in 30$\mu$s.

Fig. (6.19) shows the temporal evaluation of the TS-waves using the rectangular modulation algorithm procedure described in section (6.2.1). The threshold changes during the simulations to yield the best parameters to reduce the TS-waves amplitude. The best parameters found in this situation was $\phi = 60\% DC$ and bf=5.6kV, which achieved a reduction of the TS-waves amplitude of 70%.

To demonstrate that the wave cancellation occurs not only near the wall but also in the upper regions of the boundary layer, the velocity at two different positions above the

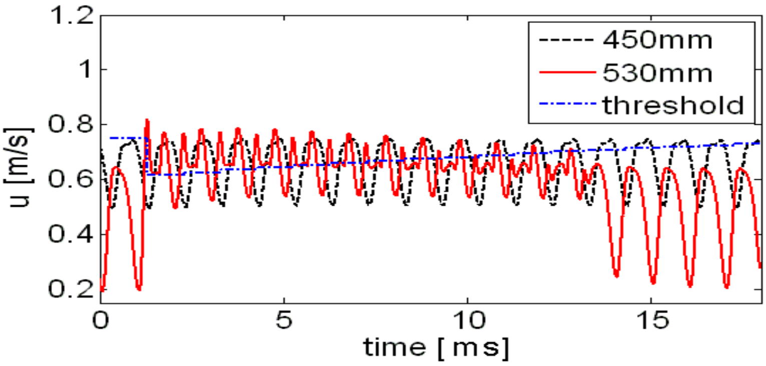

Figure 6.17: Influence of the threshold in active wave cancellation. The threshold amplitude increases linearly in time.

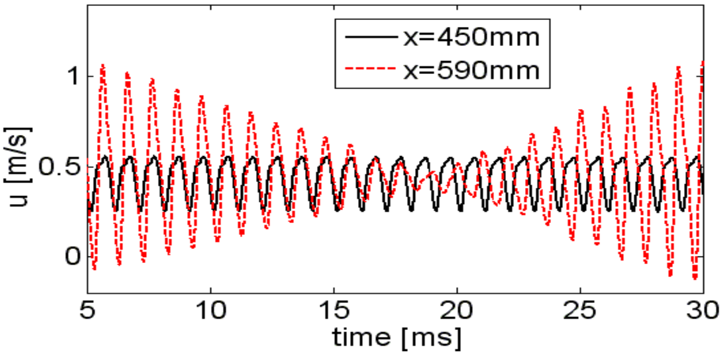

Figure 6.18: Phase-shift in time $\Phi = 180 - 340$ $(5 - 30\mu s)$.

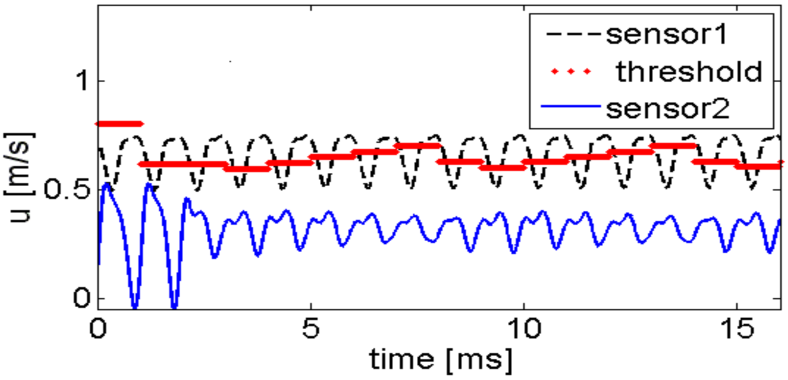

Figure 6.19: Threshold in AWC.

wall are plotted in Fig. (6.20). At both heights an amplitude reduction of 95% compared to the case without a control actuator working is achieved.

By examining Fig. (6.20) it can be observed that the cancellation of the TS-waves is not complete, which indicates that the procedure could be improved. This prompted investigation of a sinusoidal modulation of the body-force.

### Sinusoidal modulation

The active wave cancellation using sinusoidal modulation of the body force improves the adaption of the applied body force to the instantaneous magnitude of the wave. Using the

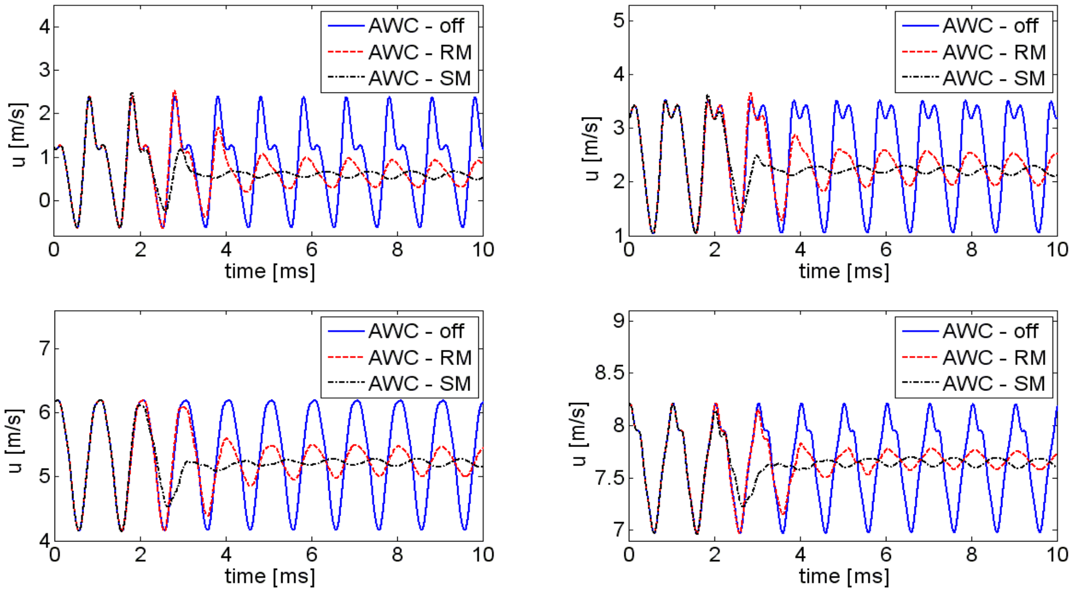

Figure 6.20: Amplitude of TS-wave analyzed at four positions above the plate at x=590mm.

function:

$$F = (bf + \Delta bf)sin(2\omega(t + \Delta\Phi)) \tag{6.39}$$

where $bf$ is the voltage, $\Delta\Phi$ is the time-step of phase shift and $\Delta bf$ is the time-step of voltage, the modulation of the plasma actuator operating voltage applied to the actuator follows the curvature of the wave amplitude. This more appropriate adaption of the force magnitude to the wave motion at any given time improves the cancellation results significantly. Another advantage of this operation mode is the fact that only two parameters need to be controlled. An attenuation of TS-wave amplitude of up to 95% can be achieved. Additionally the computational cost for the algorithm is reduced by 30% compared to the mode with rectangular modulation.

The improvement of the cancellation result by introducing a sinusoidal force modulation can clearly be seen in Fig. (6.21). The diagram shows the comparison of the velocity and turbulence intensity profiles of three cases: the base flow, wave cancellation with rectangular modulation (RM) and with sinusoidal modulation (SM).

To further look at the efficiencies and the differences between both modes, the wall shear stress is plotted in Fig. (6.22). At $x = 400$mm and $x = 500$mm, where the actuators are positioned, peaks of the wall friction occur due to the flow acceleration induced by the plasma actuator. The actuators add momentum to the flow and alter the velocity profiles for a short distance. Even the unsteady operation of the actuators alters the velocity profiles, since the force is oriented parallel to the wall. This leads to an additional effect besides the cancellation itself: as shown by Grundmann and Tropea in [41] the altered velocity profile leads to a stabilization of the laminar boundary layer. In the case of the wave cancellation a boundary-layer stabilization is superimposed to the cancellation effect. However, the altered velocity profiles decay rapidly after a short length downstream of each control actuator. Comparing both modulation modes, the sinusoidal modulation shows a higher efficiency in terms of wall-friction reduction. Applying the friction-force balance of the LES an overall reduction of 30% can be detected. This reduction is achieved

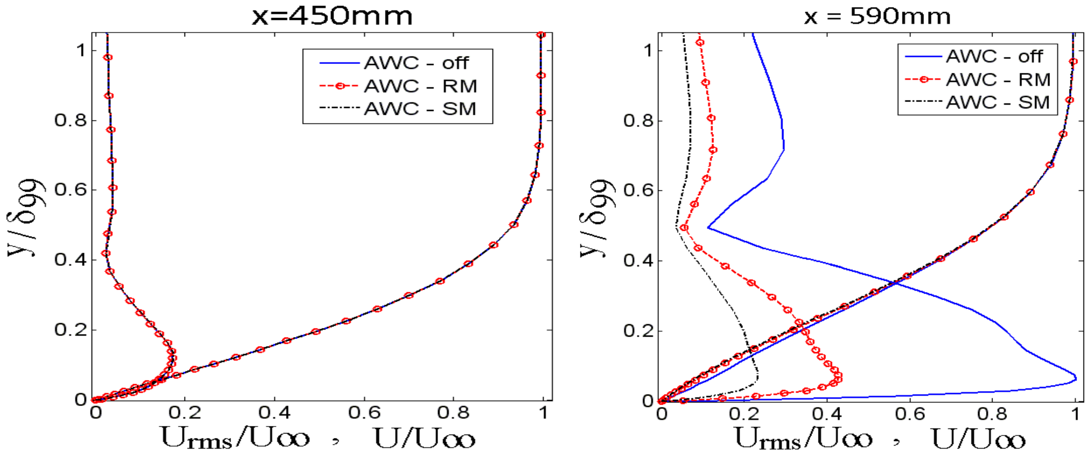

Figure 6.21: Comparisons of the velocities and turbulence intensities using two different force modulations.

solving the integral

$$\int_{le}^{te} \tau_w dx, \tag{6.40}$$

where $le$ and $te$ are the leading and trailing edge of the plate, respectively.

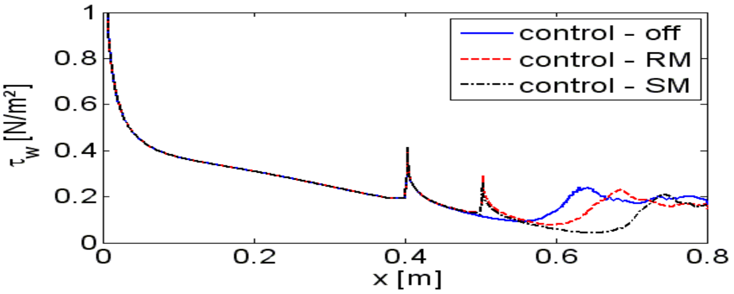

Figure 6.22: Wall shear stress comparison for both modes and the base flow.

Fig. (6.23) shows the comparison of the velocity profiles and fluctuation profiles of experimental results from [30] and [96] and the current numerical simulations 90mm downstream of the control actuator. In each case the operation parameters are adjusted precisely. All velocity profiles are equal, for the "on" and "off" cases as well as for the experimental and numerical case. However, the turbulence profiles have different shapes to the wall. These differences are attributed mainly to the fact that the experimental data has an influence of three-dimensional effects, such as streamwise vortices, which cannot occur in the quasi-2D numerical simulations.

Signal modifications of the voltage and the phase shift during the iterations are made according to the equations:

$$\begin{aligned} bf_i &= bf_i - (sgn)\alpha^* bf_{i-1} && (6.41)\\ \Phi_i &= bf_i - (sgn)\alpha^* \Phi_{i-1} && (6.42)\\ \Delta bf_i &= \alpha^{**} \Delta bf_{i-1} && (6.43)\\ \Delta \Phi_i &= \alpha^{**} \Delta \Phi_{i-1} && (6.44) \end{aligned}$$

where a relaxation factor is $\alpha^{**} = 0.2$ in this work.

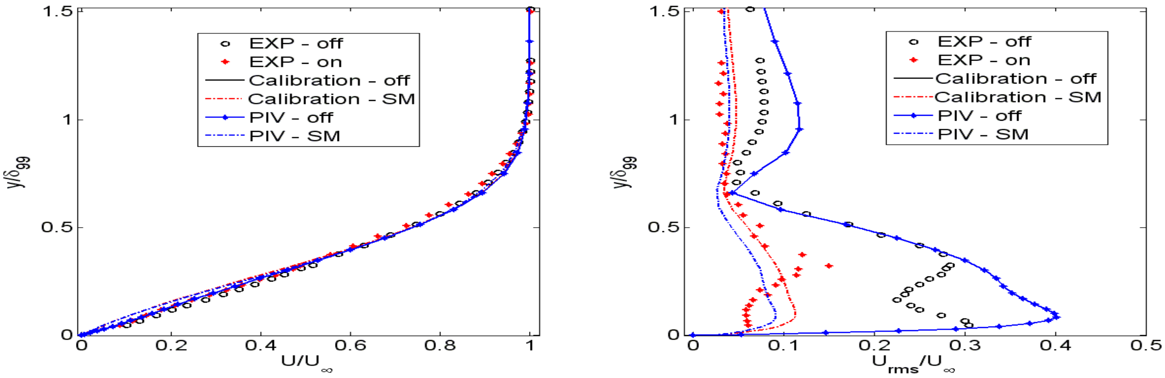

Figure 6.23: AWC comparisons with experimental data.

Table (6.1) shows the data evaluated during the optimization of voltage and phase-shift processes. In this case $\Delta bf_0 = 500V$, $bf_0 = 5000V$, $\Delta\Phi_0 = 180^o$ and $\Phi_0 = 20^o$. The convergency criterium adopted is given by

$$f_{opt} = f(\Phi_{max}, bf_{max}) - f(\Phi_{min}, bf_{min}) \leq 2 \times 10^{-1}, \tag{6.45}$$

because it is not expensive and yields satisfactory results.

Table 6.1: Voltage and phase-shift optimizations data using CLC.

| Voltage | Δ bf | signal | | Phase shift | Δ Φ | signal |
|---|---|---|---|---|---|---|
| 5000.00 | 500.00 | + | | 180.00 | 20.00 | + |
| 5500.00 | 500.00 | + | | 200.00 | 20.00 | + |
| 6000.00 | 500.00 | + | | 220.00 | 20.00 | + |
| 5600.00 | 100.00 | - | | 204.00 | 04.00 | - |
| 5520.00 | 020.00 | + | | 208.00 | 04.00 | + |
| 5540.00 | 020.00 | + | | 212.00 | 04.00 | + |
| 5560.00 | 020.00 | + | | 214.00 | 04.00 | - |
| 5580.00 | 020.00 | + | | 216.00 | 04.00 | - |
| 5564.00 | 004.00 | - | | 218.00 | 04.00 | - |
| 5568.00 | 004.00 | - | | 214.80 | 00.80 | - |
| 5564.80 | 000.80 | + | | 215.60 | 00.80 | + |
| 5565.60 | 000.80 | - | | 216.40 | 00.80 | + |
| 5564.90 | 000.16 | - | | 217.20 | 00.80 | - |
| | | | | 216.56 | 00.16 | - |

### 6.4.2 Nelder-Mead method

Applying the Nelder-Mead (Nelmead) method to optimize the operating parameters of the plasma actuator using sinusoidal modulation, the flow at three vertex are first simulated using the FASTEST-3D code. This vertex are given and the amplitudes of TS-waves (function) are evaluated. The data are presented in table (6.2). The initial vertex $\tilde{B} = (6050V, 210^o)$ corresponds to the parameters where the amplitude of TS-waves are more efficiently reduced in the first iterations. The worst vertex $\tilde{W} = (5850V, 230^o)$ attenuates the function poorly compared with the other two verticies and so will be rejected and replaced with a new vertex. The process generates a sequence of triangles, for which the function correspondent of the parameters at the vertices get smaller and smaller. The process stops when the objective function is reached, in other words, the amplitude of TS-waves are reduced below a prescribed threshold. The diagrams of Fig. (6.24) give further details about the steps of the triangle process generated in the algorithm during the optimization process. The first diagram shows the three initial parameters evaluated in the simulations. Diagram (b) shows the reflection of the worst vertex, which improves the solution compared with the other points and was considered a "good point". So the points are restructured again and the worst point will be reflected again and the parameters will be tested in the plasma actuator control trying to reduce the TS-waves. The diagram (e) shows the case where the result of the reflected point is worse than the point evaluated before (worst point). So two points were evaluated in the code ($\tilde{C_a}$ and $\tilde{C_b}$) and the point with the smaller function will be the vertex of the triangle. In this diagram the point was considered the best point to evaluate the function.

Table 6.2: Operating parameter optimizations data using Nelder-Mead method.

| k | Best point | Good point | Worst point |
|---|---|---|---|
| 1 | f(6050.00,210.00) | f(6350.00,220.00) | f(5850.00,230.00) |
| 2 | f(5550.00,220.00) | f(5850.00,230.00) | f(6050.00,210.00) |
| 3 | f(5550.00,220.00) | f(5850.00,230.00) | f(5350.00,240.00) |
| 4 | f(5550.00,220.00) | f(5875.00,217.50) | f(5850.00,230.00) |
| 5 | f(5550.00,220.00) | f(5575.00,207.50) | f(5875.00,217.50) |
| 6 | f(5550.00,220.00) | f(5575.00,207.50) | f(5250.00,210.00) |
| 7 | f(5550.00,220.00) | f(5575.00,207.50) | f(5408.00,211.80) |
| 8 | f(5562.50,213.80) | f(5479.00,215.90) | f(5550.00,220.00) |
| 9 | f(5562.50,213.80) | f(5479.00,215.90) | f(5491.50,209.60) |
| 10 | f(5562.50,213.80) | f(5506.10,212.20) | f(5479.00,215.90) |
| 11 | f(5562.50,213.80) | f(5506.10,212.20) | f(5589.60,210.10) |
| 12 | f(5562.50,213.80) | f(5506.10,212.20) | f(5506.65,214.45) |
| 13 | f(5562.50,213.80) | f(5506.10,212.20) | f(5561.95,211.55) |
| 14 | f(5548.12,212.28) | f(5562.50,213.80) | f(5506.10,212.20) |
| 15 | f(5530.71,212.62) | f(5548.12,212.28) | f(5562.50,213.80) |

The optimum parameters found using this method corresponds to $f(5530.71, 212.72)$ using a convergence error $\varepsilon_i \leq 2 \times 10^{-1}$, which is defined by equation (6.45). It is important to point out that each iteration carried through by the optimization method corresponds the two wavelengths (approximately 2000 iterations of the momentum equations into the FASTEST code). This time is necessary to evaluate the test function applied in the plasma control and to observe the effect in the amplitude of the wave. The amplitude of the TS-wave is controlled using the following equation:

$$\tilde{Y} = max(f(bf,\Phi)) - min(f(bf,\Phi)), \tag{6.46}$$

and the convergence criterium is given by equation (6.45). The convergence is satisfied after 15 iterations. The best voltage and phase shift found to reduce the TS-wave efficiently are $bf = 5530.71V$ and $ps = 212.72^o$ respectively.

The plasma actuator control and the velocity sensor used in the current optimization are situated at the same positions that were described in the previous section.

Fig. (6.25) shows the temporal evaluation of the optimization parameter at three different points on the flat-plate. At $x = 450$mm changes do not occur because this is

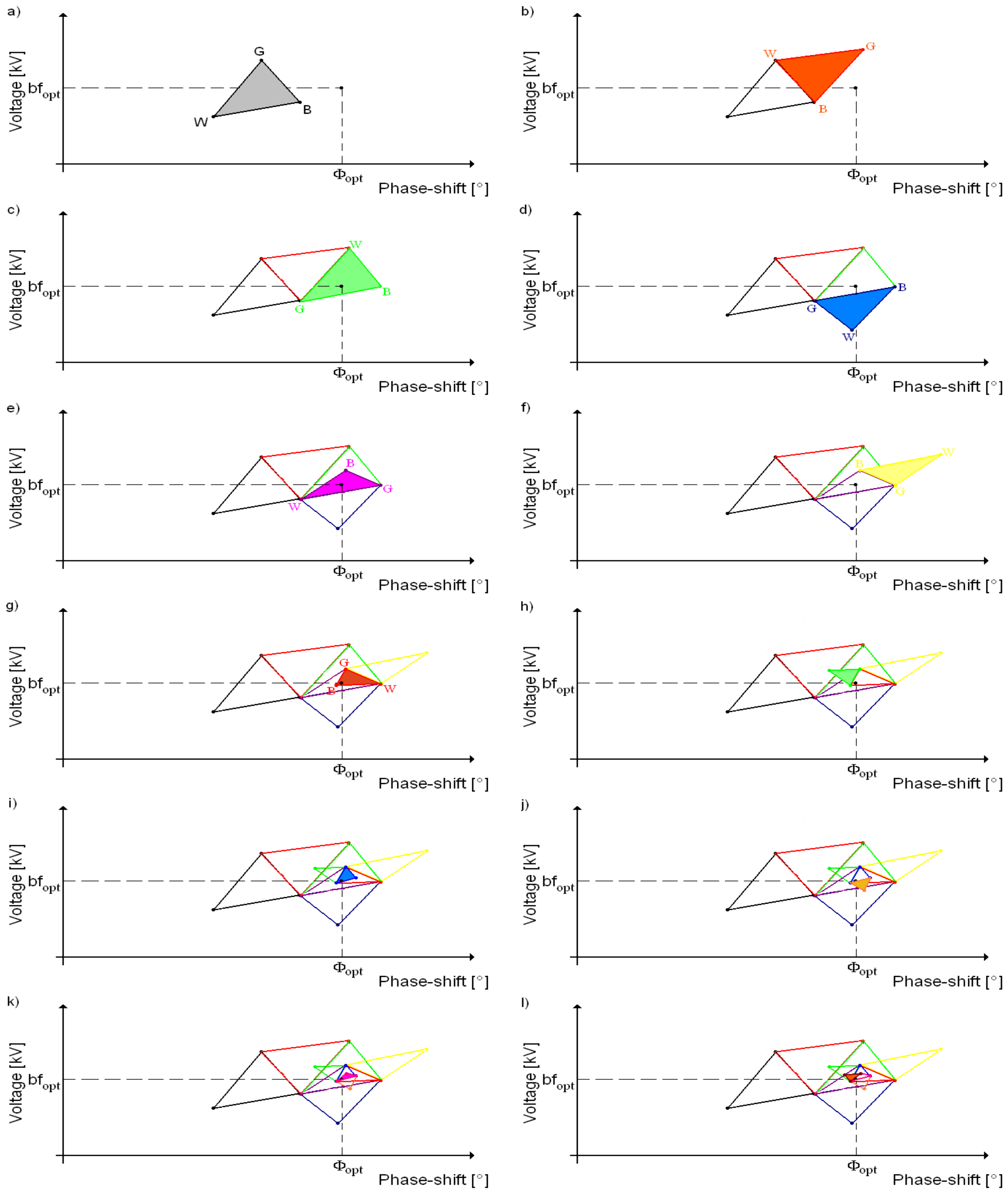

Figure 6.24: The sequence of triangle converging to the optimum point for the Nelder-Mead method.

situated before the control actuator. Analyzing the amplitude of the TS-waves 20mm downstream of the control actuator one observes that the variation of the maximum and minimum of the waves during the iterations are not large because the sensitivity of the parameters are affected by the jet created by the control actuator in the flow. However, at $x = 590$mm the sensibility of the parameters can be easily observed. These oscillations depend directly on the vertex that is being tested in the simulations.

Fig. (6.26) shows the comparisons between two optimization models at $x = 590$mm. The closed-loop control presents advantages to find the optimum parameter in this case in comparison with Nelder-Mead method. The Nelder-Mead method needs twice as much

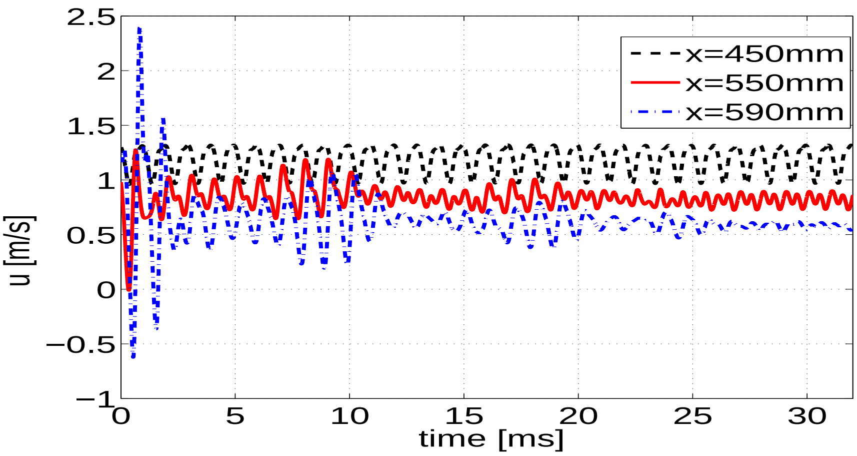

Figure 6.25: Amplitude of TS-wave comparison for three streamwise positions using Nelder-Mead method.

time to find the optimal parameter, corresponding to 25 iterations. Observe that the reduction of the amplitude of TS-wave correspond to 95% of the case without control actuator in both cases. This reduction affects directly the transition point on the flat-plate boundary layer as can see in the Fig. (6.22).

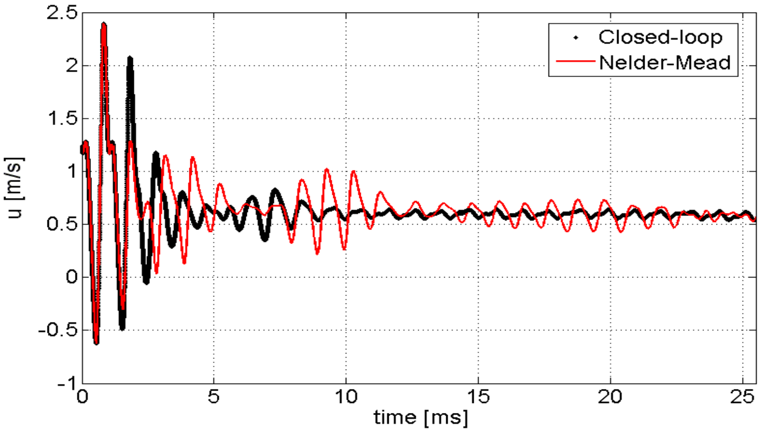

Figure 6.26: Amplitude of TS-wave comparison for two plasma actuator control using Nelder-Mead method.

The comparison of the Nelder-Mead method was tested for two different phenomenological plasma actuator models. The results are presented in the Fig. (6.27). Observe that the methods have some deviations along the simulations. These differences is explained by the fact that the initial vertex of the triangle are not the same, and so distinct vertex are tested in the current simulation.

The influence of the initial points affects the temporal evaluation directly, but the final optimum point is not affected. Fig. (6.28) shows two different initial points using Nelder-Mead method. The evaluation points are chosen systematically and at the same time the convergency criterium were satisfied for both cases. This shows that the optimum points are found independently of the chosen initial point.

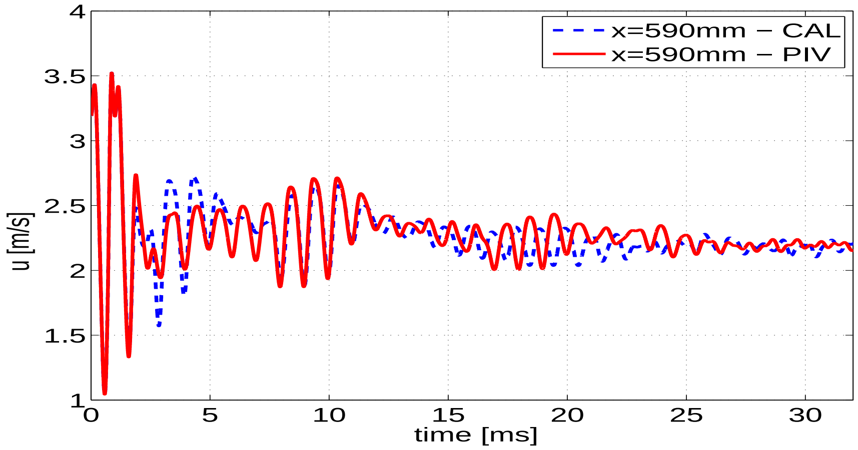

Figure 6.27: Amplitude of TS-wave comparison by Nelder-Mead method for two plasma actuator models.

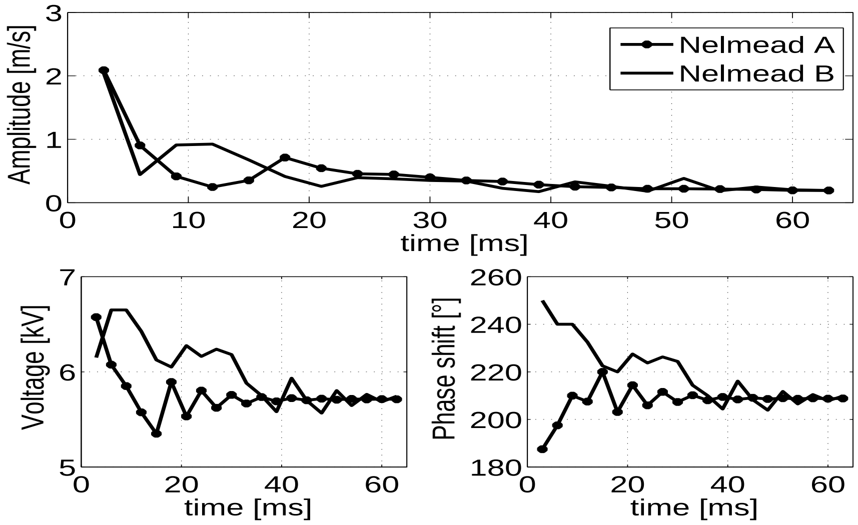

Figure 6.28: Comparison of amplitude, phase shift and voltage for two different initial points using Nelder-mead method.

### 6.4.3 NEWUOA method

The NEWUOA method is applied to optimize the operating parameters of the control actuators using also sinusoidal modulation. Fig. (6.29) shows the comparison of this method with other methods shown previously. This optimization method exhibits a low convergence rate but the results are excellent: the method reduces the amplitude of the TS-waves by 95%.

The works developed by Elsemüller [4], the initial ratio of the trust region is set to 5 points for each problem. The algorithm iterates until a minimum trust-region ratio is reached ($\rho_{end} = 10^{-3}$mm in our simulations).

Fig. (6.30) shows the convergence scheme to find the optimum in the NEWUOA method. First, a starting the vector $x^{(k)} \in \mathbb{R}^n$, for $n = 2$ and $k = 0, 1, ..., m-1$, also the values of the parameters $\rho_{beg}$ and $\rho_{end}$ and $m \in [n+2, 1/2(n+1)(n+2)]$. The value $m = 2n+1$ is recommended in this case. Here $\rho_{beg}$ and $\rho_{end}$ are the Euclidean lengths of changes that are made to the variables initially and at the end of the calculations, respectively, so $\rho_{beg} \geq \rho_{end}$ must hold and $\rho_{and}$ can be used to control the final accuracy.

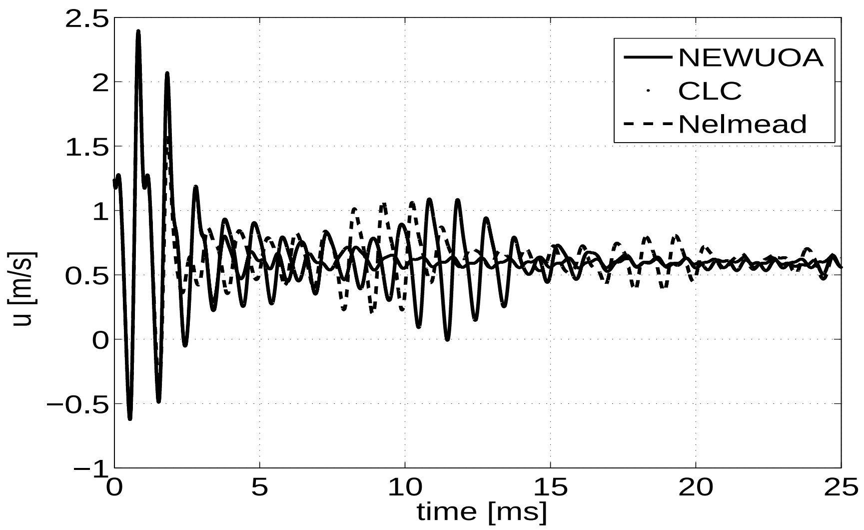

Figure 6.29: Amplitude of TS-wave comparison for three optimization methods.

The purpose of $m$ is that each iteration of NEWUOA employs a quadratic model[1] that interpolates just $m$ values of the objective function. Each iteration changes only one of the interpolation points, keeping $m$ fixed. Normally the $m$ chosen points are the best vector of variables at the beginning of the $k$th iteration, which means that $F(x^{(k)})$ is the least calculated value of $F$ so far. The step $d^{(k)}$ from $x^{(k)}$ is a vector $d$ that is calculated by applying an extension of the truncated conjugated gradient method to the subproblem

$$Minimize\ Q^{(k)}(x^{(k)}+d)\ subject\ to\ \|d\| \in \Delta^{(k)}. \tag{6.47}$$

If $\|d^{(k)}\| \geq 0.5\Delta^{(k)}$ occurs, this signifies that the next evaluated point is so near the previous point and $x^{(k)}$ is abandoned and an "alternative" type is switched on. Otherwise the new function value $F(x^{(k)}+d^{(k)})$ is calculated.

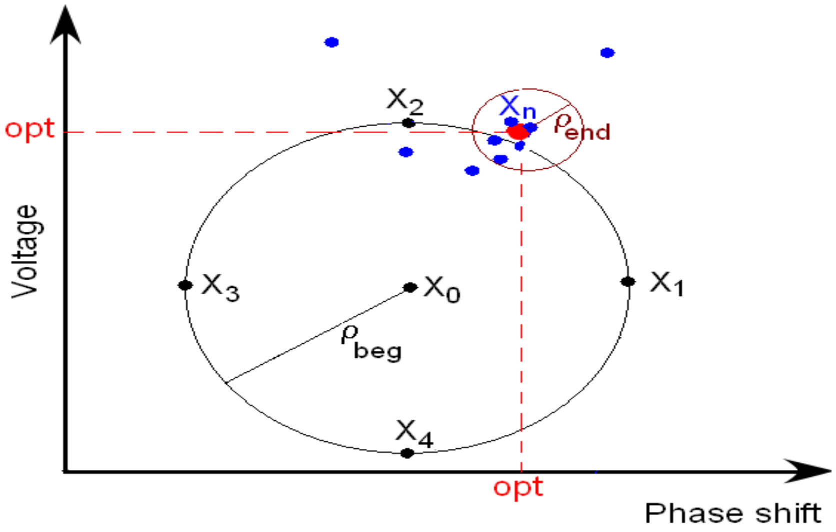

Figure 6.30: NEWUOA scheme.

Table (6.3) presents the data of the evaluation points of the NEWUOA method. The corresponding points of this table are shown in the Fig. 6.32. In this case $m=5$ was used.

---

[1] Quadratic polynomial approximation of $F(x^{(k)})$.

Initially the five points are evaluated and the amplitude and the target function for all points are found. Using these points the quadratic function is developed and the next point is evaluated such that the point that has the largest value of target function is discarded. In this example the point 4 presented the largest value, reaching 1179.27 points. Using the function $Q(x^{(1)})$ the next point 4 was evaluated. Now the amplitude of the TS-wave and the target function reduces significantly. Following to the next iteration and analyzing all evaluated points, the fifth point will be deleted in this step and a new quadratic function is calculated. With this new function the new point is evaluated. This process continues until the trust-region reduces to $\rho_{end}$, in other words, all tested points are inside of the trust-region. Thus the TS-waves are totally attenuated (target function reached). In this case the optimum body-force $bf_{opt} = 5394.11V$ and phase-shift $\phi_{opt} = 212.13$ was found, corresponding to the least target function $F_{target} = 284.40$.

Table 6.3: Operating parameter optimizations data using NEWUOA method.

| k×$10^3$ | point 1 | | | point 2 | | |
|---|---|---|---|---|---|---|
| | $f(bf,\phi)$ | amplitude | target f | $f(bf,\phi)$ | amplitude | target f |
| 12 | f(5000.00,210.00) | 0.689 | 683.09 | f(5500.00,210.00) | 0.172 | 346.92 |
| 14 | f(5000.00,210.00) | 0.689 | 683.09 | f(5500.00,210.00) | 0.172 | 346.92 |
| 16 | f(5000.00,210.00) | 0.689 | 683.09 | f(5500.00,210.00) | 0.172 | 346.92 |
| 18 | f(5000.00,210.00) | 0.689 | 683.09 | f(5500.00,210.00) | 0.172 | 346.92 |
| 20 | f(5000.00,210.00) | 0.689 | 683.09 | f(5500.00,210.00) | 0.172 | 346.92 |
| 22 | f(5000.00,210.00) | 0.689 | 683.09 | f(5500.00,210.00) | 0.172 | 346.92 |
| 24 | f(5389.89,213.12) | 0.135 | 287.81 | f(5500.00,210.00) | 0.172 | 346.92 |
| 26 | f(5389.89,213.12) | 0.135 | 287.81 | f(5340.38,213.26) | 0.162 | 288.98 |
| 28 | f(5389.89,213.12) | 0.135 | 287.81 | f(5340.38,213.26) | 0.162 | 288.98 |
| 30 | f(5389.89,213.12) | 0.135 | 287.81 | f(5340.38,213.26) | 0.162 | 288.98 |
| 32 | f(5389.89,213.12) | 0.135 | 287.81 | f(5340.38,213.26) | 0.162 | 288.98 |
| 34 | f(5389.89,213.12) | 0.135 | 287.81 | f(5397.28,212.20) | 0.150 | 295.44 |
| 36 | f(5389.89,213.12) | 0.135 | 287.81 | f(5397.28,212.20) | 0.150 | 295.44 |
| 38 | f(5390.91,212.20) | 0.154 | 297.90 | f(5397.28,212.20) | 0.150 | 295.44 |
| 40 | f(5390.91,212.20) | 0.154 | 297.90 | f(5397.28,212.20) | 0.150 | 295.44 |

| k×$10^3$ | point 3 | | | point 4 | | |
|---|---|---|---|---|---|---|
| | $f(bf,\phi)$ | amplitude | target f | $f(bf,\phi)$ | amplitude | target f |
| 12 | f(5000.00,220.00) | 0.2508 | 466.54 | f(4500.00,210.00) | 0.458 | 1179.27 |
| 14 | f(5000.00,220.00) | 0.2508 | 466.54 | f(5765.09,218.48) | 0.218 | 524.75 |
| 16 | f(5000.00,220.00) | 0.2508 | 466.54 | f(5765.09,218.48) | 0.218 | 524.75 |
| 18 | f(5479.22,211.18) | 0.1531 | 324.95 | f(5765.09,218.48) | 0.218 | 524.75 |
| 20 | f(5479.22,211.18) | 0.1531 | 324.95 | f(5765.09,218.48) | 0.218 | 524.75 |
| 22 | f(5479.22,211.18) | 0.1531 | 324.95 | f(5455.12,214.12) | 0.145 | 317.20 |
| 24 | f(5479.22,211.18) | 0.1531 | 324.95 | f(5455.12,214.12) | 0.145 | 317.20 |
| 26 | f(5479.22,211.18) | 0.1531 | 324.95 | f(5455.12,214.12) | 0.145 | 317.20 |
| 28 | f(5394.11,212.13) | 0.1425 | 284.40 | f(5455.12,214.12) | 0.145 | 317.20 |
| 30 | f(5394.11,212.13) | 0.1425 | 284.40 | f(5360.84,211.38) | 0.168 | 296.83 |
| 32 | f(5394.11,212.13) | 0.1425 | 284.40 | f(5360.84,211.38) | 0.168 | 296.83 |
| 34 | f(5394.11,212.13) | 0.1425 | 284.40 | f(5360.84,211.38) | 0.168 | 296.83 |
| 36 | f(5394.11,212.13) | 0.1425 | 284.40 | f(5392.13,212.04) | 0.145 | 285.84 |
| 38 | f(5394.11,212.13) | 0.1425 | 284.40 | f(5392.13,212.04) | 0.145 | 285.84 |
| 40 | f(5394.11,212.13) | 0.1425 | 284.40 | f(5392.13,212.04) | 0.145 | 285.84 |

| k×$10^3$ | point 5 | | |
|---|---|---|---|
| | $f(bf,\phi)$ | amplitude | target f |
| 12 | f(5000.00,200.00) | 0.374 | 729.55 |
| 14 | f(5000.00,200.00) | 0.374 | 729.55 |
| 16 | f(5632.05,205.75) | 0.238 | 413.90 |
| 18 | f(5632.05,205.75) | 0.238 | 413.90 |
| 20 | f(5435.75,213.52) | 0.145 | 303.70 |
| 22 | f(5435.75,213.52) | 0.145 | 303.70 |
| 24 | f(5435.75,213.52) | 0.145 | 303.70 |
| 26 | f(5435.75,213.52) | 0.145 | 303.70 |
| 28 | f(5435.75,213.52) | 0.145 | 303.70 |
| 30 | f(5435.75,213.52) | 0.145 | 303.70 |
| 32 | f(5406.32,212.11) | 0.1552 | 301.83 |
| 34 | f(5406.32,212.11) | 0.1552 | 301.83 |
| 36 | f(5406.32,212.11) | 0.1552 | 301.83 |
| 38 | f(5406.32,212.11) | 0.1552 | 301.83 |
| 40 | f(5397.07,212.05) | 0.1447 | 295.09 |

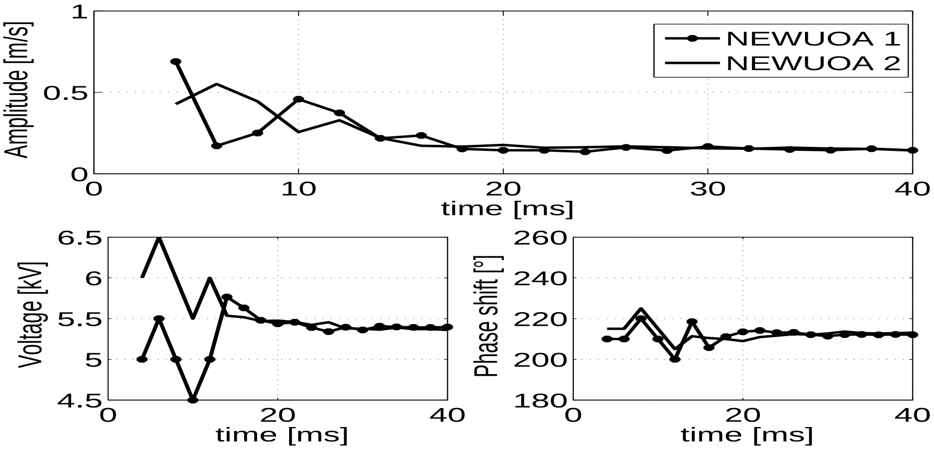

Figure 6.31: Comparison of amplitude, phase shift and voltage for two different initial points using NEWUOA method.

Fig. (6.31) shows two independent simulations using different initial points to start the NEWUOA method. In the simulation 1 the initial parameters are described in the table 6.3 and in the second case was used $x_1 = (6000, 210)$; $x_2 = (6500; 210)$; $x_3 = (6000; 220)$; $x_4 = (5500; 210)$ and $x_5 = (5000; 200)$. Observe that in both cases the optimum parameters were found in $20\mu s$ approximately. The optimum parameter in the second case was $x_{opt} = (5389, 16; 212.26)$. The temporal evolution of the velocity profile at the second sensor was described in the Fig. (6.32). In this case a reduction of 96% of the amplitude of TS-wave was found, as confirmed in the upper diagram of the Fig. (6.31).

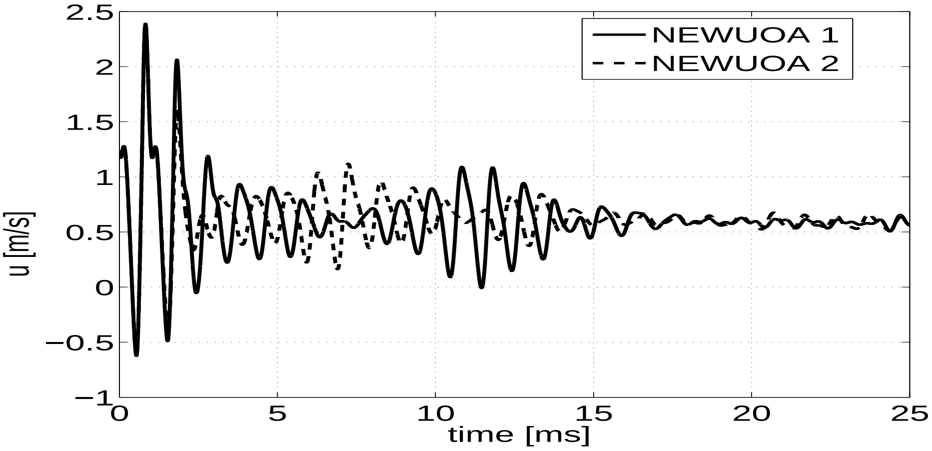

Figure 6.32: Comparison with two initial points using NEWUOA at x=590mm.

## 6.5 Conclusions

At this point it is interesting to draw comparisons among the three methods of optimization investigated in this study. This has been done on the basis of various criteria, as summarized in Table 6.4.

The first criterium is the computation cost and to provide the given computational times the three methods were compared running on the same computer and with the same initial conditions. The initial voltage was $bf = 6050$V, the initial phase shift $\phi = 180^o$. The results were obtained running on 8 parallel processors (AMD64 Opteron QUAD 32Gb RAM) using MPI (Message Passing Interface).

The closed-loop control method yields acceptable results with a relatively low computational demand. Such a control is however restricted to optimizing only up to three, possibly four parameters. Furthermore, only local optimization minima may be found. The NELMEAD method is easy to implement, achieves a good results and is also relatively fast. The best suppression of Tollmien-Schlichting waves was found using the NEWUOA method and this method can be extended to operate on many parameters. However this method requires significantly more optimization steps and is therefore much more demanding in computational load. For the present application, the NELMEAD appears to be the most suitable method of optimization.

Table 6.4: Optimal operating parameters comparison.

| | CLC | NELMEAD | NEWUOA |
|---|---|---|---|
| Computational time(h) | 18 | 24 | 32 |
| Phase shift($^o$) | 216.56 | 212.62 | 212.13 |
| Voltage(V) | 5564.90 | 5530.71 | 5394.11 |
| Damping rate(%) | 90 | 92 | 95 |
| parameters | max 3 | n | n |

# 7 Applications

## 7.1 Introduction

In this section two applications using the optimized parameters will be presented: In the first subsection a theoretical application using linear stability theory will be shown. The stability theory will analyze the stability property of a set of boundary-layer profiles using plasma actuators using the optimal parameters found in each operating mode presented in the previous sections. The optimal parameters will be taken the parameters obtained using the CLC method; In the second part the NELMEAD method will be implemented on-line in the experimental facility.

## 7.2 Application of stability theory

In order to support the current investigations of plasma actuators at the Institute of Fluid Mechanics and Aerodynamics in Darmstadt a linear stability analysis program was utilized to compute the stability properties of a set of boundary-layer profiles manipulated by plasma actuators. Reeh [5] has observed that the boundary-layer profile shape may influence the stability characteristics considerably.

In order to investigate the plasma actuator's influence on flow stability and to verify existing experimental and numerical results, linear stability analysis is conducted. The manipulation of the boundary-layer profiles by the plasma actuator, i.e. the higher velocities near the surface, is expected to have a stabilizing effect. Therefore, the stability calculations are supposed to show the flow's reduced affinity to become unstable. On the other hand, it clearly needs to be pointed out that the plasma actuator's mode of operation itself represents a disturbance source. This section concentrates on the stability properties of modified boundary-layer profiles as if there were no further influences.

The linear stability analysis method can only be used to calculate stability properties for a specific base flow profile. Generally, the shape of the base flow profile changes moving further up or downstream in the flow domain. For the stability properties of a specific base flow profile, a stability calculation for each evaluated profile is necessary. The boundary-layer profiles are investigated in the region 0.48m $\leq x \leq$ 0.6m in intervals of 0.1m. Especially the derivatives of the mean velocity profiles shape changes drastically depending on the $x$-position and the actuator model used, as shown in Fig. (7.1).

The stability calculations were performed using two different phenomenological actuators models (see section (4)). In the first case the plasma actuator control is switched off in order to obtain the flow stability behavior with uncontrolled TS-waves growth as a reference. In the controlled cases, the excitation actuator using rectangular modulation and two control actuator models using sinusoidal modulation driving voltage were used in opposite phase to the arriving waves. Both wave-cancelation methods proved to be effective. Observe that the first velocity profile does not change too much in both cases, but the first streamwise derivative as well as the second streamwise derivative changes considerably downstream of the actuator control, as showed in Fig. (7.1) at $x = 510$mm. The PIV based method yielded slightly more precise results in the neutral curve plots (Fig. (7.2) at $x = 520$mm), followed by the calibration based model using sinusoidal modulation,

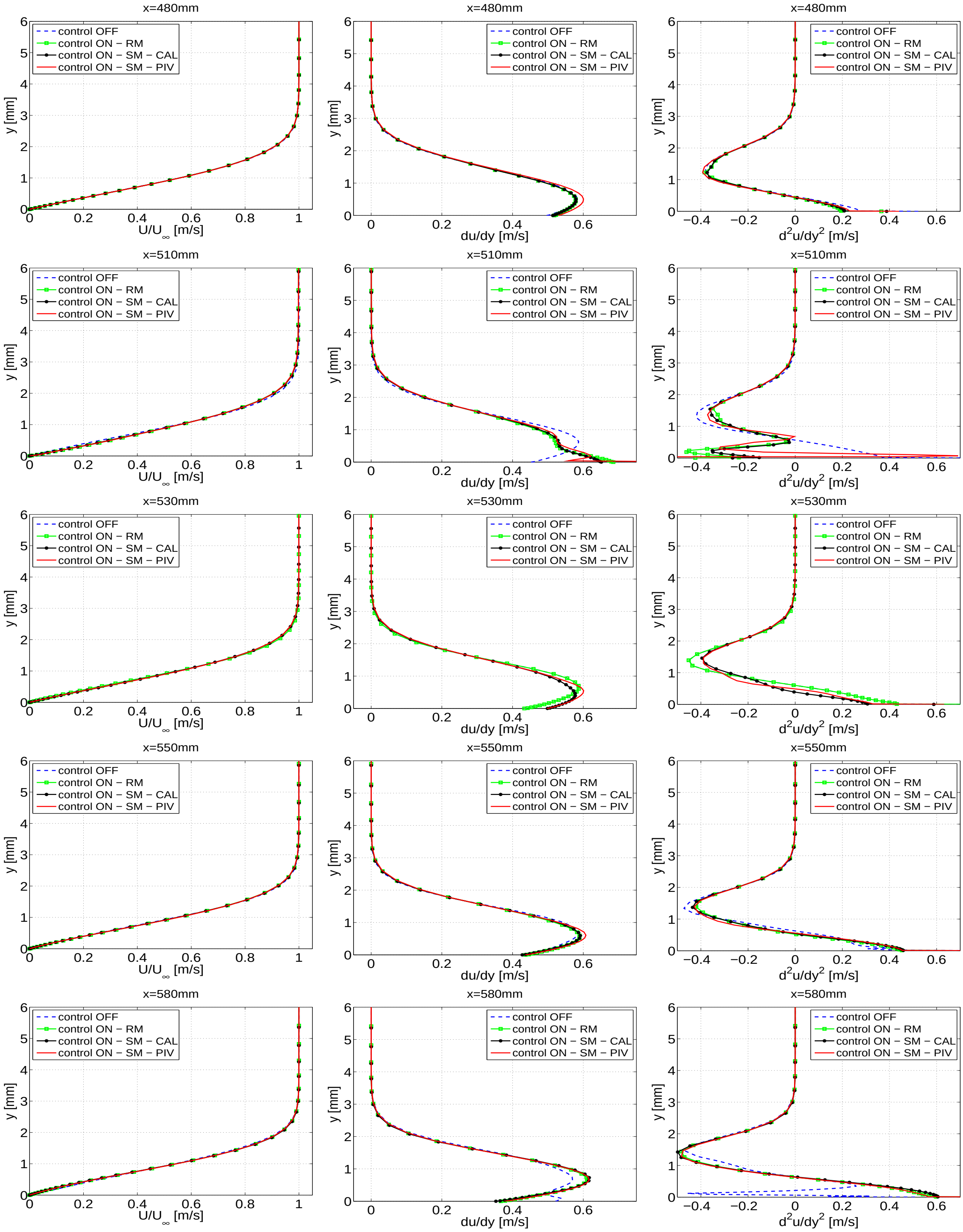

Figure 7.1: Mean velocity profiles and derivatives for the uncontrolled and the pulsed case at different streamwise positions.

which turned out to be more successful in canceling TS-waves compared by rectangular modulation mode. In the rectangular modulation model more energy is inserted into the manipulation process. This can be observed in the upper diagram of the Fig. (6.15) by comparing the areas enclosed by the course of the modulation voltage and the line of zero

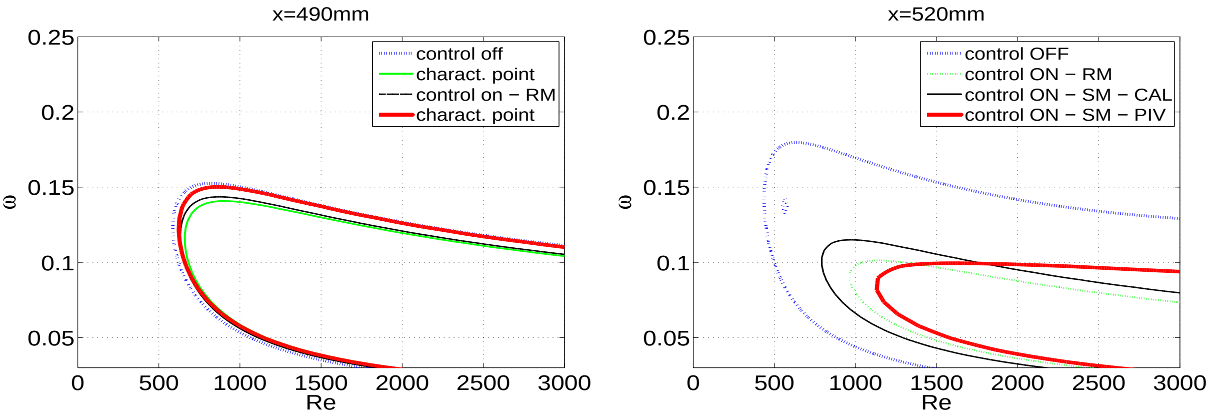

Figure 7.2: Comparison of the neutral curve manipulations for uncontrolled operation, rectangular modulation, calibration and PIV based using sinusoidal modulation for two different streamwise positions.

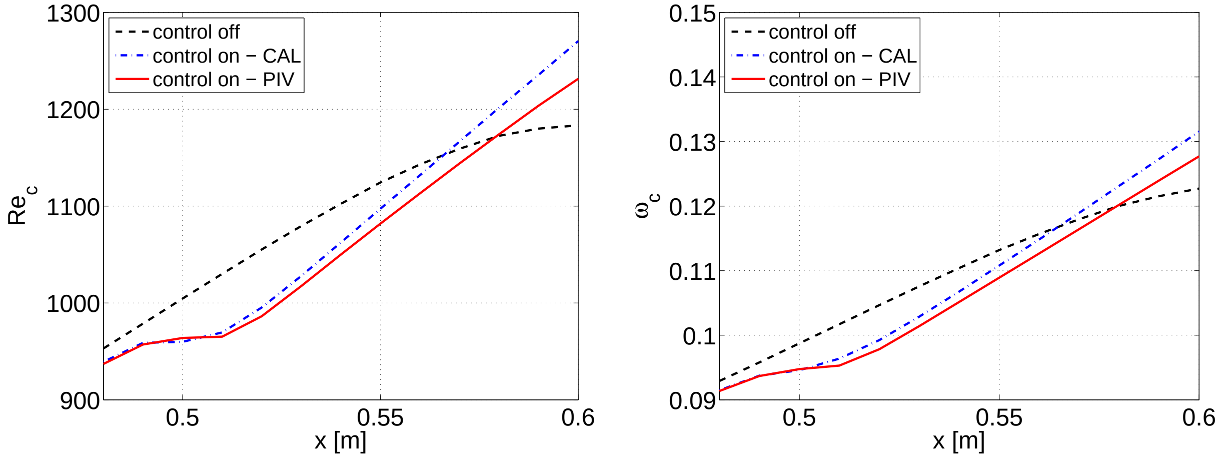

Figure 7.3: Variation of the characteristic Reynolds number and the characteristic angular frequency due to the manipulations induced by the plasma actuator.

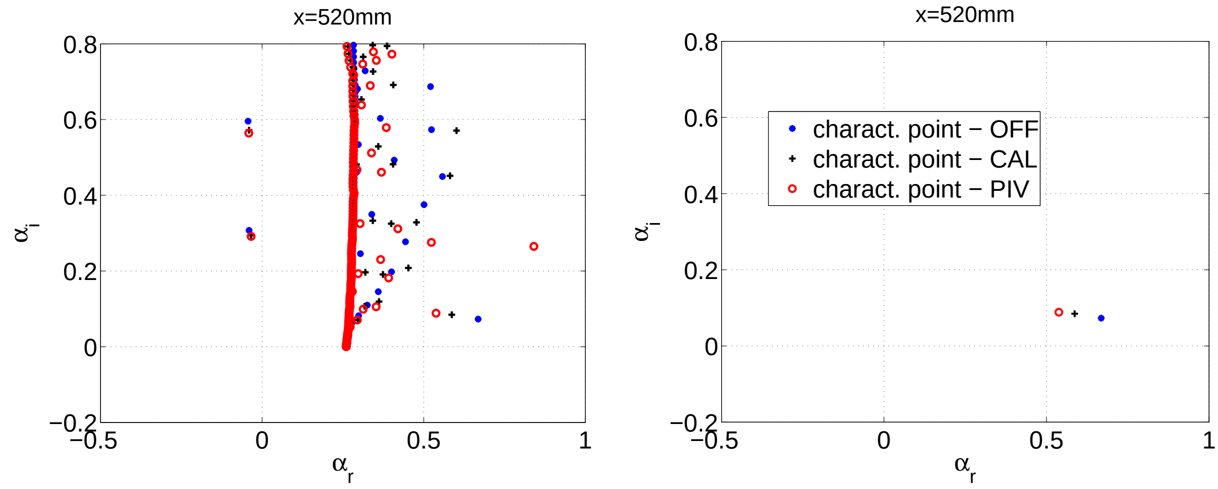

Figure 7.4: Comparison and filter of the results of the different actuation methods. The spatial eigenvalue spectrum is obtained with the parameters $\omega = 0.26$, $\beta = 0$ and $Re = 2000$ [5].

voltage for both cases. Yet, the sinusoidal modulation observed in PIV based method is more aligned to the shape of the TS-waves and thus is more successful in canceling these waves. One can see in the neutral curve plot at $x = 490$mm in Fig. (7.2) there are almost no differences in the critical Reynolds in all 4 studied cases, since the effect of the plasma actuator control is not present in this position.

The total transition delay results from both effects, the wave cancelation and the stabilization of the base-flow profiles. Sinusoidal modulation turned out to be more successful [97] and is therefore preferable, but calculations have also been performed for the rectangular modulation case. The stabilizing effect of the boundary-layer manipulation by plasma actuators could be demonstrated and the results may be used for the validation of the preceding investigations.

Another important effect in the stability analysis is the spectrum of the eigenvalues. Fig. (7.4) shows a typical spatial eigenvalue spectrum of the investigated boundary-layer flow. The spatial formulation of the Orr-Sommerfeld eigenvalue problem is more appropriate since convective instabilities are investigated. The majority of eigenvalues are densely located on an almost vertical line. Some eigenvalues seem to break out of the line and only a few discrete eigenvalues exist to the far left. The vertical line is a discrete representation of a continuous spectrum [16]. Due to the discrete nature of the solution procedure, the continuous line of the spectrum is composed of closely spaced eigenvalues. The eigenvalues in the continuous spectrum do not contribute to the modal stability characteristics of the flow. Only the discrete ones determine whether the flow is exponentially stable or unstable [5]. These discrete eigenvalues, denoted characteristic points, will be taken into account to evaluate the instability of the flow. The characteristic points are shown in the right side of Fig. (7.4) for the cases without actuator control and using sinusoidal modulation for two studied methods.

The shape change in the base-flow velocity profiles causes a tremendous increase of the critical Reynolds numbers and the instability region decreases significantly in the affected region around the plasma actuator (Fig. (7.3)). The discrete points in the neutral curve plots represent the current state of the flow defined by the characteristic Reynolds number $Re_{\delta_1}$ and the dimensionless angular frequency of the artificial TS-waves $\omega = \frac{2\pi F \delta_1}{U_\delta}$. It can be observed that these identities vary only slightly in the $x$-direction. Hence, the linear stability determining effect must actually come from the change of the boundary-layer profiles.

In order to demonstrate the differences and the stabilizing effects of the plasma actuator, instability curve computations have been performed in the spatial framework. As the neutral curve diagrams at ten different $x$-positions demonstrate (Fig. (7.5)), wavelike disturbances grow in the uncontrolled case exponentially for all positions. In the uncontrolled case the amplitude of the artificial waves in the region $x > 0.56$ has amplified to an extent that nonlinear effects become important. At $x = 580$mm the nonlinearities in the second derivatives of the velocity profiles (Fig. 7.2) are visible, characterizing that the flow turns totally unstable. Fig. (7.6) demonstrates clearly the positive effect of the plasma actuator with remarkably reduced growth rates of the primary instabilities compared to the uncontrolled case in the sinusoidal modulation cases; one can also observe differences between calibration and PIV based method. In the region 0.48m$\leq x \leq$ 0.54m instabilities of the Tollmien-Schlichting type, but at remarkably lower growth rates. The control actuator's acceleration of fluid material close to the surface is similar to the effect of a favorable pressure gradient [5]. Instabilities amplify more slowly and thus avoid early transition. Nonlinearity enters later into the problem and the whole process of disturbance growth is displaced further downstream. In Fig. (7.7) the evolution of the critical Reynolds number

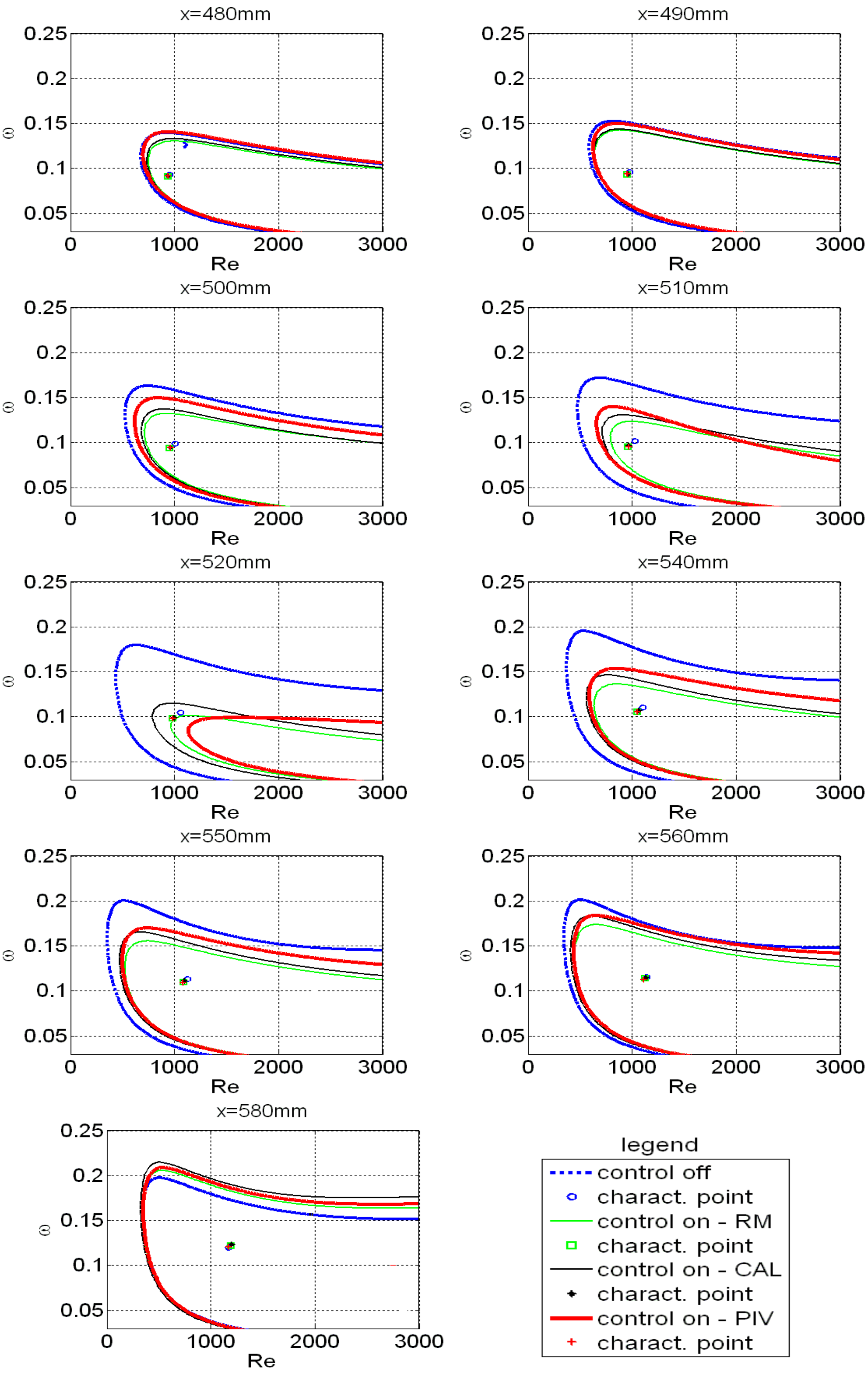

Figure 7.5: Manipulations of the neutral curves at different streamwise positions.

as a key figure of modal stability analysis is compared to the uncontrolled case.

Wave cancelation is an important reason for the observed transition displacement. If

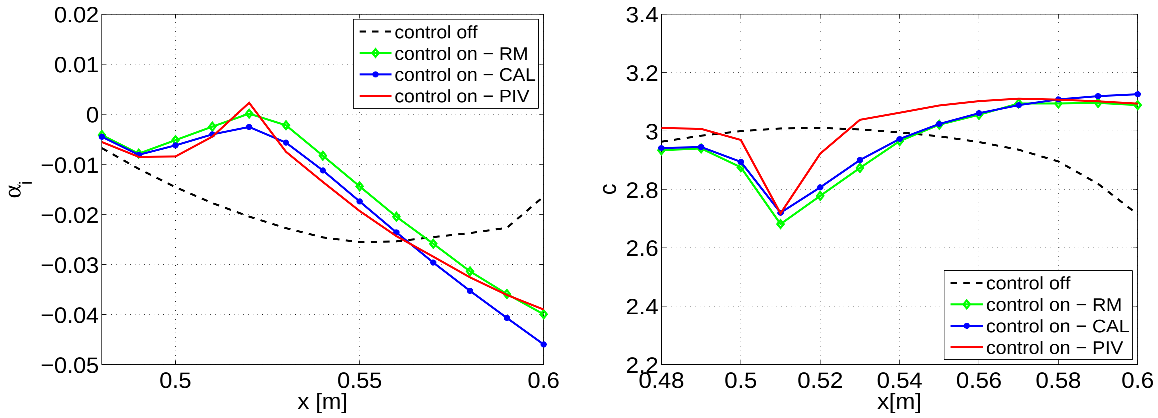

Figure 7.6: Exponential growth rates and phase speeds at different *x*-positions [5].

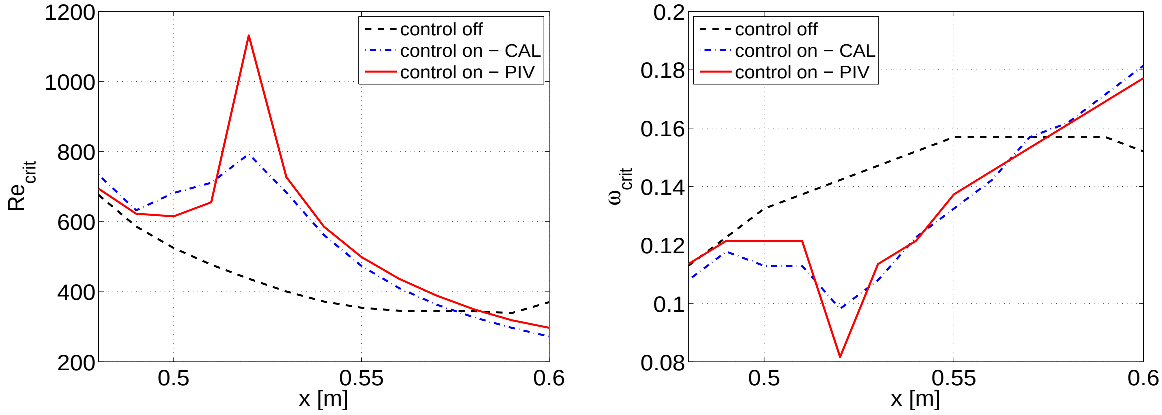

Figure 7.7: Alteration of the critical Reynolds number and the critical angular frequency [5].

disturbance waves can be cancelled or damped, they need additional time to recover and to grow in amplitude until reaching a nonlinear state. During that time the wave propagates of course and the onset of transition is delayed. It should be mentioned once again that only the alterations of the boundary-layer profiles caused by the actuation have been investigated in this linear stability analysis and not the wave cancelling mechanism. It was clearly shown that the stabilizing effect of the plasma actuator is also an important factor in transition manipulation and delay.

## 7.3 Experimental closed-loop control

Since the wave cancellation depends on a precise adjustment of several parameters, best results can only be obtained with a closed loop control circuit that gains information about the cancellation results from a sensor, as discussed before. To validate that the methods presented in section 6.4 also wind tunnel experiments can be used the control or optimization algorithms implemented in Labview. For this purpose the NELMEAD method is chosen because of its implementation simplicity. Experiments are carried out at the Low-Speed Wind Tunnel Facility at Technische Universität Darmstadt for a boundary layer developing along a flat plate. A detailed description of the experiment can be found in [30].

Grundmann [30] presented a closed loop control based on a rather simple approach in which the potential of this technique can be demonstrated. In tests realized by Güttler

[96], two parameters were simultaneously optimized. The control circuit alternates between the control of the phase difference between the excitation and the control actuator, and the duty cycle of the attenuation simultaneously, using the operations of NELMEAD method to find the best vertices of the triangle. The step size of the parameter changes per cycle depends on the actual amplitude to enable the circuit to find the minimum quickly with large steps and to maintain the optimal cancellation using small step sizes.

A result of this wave-cancellation control circuit is shown in Fig. 7.8 for three velocity magnitudes. The upper diagram of Fig. 7.8 shows the Tollmien-Schlichting wave reduction using $u = 10.8\text{m/s}$. The control circuit is activated at the time $t = 20\text{s}$. Before that time the amplitude diagram shows the amplitude of the uninfluenced TS-waves. Quickly after the activation a minimum of the amplitude was found by the automated adaption of the phase and the duty-cycle. The peaks occur due to an initial parameter used to evaluate the first three vertices of the triangle, following the algorithm described in the section 6.2.2. The control actuator is turned off after 30s. One observes that the amplitude of TS-waves returns to the original level. The reduction of 70% of the TS-wave amplitude can be observed when the control circuit is activated again ($t = 60\text{s}$), demonstrating the potential of an optimization method for close-loop control.

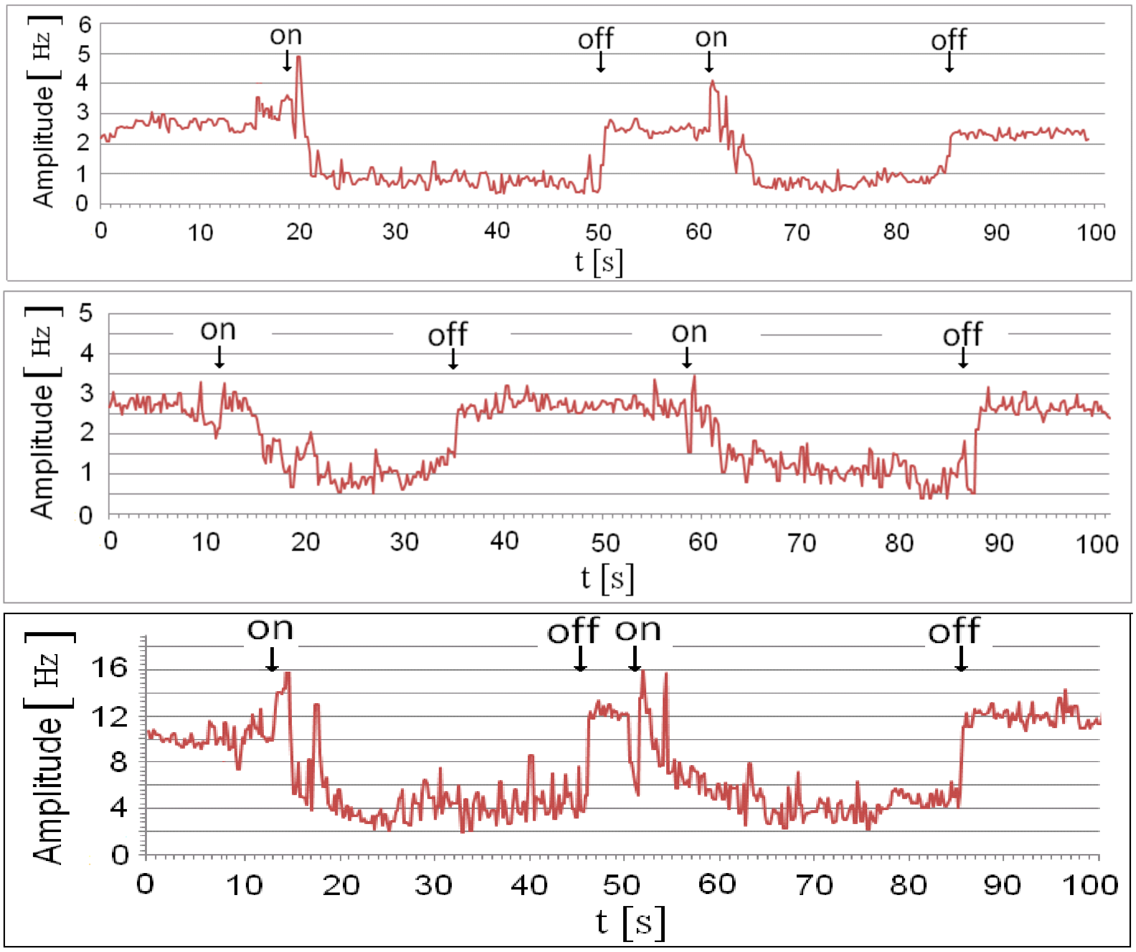

Figure 7.8: Experimental AWC results obtained with NELMEAD method with velocity: u=10.8ms(up); u=14.4m/s(middle) and u=21.4ms(below).

The middle diagram of Fig. 7.8 shows the experimental AWC results using NELMEAD method for the velocity $u = 14.4\text{m/s}$. The best parameter found corresponded to DC=67.3%

Table 7.1: Parameters used in the experiments

| velocity [m/s] | Voltage [kV] | duty cycle [%] | frequency [Hz] |
|---|---|---|---|
| 10.8 | 6.4 | 55.2 | 100 |
| 14.4 | 6.3 | 67.3 | 100 |
| 21.5 | 8.5 | 52.4 | 200 |

and ps=$210^o$ using a frequency of TS-wave equivalent to 100Hz. Some deviations prejudiced the convergency of the method, however a reduction ratio of 60% has been achieved. At t=60s the plasma actuator control was activated again. Note that many evaluations of the amplitude were necessary to reduce the TS-wave significantly.

The velocity magnitude u=21.5m/s was achieved in measurements represented in the lower diagram of Fig. 7.8. High amplitude oscillations were observed in this diagram, but nevertheless the optimization procedure functioned very well and despite these oscillations quite large attenuation rates of 65% were obtained. Table 7.1 summarizes the parameters used in the measurements.

# 8 Conclusions and Perspectives

## 8.1 Conclusions

In this thesis the transitional boundary layer in the presence of a strong adverse pressure gradient, controlled by continuously and pulsed operated plasma actuators was successfully investigated. This study has been performed at a free-stream velocity of 8 m/s (measured downstream of the displacement body). LES using the Germano method has been shown to be a viable approach for such flows. To improve the reliability of the results and to overcome the uncertainty of LES modelling of the early-stage of transition, comparisons with DNS and experimental results have been performed. It has been found that very good agreement of both numerical approaches with the experimental results exist.

A rather simple actuator model is found to adequately capture the process that leads to a delayed transition to turbulence in both actuator operating modes. The high instability and also the impracticability of the rectangular modulation in practice, shows that this mode should be changed for the sinusoidal modulation in the control of the TS-waves. The overall wall friction drag could be reduced by 30% using a sinusoidal modulation when the momentum input of the plasma body force is included in the force balance, demonstrating the large potential of this technique for wall-friction reduction applications. These highly satisfying results are encouraging and beg for further investigations of the more detailed process of wave cancelation.

When optimizing only two parameters of the plasma actuator, the method developed in this work presented better convergence compared with NELMEAD and NEWUOA methods. However, for $n \geq 3$ parameters the closed-loop control method becomes inviable computationally and the other two algorithms maintain the same velocity of convergence. The NEWUOA method is more precise than the other two optimization methods once such a method has a second-order approximation.

Analyzing the two applied models for the body-force distributions, the following conclusions are drawn:

- large differences exist between the body-force distributions of both models;
- different force distributions yield different wave-attenuation results;
- the force distribution derived from the PIV measurements [98] is more efficient for the boundary-layer stabilization;
- the force distribution generated by the calibration based model is more efficient for the active wave cancellation.

Usually it is very difficult to discover general convergence theorems for nonlinear optimization algorithms that perform well in practice, especially when first derivatives are not available. However the results presented in this study demonstrate the robustness and practicality of the three methods implemented into the CFD FASTEST code. These results indicate that unconstrained optimization algorithms, specifically direct search methods, deserve further attention for this particular application.

Another conclusion from this study is that the final set of optimization parameters is not particularly sensitive to the model used to provide the induced body forces from the plasma actuator. This suggests that the lessons learned about optimization approaches here, can easily be carried over to simulations using more refined plasma actuators models in the future.

This work is only an introduction of the plasma actuator thematic and now using these optimizations methods in the implemented computational code, future researchers can use these tools to find the best configurations of the plasma actuators for many applications. In the next section some application possibilities for these techniques will be presented including a discussion of what needs to be done to improve and apply them in practice.

## 8.2 Perspectives

The developed optimization schemes can now also be applied to other areas of flow control with plasma actuators. Interesting operating parameters that should be addressed include electrode gap and width, voltage, frequency, electrode size, etc.

Studies at the Institute of Fluid Mechanics and Aerodynamics involve experimental, numerical and theoretical investigations for a better understanding of the plasma actuator's operating principle [99]. An optimization of operation and an extension of the flow-control applications, showing the high importance of the actuator's geometrical configuration to the spatial velocity distribution are currently being investigated. Kriegseis et al. [100] developed measurements of plasma actuators with different electrode widths operated in quiescent air. Different actuators operating at the same voltage and frequency clearly show different flow fields. Many different electrode widths were tested but a more comprehensive investigation of the fluid field dependency on electrode width is currently being performed and in the meantime the development of an optimization procedure becomes necessary; hence the present numerical study can now can be applied in this direction.

The greatest concern with DBD plasma actuators, according to Choi and Jukes [101], lies in the authority, efficiency and durability. These are the issues to the future development of DBD plasma actuators. Thus, some topics in general require more specific investigations and must be carried out as a part of the system optimization process:

1. Applied voltage and frequency: What are the upper and lower limits of applied voltage and frequency for DBD plasma actuators? What are the optimized combination of voltage and frequency to give the best actuator authority?

2. Voltage profile and duty cycle: Which voltage profile should be applied to the actuators to maximize their authority? How can we optimize the voltage cycles to ensure the best efficiency and durability of actuators?

3. Power consumption: How much of the input power is used to generate the surface plasma and how much should be used for the dielectric heating? Can we reduce the power consumption of the actuators by optimizing the flow control technique and/or by improving the actuator design?

4. Electrode geometry: How does the geometry of the plasma electrodes affect the actuator authority? Can we improve the efficiency and durability of plasma actuators by optimizing the electrode geometry?

5. Dielectric sheet material: How does the dielectric sheet material (dielectric constant) affect the authority of plasma actuators? What other dielectric materials are available to improve the authority, efficiency and durability of plasma actuator?

6. Dielectric heating and thermal material [102]: How does the thermal cycle due to plasma heating affect the durability of actuators?

7. Ambient pressure and relative humidity [103], [104]: One knows that the effect of the environmental conditions like ambient pressure and relativity humidity have significant contribution in the efficiency of the plasma actuators. Therefore, a set of new parameters must be taken into account in the simulations to find the best configurations for a plasma actuator.

The methodology developed in the present thesis is capable of helping indirectly in the most items described above and the first three items can be easily evaluated using the current technique.

For application of the developed closed-loop under realistic conditions the influence of noise and other disturbances needs to be considered. As a first step in this direction, a distorted signal was artificially generated in the simulation. Figure (8.1) shows the time traces of the instantaneous velocity fluctuations in an uncontrolled flow due to presence of the TS-wave at a wall-normal distance of $y = d_{99}$. At $t = 15$ms a gust occurs and lasts for 10ms. The time trace of the velocity signal reveals that this gust strongly influences the TS-wave. In minor intensity this variation is also detected at $y = 1$mm where the velocity sensor is positioned.

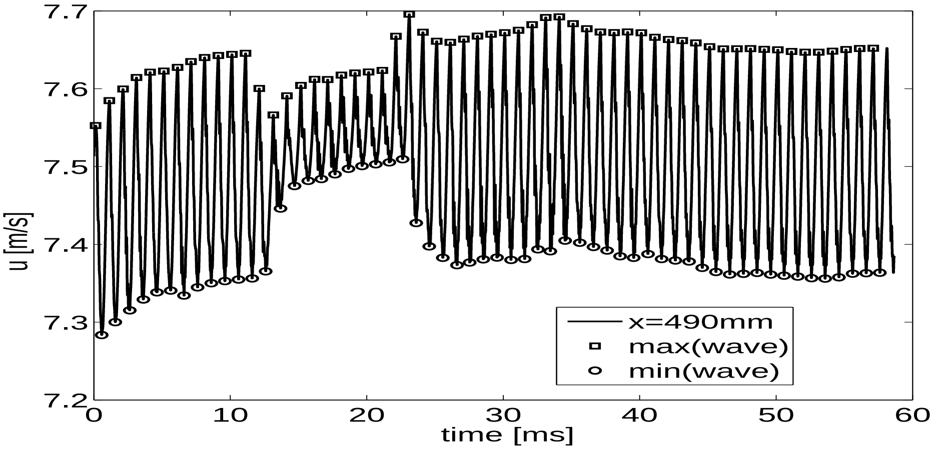

Figure 8.1: The effect of the noise on the amplitude of the TS-wave at $y = \delta_{99}$ in the simulations.

Figure (8.2) (top) shows the amplitude of the TS-wave in a controlled flow. At t=15ms when the wave amplitude has been significantly reduced already, the gust occurs. Since the operating parameters of the plasma actuator are not adjusted to these new operating conditions the wave amplitude increases. At round $t = 20$ms the closed-loop has successfully adjusted to the new operating conditions and the wave amplitude decreases again. After the end of the gust, another increase of the wave amplitude is observed until the optimum operating parameters for the initial conditions before the occurrence of the gust are once again adjusted. The plots in the bottom part of Fig. (8.2) reveal how the operating parameters are strongly varied due to the occurrence of the gust. Finally, after the gust has passed, they converge to the same parameter values that were initially found to be the optimum parameters for the given operating conditions. This numerical test shows that the closed-loop can handle flow disturbances and the application of the optimization technique in real experiments, as discussed in Section 7.3, provides a successful example that active wave cancellation is possible in practice. Future work will have to investigate the treatment of varying operating conditions in more detail.

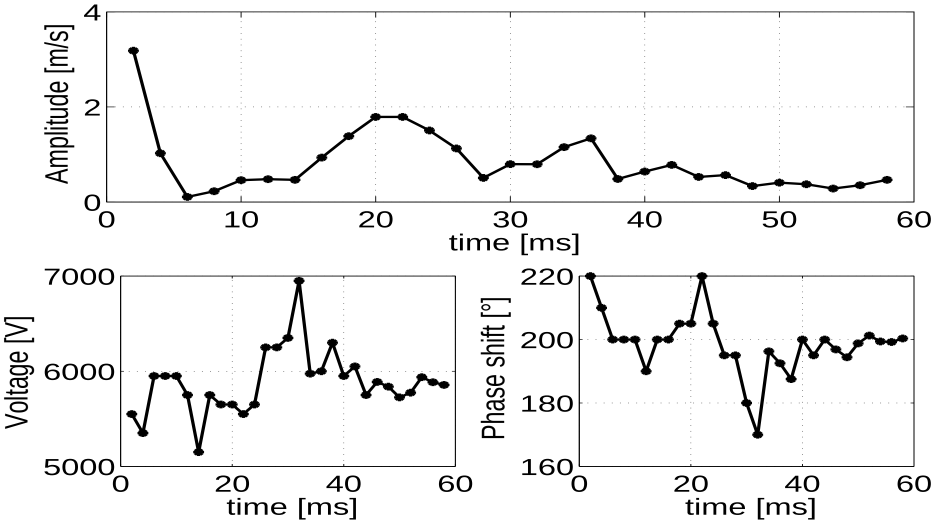

Figure 8.2: The Nelmead method tested in noisy conditions.

The greatest concern is to address these important issues in plasma actuator design through experiments, modeling and theory. As one can see, the present research work is only one step to reach these objectives and make the DBD plasma concept competitive for a wide range of flow applications. Further development requires treatment to the questions discussed above.

# Acknowledgements

The present work was prepared during my employment as a doctoral research at the Center of Smart Interfaces of the Technische Universitaet Darmstadt. First of all I want to express my great appreciation to Professor Dr. Cameron Tropea, as my advisor, for his wisdom, guidance, and encouragement during the course of this work. He has been a tremendous paradigm of a professor for me. For his support (and for his many helpful suggestions for improving this dissertation) I am thankful. No words can express the thanks I have for him.

I would like to thank Prof. Dr. Stefan Ulbrich for refereeing this thesis.

I would also like to thank my colleague Sven Grundmann in a special form for the infinity contribution in to realization of this work. He drew my attention to this topic and enable me to further develop this fascinating research field. The infrastructure and scientific environment provided by him together with Prof. Cameron Tropea, along with his subtle way of supporting and challenging his assistants, offers an excellent chance for one to develop a career. Certainly, his brilliant perception, generosity and friendly manner during this time made an enormous difference.

The financial support from the Deutscher Akademischer Austausch Dienst (DAAD) under contract number A/05/50720 is gratefully acknowledge.

I am truly thankful to the students Alexander Stroh, Jane Elsemueller and Andreas Reeh who added fundamental contributions to every section of my research. Without exception they dedicated themselves fully to their task and I believe they enjoyed it at least a bit. They all helped to set building blocks throughout this research project.

Over the years, more and more colleagues joined me in this field of plasma actuators and flow-control activities, which provided an opportunity for many fruitful discussions. Together with our other colleagues they created a school trip-like atmosphere, which was the reason why I always, also during difficult periods, enjoyed coming to work. Additionally, I offer my sincere gratitude to colleagues, whose assistance was invaluable to understand the difficulties developing this work.

Last but not least I want to express my gratefulness to my dearest wife Daniela. She supported me all times unconditionally and created the private life, although many times far away from me by distance between our countries, which I always looked forward to at the end of each day. Certainly this unforgettable experience and this time living here had been hard without her nice company.

# Bibliography

[1] T. Cebeci and P. Bradshaw, *Momentum transfer in boundary layers*. Hemisphere (McGraw-Hill), Washington, USA, 1977.

[2] A. Yun, *Development and Analisys of Advanced Explicit Algebraic Turbulence and Scalar Flux Models for Complex Enginnering Configurations.* PhD thesis, Technischen Universität Darmstadt, Darmstadt, 2005.

[3] M. J. D. Powell, "The NEWUOA software for unconstrained optimization without derivates," in *in Workshop on Large Scale Nonlinear Optimization, Ed. Nonconvex Optimization and Its Applications, Italy*, vol. 83, Springer, 2004.

[4] J. Elsemueller, "Optimierung von Plasmaaktuator-Parametern zur Auslöschung von Tollmien-Schlichting-Wellen mit NEWUOA," Master's thesis, Technische Universität Darmstadt, Fachgebiet Mathematik, 2009.

[5] A. D. Reeh, "Development and implementation of a method for linear stability analysis in natural and manipulated boundary-layer flows," Master's thesis, TU-Darmstadt, 2008.

[6] G. Schubauer and H. K. Skramstad, "Laminar boundary layer oscillations and transition on a flat plate," tech. rep., National Advisory Committe for Aeronautics, 1948.

[7] H. Schlichting and K. Gersten, *Boundary-Layer Theory*. Springer - Verlag, Berlin, Ed. K. Gersten, 1982.

[8] W. Saric, *Boundary-Layer Stability and Transition*. Springer-Verlag, Heidelberg: Springer Handbook of Experimental Fluid Mechanics, Editors: C. Tropea, A.L. Yarin and J. Foss, 2007.

[9] R. E. Mayle, "A theory for predicting the turbulent-spot production rate.," *Journal of Turbomachinery*, vol. 121, pp. 588 – 593, 1999.

[10] V. J. Modi, "Moving surface boundary-layer control: A review," *J. Fluids Struct.*, vol. 11, pp. 627 – 663, 1997.

[11] D. Greenblatt and I. J. Wygnansky, "The control of separation by periodic excitation," *Prog. Aero. Sci.*, vol. 36, pp. 487 – 545, 2000.

[12] J. C. Lin, "Review of research on low-profile vortex generators to control boundary-layer separation," *Prog. Aero. Sci.*, vol. 38, pp. 389 – 420, 2002.

[13] S. J. Lee and Y. G. Jang, "Control of flow around a NACA 0012 airfoil with a micro-ribblet film," *J. Fluids Struct.*, vol. 20, pp. 659 – 672, 2005.

[14] R. D. Joslin, "Aircraft laminar flow control," *Ann. Rev. Fluid Mech.*, vol. 30, pp. 1 – 29, 1998.

[15] M. Gad-el Hak, *Flow Control: Passive, Active and Reactive Flow Management*. Cambridge University Press, 2000.

[16] D. Henningson and P. J. Schimd, *Stability and Transition in Shear Flows*. Springer - Verlag, Berlin, Ed. J. E. Marschen and L. Sirovich, 2001.

[17] C. Gmelin and U. Rist, "Active control of laminar-turbulent transition using instantaneous vorticity signals at the wall," *Phys. of Fluids*, vol. 13, pp. 513 – 519, 2001.

[18] P. J. Schmid, "Nonmodal stability theory," *Ann. Rev. Fluid Mech*, vol. 39(1), pp. 129 – 162, 2007.

[19] J. H. M. Fransson, A. Talamelli, L. Brandt, and C. Cossu, "Delaying transition to turbulence by a passive mechanism," *Phys. Rev. Lett.*, vol. 96(6):064501, 2006.

[20] R. D. Joslin, G. Erlebacher, and M. Y. Hussaini, "Active control of instabilities in laminar boundary-layer flow. Part 1: An overview," tech. rep., Institute for Computer Applications in Science and Engineering, Hampton, VA, 1994.

[21] H. W. Liepmann, G. L. Brown, and D. M. Nosenchuck, "Control of laminar instabilities waves using a new technique," *J. Fluid Mech.*, vol. 118, pp. 187 – 200, 1982.

[22] Z. Wanga, K. S. Yeob, and B. C. Khoob, "Spatial direct numerical simulation of transitional boundary layer over compliant surfaces," *Computers & Fluids*, vol. 34(9), pp. 1062 – 1095, 2005.

[23] J. J. Riley, M. Gad-el Hak, and R. W. Metcalfe, "Compliant coatings," *Ann. Rev. Fluid Mech*, vol. 20, pp. 393 – 420, 1988.

[24] T. Albrecht, R. Grundmann, G. Mutschke, and G. Gerbeth, "On the stability of the boundary layer subject to a wall-parallel Lorentz force," *Phys. of Fluids*, vol. 18, pp. 98 – 103, 2006.

[25] T. Albrecht, H. Metzkes, R. Grundmann, G. Mutschke, and G. Gerbeth, "Tollmien-Schlichting wave damping by a streamwise oscillating Lorentz force," *Magnetohydrodynamics*, vol. 44(3), pp. 205 – 222, 2008.

[26] S. Grundmann and C. Tropea, "Active cancellation of artificially introduced tollmien-Schlichting waves using plasma actuators," *Exp. in Fluids*, vol. 44, Issue 5, pp. 795 – 806, 2007.

[27] R. D. Joslin, R. A. Nicolaides, G. Erlebacher, M. Y. Hussaini, and M. D. Gunzburger, "Active control of boundary-layer instabilities: Use of sensors and spectral controller," *AIAA Journal*, vol. 33, pp. 1521 – 1523, 1995.

[28] M. Gaster, "Active control of boundary layer instabilities using MEMS," *Current Science*, vol. 79(6), pp. 774 –780, 2000.

[29] D. P. Rizzetta and M. R. Visbal, "Large eddy simulation of plasma-based control strategies for bluff body flow," *AIAA Journal*, vol. 47, pp. 717 – 729, 2009.

[30] S. Grundmann, *Transition Control using Dieletric Barrier Discharge Actuators*. PhD thesis, TU-Darmstadt, Darmstadt, 2008.

[31] D. Sturzebecher and W. Nitsche, "Active cancellation of Tollmien-Schlichting instabilities on a wing using multi-channel sensor actuator systems," *Heat and Fluid Flow*, vol. 24(4), pp. 572–583, 2003.

[32] H. Opfer, F. Evert, D. Ronneberger, and F. R. Grosche, “On the potential and the limitations of boundary-layer stabilization via active wave cancellation. in recent results in laminar turbulent transition,” *Notes on Numerical Fluid Mechanics and Multidisciplinary Design*, vol. 86, pp. 219 – 230, 2003.

[33] K. P. Singh and S. Roy, “Force approximation for a plasma actuator operating in atmospheric air,” *J. Appl. Phys.*, vol. 103, pp. 013305–1 – 013305–6, 2008.

[34] K. P. Singh and S. Roy, “Force generation due to three-dimensional plasma discharge on a conical forebody using pulsed direct current actuators,” *J. Appl. Phys.*, vol. 103, pp. 103303–1 – 103303–6, 2008.

[35] J. Boeuf, Y. Lagmich, T. Callegari, L. Pitchford, and T. Unfer, “New insights in the physics of DBD plasma actuators for flow control,” *46th AIAA Aerospace Sciences Meeting and Exhibit*, pp. AIAA2008–1376, 2008.

[36] J. Boeuf and L. C. Pitchford, “Electrohydrodynamic force and aerodynamic flow acceleration in surface dielectric barrier discharge,” *J. Appl. Phys.*, vol. 97(10), pp. 103307–1 – 103307–7, 2005.

[37] J. Boeuf, Y. Lagmich, T. Unfer, T. Callegari, and L. Pitchford, “Electrohydrodynamic force in dielectric barrier discharge plasma actuators,” *J. Appl. Phys.*, vol. 40, pp. 652–662, 2007.

[38] A. V. Likhanskii, M. N. Shneider, S. O. Macheret, and R. B. Miles, “Modeling of dielectric barrier discharge plasma actuator in air,” *J. Appl. Phys.*, vol. 103(5), pp. 053305–1 – 053305–13, 2008.

[39] A. V. Likhanskii, V. V. Semak, M. N. Shneider, D. F. Opaits, R. B. Miles, and S. O. Macheret, “Parallel code development and numerical investigation of surface charge build-up in DBD plasma actuator,” *AIAA 2008-1380*, 2008.

[40] R. S. Quadros, S. Grundmann, and C. Tropea, “Tollmien-Schlichting waves control using plasma actuators,” *13. STAB Workshop 2007 DLR Goettingen*, 2007.

[41] S. Grundmann and C. Tropea, “Experimental transition delay using glow-discharge plasma actuators,” *Exp. in Fluids*, vol. 42(4), pp. 653–657, 2007.

[42] S. Grundmann and C. Tropea, “Pulsed plasma actuators for active boundary-layer influence,” in *12. STAB Workshop 2005 DLR Goettingen*, 2005.

[43] T. R. Bewley and S. Liu, “Optimal and robust control and estimation of linear paths to transition,” *J. Fluid Mech.*, vol. 365, pp. 305 – 349, 1998.

[44] M. Högberg and D. Henningson, “Linear optimal control applied to instabilities in spatially developing boundary-layers,” *J. Fluid Mech.*, vol. 470, pp. 151 – 179, 2002.

[45] T. R. Bewley, “Flow control: New challenges for a new renaissance,” *Prog. Aero. Sci.*, vol. 37, pp. 21 – 58, 2001.

[46] J. Roth and X. Dai, “Optimization of the aerodynamic plasma actuator as an electrohydrodynamic EHD electrical device,” *AIAA Aerospace Sciences Meeting and Exhibit*, 2006.

[47] M. Forte, J. Jolibois, J. Pons, E. Moreau, G. Touchard, and M. Cazalens, "Optimization of a dielectric barrier discharge actuator by stationary and non-stationary measurements of the induced flow velocity - application to airflow control," *Exp. in Fluids*, vol. 43(6), pp. 917 – 928, 2007.

[48] J. A. Nelder and R. Mead, "A simplex method for function minimization," *The Computer Journal*, vol. 7, pp. 308 – 313, 1965.

[49] W. Spendley, G. R. Hext, and F. R. Himsworth, "Sequential application of simplex design in optimization and evolutionary operations," *Technometrics*, vol. 4, pp. 441 – 461, 1962.

[50] K. I. M. McKinnon, "Convergence of the Nelder-Mead simplex method to a non-stationary point," *SIAM on Optimization*, vol. 9, pp. 148 – 158, 1999.

[51] V. Torczon, "On the convergence of the multidirectional search algorithm," *SIAM on Optimization*, vol. 1(1), pp. 123 – 145, 1991.

[52] M. J. D. Powell, "Developments of NEWUOA for minimization without derivatives," *IMA of Num. Analysis*, vol. 28, pp. 649 – 664, 2008.

[53] W. Shiquan and W. Fang, "Computation of a trust region step," *Acta Mathematicae Applicatae Sinica*, vol. 7(4), 1991.

[54] R. S. Quadros, S. Grundmann, and C. Tropea, "Numerical simulations of the transition delay plasma actuators," in *7th International ERCOFTAC Symposium on Engineering Turbulence Modelling and Measurements*, (Limassol, Cyprus), 2008.

[55] J. Fröhlich, *Large Eddy Simulation Turbulenter Strömungen*. B. G. Teubner - Verlag, Wiesbaden, 2006.

[56] S. P. Pope, *Turbulent Flows*. Cambridge University Press, 2000.

[57] P. Sagaut, *Large Eddy Simulation for Incompressible Flows - An Introduction*. Springer - Verlag, Heidelberg, Ed. Board, 2006.

[58] O. Wehrmann, "Tollmien-Schlichting waves under the influence of a flexible wall," *Phys. of Fluids*, vol. 8, p. 1389, 1965.

[59] P. Cvitanovic, *Universality in Chaos*. Adam Hilger, Bristol, 1989.

[60] P. Manneville, *Dissipative structures and weak turbulence*. Springer - Verlag, Berlin, Ed. Manneville, P., 1995.

[61] T. Mullin and R. Kerswell, *Laminar-Turbulent Transition and Finite Amplitude Solutions*. Fluid Mechanics and its Applications, Springer - Verlag, Netherland, 2005.

[62] B. Frohnapfel, *Flow Control of Near-Wall Turbulence*. PhD thesis, Universitaet Erlangen, Shaker Verlag, Aachen, 2007.

[63] A. A. Townsend, *The structure of turbulent shear flow*. Cambridge University Press, Great Britain, Second edition, 1958.

[64] Invent Computing GmbH, Erlangen, *FASTEST-3D CFD code*, 1997.

[65] J. Smagorinsky, “General circulation experiments with the primitive equations: I. the basic experiment,” *Mon. Weather Rev*, vol. 91, pp. 99 – 164, 1963.

[66] U. Piomelli, “Large-eddy and direct simulation of turbulent flows,” tech. rep., Dept. of Mechanical Eng., University of Maryland, College Park, Maryland - USA, 2001.

[67] D. K. Lilly, “A proposed modification of the Germano subgrid-scale closure method,” *Phys. Fluids*, vol. 4, pp. 633 – 635, 1992.

[68] T. J. Chung, *Computational Fluid Dynamics*. Cambridge University Press, 2008.

[69] R. D. Moser, J. Kim, and N. N. Mansour, “Direct numerical simulation of turbulent channel flow up to $Re_\tau = 590$,” *Phys. Fluids*, vol. 11(4), pp. 943–945, 1999.

[70] S. Patankar and D. Spalding, “A calculation procedure for heat, mass and momentum transfer in three-dimensional parabolic flows,” *Int. J. Heat and Mass Transfer*, vol. 15, p. 1787, 1972.

[71] J. H. Ferziger and M. Peric, *Computational Methods for Fluid Dynamics*. Springer - Verlag, Berlin, 1996.

[72] A. L. De Bortoli, *Introduction of Computational Fluid Dynamics*. Universidade Federal do Rio Grande do Sul, UFRGS, Porto Alegre, 2000.

[73] J. T. Poinsot and S. K. Lele, “Boundary conditions for direct simulations of compressible viscous flows,” *J. Comp. Physics*, vol. 101, pp. 104 – 129, 1992.

[74] M. M. Rai and P. Moin, “Direct numerical simulation of transition to turbulence in a spatially evolving boundary-layer,” *J. Comp. Physics*, vol. 109, pp. 169 – 192, 1993.

[75] F. Durcos, P. Comte, and R. Lesier, “Large-eddy simulation of transition to turbulence in a boundary layer developing spatially over a flat plate,” *J. Fluid Mech.*, vol. 326, pp. 1 – 36, 1996.

[76] X. Huai, R. D. Joslin, and U. Piomelli, “Large-eddy simulation of transition to turbulence in boundary layers,” *Theoret. Comput. Fluid Dyn.*, vol. 9, pp. 149 – 158, 1997.

[77] S. Grundmann, S. Klumpp, and C. Tropea, “Experimental and numerical investigations of boundary-layer influence using plasma-actuators.,” *Notes on Numerical Fluid Mechanics and Multidisciplinary Design*, vol. 95, Springer - Verlag, Heidelberg, pp. 56 – 68, 2006.

[78] C. Baird, C. Enloe, T. McLaughlin, and J. Baughn, “Acoustic testing of the dielectric barrier discharge (DBD) plasma actuator,” *AIAA-2005-0565*, 2005.

[79] R. Hippler, S. Pfau, M. Schmidt, and K. H. Schoenbach, *Low Temperature Plasma Physics - Fundamental Aspects and Applications*. WILEY-VCH, Springer - Verlag, Berlin GmbH, Eds. Rainer Hippler, Institute of Physics, University of Greifswald, Germany, 2001.

[80] C. Enloe, T. McLaughlin, G. Font, and J. Baughn, “Parameterization of temporal structure in the single dielectric barrier aerodynamic plasma actuator,” in *UB/TIB Hannover, Tagung RN 160*, 2005. AIAA 2005-0564.

[81] C. Enloe, T. McLaughlin, R. VanDycen, K. Kachner, E. Jumper, and T. Corke, “Mechanisms and responses of a single dielectric barrier plasma actuator: Plasma morphology,” *AIAA-Journal*, vol. 42(3), pp. 589–594, 2004.

[82] C. Enloe, T. McLaughlin, R. VanDycen, K. Kachner, E. Jumper, T. Corke, M. Post, and O. Haddad, “Mechanisms and responses of a single dielectric barrier plasma actuator: Geometric effects,” *AIAA Journal*, vol. 42(3), pp. 595–604, 2004.

[83] C. Steffes, “Erste Ansätze einer neuen Strategie zur effizienten Modellierung eines Plasma-Aktuators auf Basis des Vertändnisses bestehender Modelle.,” Master’s thesis, TU-Darmstadt, 2008.

[84] S. Grundmann, T. Klumpp, and C. Tropea, “Stabilizing a laminar boundary layer using plasma actuators,” in *Proceedings of the 25th International Congress of the Aeronautical Sciences*, Hamburg 2006.

[85] B. Jayaraman and W. Shyy, “Flow control and thermal management using dielectric glow discharge concepts,” *AIAA 2003-3712*, 2003.

[86] J. B. Wilke, *Aerodynamische Strömungssteuerung mittels dilektrischen Barrierentladungs-Plasmaaktuatoren, 2009.* PhD thesis, Technische Universität Darmstadt, 2009.

[87] T. Corke and E. Matlis, “Phased plasma arrays for unsteady flow control,” *AIAA 2000-2323*, 2000.

[88] S. Grundmann and C. Tropea, “Experimental damping of boundary-layer oscillations using dbd plasma actuators,” *Int. J. Heat and Fluid Flow*, vol. Article in Press, 2009.

[89] R. D. Henderson and G. E. Karniadakis, “Unstructured spectral element methods for simulation of turbulent flows,” *J. Comp. Phys.*, vol. 122(2), pp. 191 – 217, 1995.

[90] U. Rist and H. Fasel, “Direct numerical simulation of controlled transition in a flat-plate boundary layer,” *J. Fluid Mech.*, vol. 298, pp. 211 – 248, 1995.

[91] K. Horiuti and Y. Takagi, “Identification method for vortex sheet structures in turbulent flows,” *Phys. of Fluids*, vol. 17, pp. 121703/1 – 121703/4, 2005.

[92] L. Huang, P. Huang, and R. LeBeau, “Numerical study of blowing and suction control mechanism on NACA0012 airfoil,” *J. of Aircraft*, vol. 41, pp. 1005–1013, 2004.

[93] J. H. Mathews and K. D. Fink, *Numerical Methods Using MATLAB*. Upper Saddle River, 2003.

[94] D. Winfield, “Function minimization by interpolation in a data table,” *J. Inst. Maths Applics*, 1973.

[95] S. Grundmann and C. Tropea, “Experimental damping of boundary-layer oscillations using plasma actuators,” *7th International ERCOFTAC Symposium on Engineering Turbulence Modelling and Measurements - ETMM7*, 2008.

[96] A. Güttler, “Auslegung, Umsetzung und Erprobung verschiedener Regelkonzepte zur aktiven Dämpfung von Tollmien-Schlichting-Wellen mit Hilfe von Plasma Aktuatoren,” Master’s thesis, TU-Darmstadt, 2008.

[97] R. S. Quadros, S. Grundmann, C. Tropea, T. Albrecht, and R. Grundmann, "Numerical investigation of the boundary-layer stabilization using plasma actuators," *Flow, Turbulence and Combustion*, vol. Special Issue ETMM7, 2009. Accepted.

[98] B. Wilke, "Experiment-based fluidic modeling of plasma actuators," *(Personal communication)*, 2008.

[99] A. Duchmann, "Experimentelle Untersuchung der Transitionsbeeinflussung mit Hilfe von Plasma-Actuatoren," Master's thesis, TU-Darmstadt, Darmstadt, 2007.

[100] J. Kriegseis, S. Grundmann, and C. Tropea, "Flow field behavior in proximity of a plasma actuator," in *In European Drag Reduction and Flow Control Meeting EDRFCM 2008, Ostritz - St. Marienthal, Germany*, 2008.

[101] T. Jukes, K. Choi, G. Johnson, and S. Scott, "Turbulent drag reduction by surface plasma through spanwise flow oscillation," in *3rd AIAA Flow Control Conference, 5-8 June 2006, San Francisco, California*, 2006.

[102] T. N. Jukes, K. S. Choi, T. Segawa, and H. Yoshida, "Jet flow induced by a surface plasma actuator," *Proc. IMechE*, vol. 222, pp. 347 – 356, 2008.

[103] N. Bernard, N. Balcon, and E. Moreau, "Electric wind produced by a single dielectric barrier discharge actuator operating in atmospheric flight conditions - pressure outcome," *AIAA 2008-3792*, 2008.

[104] N. Bernard, N. Balcon, and E. Moreau, "Electric wind produced by a surface dielectric barrier discharge operating over a wide range of relative humidity," *AIAA 2009-0488*, 2009.

# 9 Appendix

## 9.1 Truncated conjugate gradient method

The truncated conjugate gradient method is the special simulation for conjugate gradient (CG-simulation). The method produces a linear path in $\mathbb{R}^n$, starting by the fraction $x_{opt} = x_{opt} - d_0$ with $d_0 = 0$. For $j \geq 1$, let $x_{opt} - d_j$ the point of the path at the end j-th straight line segment. It has the form

$$x_{opt} + d_j = x_{opt} + d_{j-1} + \alpha_j s_j, \ j \geq 1, \tag{9.1}$$

where $s_j$ and $\alpha_j$ are the direction of the segment and the step size respectively. The direction $s_j$ of the j-th segments are determined by

$$\begin{aligned} s_j &= -\nabla Q(x_{opt}), \ j = 1 && (9.2)\\ s_j &= -\nabla Q(x_{opt} + d_{j-1}) + \beta_j s_{j-1}, \ j \geq 2 && (9.3) \end{aligned}$$

where

$$\beta_j = \frac{||\nabla Q(x_{opt} + d_{j-1})||^2}{||\nabla Q(x_{opt} + d_{j-2})||^2}. \tag{9.4}$$

The equation (9.2) leads on the descent condition

$$s_j^T \nabla Q(x_{opt} + d_{j-1}) = -||\nabla Q(x_{opt} + d_{j-1})||^2 < 0, \ j \geq 1. \tag{9.5}$$

To determine the step size $\alpha_j$ the maximal step size $\hat{\alpha}_j$ are used with

$$||x_{opt} + d_{j-1} + \hat{\alpha}_j s_j|| = \Delta. \tag{9.6}$$

The search $\alpha_j$ is situated in the interval $[0, \hat{\alpha}_j]$ and

$$Q(x_{opt} + d_{j-1} + \alpha s_j) = Q(x_{opt} + d_{j-1}) + \alpha s_j^T \nabla Q(x_{opt} + d_{j-1}) + \frac{1}{2}\alpha^2 s_j^T \nabla^2 Q s_j \tag{9.7}$$

must be minimized. If $Q(x_{opt} + d_{j-1} + \alpha s_j)$ decreases monotonically to $0 \leq \alpha \leq \hat{\alpha}_j$, then equations (9.6) and (9.7) yields

$$-||\nabla Q(x_{opt} + d_{j-1})||^2 + \hat{\alpha}_j s_j^T \nabla^2 Q s_j \leq 0 \tag{9.8}$$

and $\alpha_j = \hat{\alpha}_j$. Otherwise $s_j^T \nabla^2 Q s_j$ is positive and therefore

$$\alpha_j = \frac{||\nabla Q(x_{opt} + d_{j-1})||^2}{s_j^T \nabla^2 Q s_j} < \hat{\alpha}_j. \tag{9.9}$$

The path are reduced by $x_{opt} + d_{j-1}$, when

- $\alpha_j = \hat{\alpha}_j$, which $||d_{j-1}|| = \Delta$,
- the initial gradient is $\nabla Q(x_{opt}) = 0$ or
- the relationship $\frac{Q(x_{opt}) - Q(x_{opt} + d_j)}{Q(x_{opt}) - minQ(x_{opt} + d) : ||d|| \leq \Delta} \approx 1$,

Let $x_{opt} + d_j$ be the end point of the path, then $d^{(k)} = d_j$.

# Curriculum Vitae

## M.Sc. Régis Sperotto de Quadros

graduate at Mathematics from Universidade de Passo Fundo (2000) and master's at Mathematics from Universidade Federal do Rio Grande do Sul (2003). Doctorade at natural sciences from Technische Universitaet Darmstadt (2009). Has experience in Mathematics, focusing on Numerical Analysis and Optimization.

### Personal information

| | |
|---|---|
| Full name | Régis Sperotto de Quadros |
| Parental information | Telmo Rodrigues de Quadros and Leonides Sperotto de Quadros |
| Birth date | 25/11/1975 |
| Birth place | Passo Fundo/RS - Brasil |
| Address | Rua General Osório 1311/32 - Cohabpel - Cep: 96020-000 Pelotas/RS - Brasil |

### Formal education

| | |
|---|---|
| 2006 - 2009 | Ph.D in Mathematics - Technische Universität Darmstadt - Darmstadt/Hessen - Germany |
| 2001 - 2003 | Master in Applied Mathematics - Universidade Federal do Rio Grande do Sul - Porto Alegre/RS - Brasil |
| 1996 - 2000 | Graduate in Mathematics - Universidade de Passo Fundo - Passo Fundo/RS - Brasil |
| 1990 - 1993 | Vocational and Technical Education - Escola Agrotécnica Federal de Sertao - Sertao/RS - Brasil |
| 1981 - 1989 | Primary and Secondary School - Escola Estadual de Bela Vista - Passo Fundo/RS - Brasil |